

Experimental Measurement of Mass Transport Parameters of Gas Diffusion Layer and Catalyst Layer in PEM Fuel Cell

by

Hao Xu

A thesis submitted in partial fulfillment of the requirements for the degree of

Master of Science

Department of Mechanical Engineering

University of Alberta

Abstract

A diffusion bridge is modified to accurately measure the in-plane permeability and diffusivity of gas diffusion layers (GDLs), and to measure the through-plane permeability, effective pore diameter, Knudsen diffusivity and effective diffusivity of catalyst layers (CLs).

In order to measure in-plane permeability of GDL, nitrogen is injected through the GDL at various flow rates and the pressure drop is measured. Then, Darcy-Forcheimer equation is used to estimate the permeability. The importance of Knudsen slip is estimated by conducting the permeability experiment at various compression levels using different gases. To measure GDL in-plane diffusivity, nitrogen and oxygen are introduced into each channel and oxygen is transported through the sample into the nitrogen channel. The oxygen mole fraction is measured at the outlet of nitrogen channel and the effective diffusivity of the sample is estimated using Fick's first law. Different GDL types are measured to study the effect of carbon matrix and morphology on mass transport properties. Permeability and diffusivity of GDL are found to decrease with volume fraction in matrix. The volume fraction of large pores increases the permeability and diffusivity of GDL. The gas transport properties are dependent on both matrix and pore diameter.

The CL is fabricated using inkjet printing with varying Nafion loading and effect of ionomer/carbon (I/C) ratio is studied next. The gas-independent permeability and effective pore diameter are obtained using Knudsen's expression. Krypton and CO₂ are used for

validation. It is shown that Darcy's law is not appropriate and that Knudsen's expression provides accurate results. Nafion loading and I/C ratio are found to have a negative influence on permeability and effective pore diameter. Effective diffusivity is also measured using the same protocol as for GDLs. Nafion loading and I/C ratio are found to reduce the effective diffusivity of CL. Ketjen carbon support CL exhibit better gas transport properties than Vulcan carbon support CL.

Keywords: mass transport, gas diffusion layer, catalyst layer, permeability, effective diffusivity, Knudsen diffusivity

Acknowledgements

I would like to thank my supervisor - Dr. Marc Secanell for giving me the valuable opportunity to work in the ESDLab. When I just came here from China about two years ago, I was facing many difficulties. My English was not good, I found it difficult to catch up with the courses and I even did not know how to make my setup work. Dr. Marc Secanell was always supportive to my study and life and gave me great encouragement that helped me adjust to the new environment. I would also like to appreciate his patience during the last two years. There was a period of time I could not write my monthly report well and made some mistakes. Dr. Marc Secanell corrected my mistakes over and over again very patiently and made me realize the importance of writing to my future thesis. Without his support and encouragement, I would have never completed my thesis.

I would also like to thank my family members, especially my wife who encouraged me to come to University of Alberta and pursue my master research. Over the past two years, she stood by my side and gave me great emotional support. Talking with her is the most happiest thing of a day and drove away all my tiredness and anxiety. Thank my Summer for making me into a better person.

I would like to thank my colleagues at the ESDLab for helping in my research. Especially, I would like to thank Manas for providing me SEM images and many constructive suggestions on my experiment, Wei Fei for providing me pore size distributions of GDL, James for teaching me how to calibrate my equipment, Luis for teaching me how to prepare the inks and print the catalyst layer, as well as all the others in the group for their help.

Contents

1	Introduction	1
1.1	Motivation	1
1.2	PEM fuel cell	2
1.2.1	Bipolar plate	3
1.2.2	Gas diffusion layer	4
1.2.3	Microporous layer	5
1.2.4	Catalyst layer	6
1.2.5	Polymer electrolyte membrane	7
1.2.6	Fuel cell performance	7
1.3	Literature review	8
1.3.1	Permeability	8
1.3.2	Diffusivity	12
1.4	Research gap and objectives	20
1.5	Thesis outline	21
2	Measurement of in-plane PEM fuel cell gas diffusion layer gas transport properties	22
2.1	Introduction	22
2.2	Experimental setup	23
2.2.1	In-plane diffusion bridge	23
2.2.2	Sample preparation	24
2.2.3	In-plane permeability	24
2.2.4	In-plane diffusivity setup	25
2.2.5	Experimental conditions	27
2.3	Governing equation and data analysis	27
2.3.1	Governing equation	27
2.3.2	Data analysis	30
2.4	Uncertainty analysis	31

2.4.1	Mass flow controller uncertainty	32
2.4.2	Pressure transducer uncertainty	35
2.4.3	Oxygen sensor uncertainty	35
2.4.4	Thickness measurement uncertainty	36
2.4.5	Permeability uncertainty	36
2.4.6	Experimental permeability precision uncertainty	37
2.4.7	Diffusivity uncertainty	38
2.4.8	Experimental diffusivity precision uncertainty	39
2.5	Results and discussion	39
2.5.1	GDL sample characterization	40
2.5.2	GDL in-plane permeability	44
2.5.3	GDL in-plane diffusivity	51
2.6	Conclusions	60

3 Measurement of through-plane PEM fuel cell catalyst layer gas transport properties **62**

3.1	Introduction	62
3.2	Experimental setup	63
3.2.1	Through-plane diffusion bridge	63
3.2.2	Sample preparation	63
3.2.3	Through-plane permeability and Knudsen diffusivity setup	67
3.2.4	Through-plane diffusivity setup	68
3.2.5	Experimental conditions	72
3.2.6	Catalyst layer characterization	72
3.3	Governing equation and data analysis	77
3.3.1	Governing equation	77
3.3.2	Data analysis	84
3.4	Uncertainty analysis	86
3.4.1	Mass flow controller uncertainty	87
3.4.2	Pressure transducer uncertainty	87
3.4.3	Differential pressure controller uncertainty	87
3.4.4	Back pressure controller uncertainty	87
3.4.5	Oxygen sensor uncertainty	87
3.4.6	Thickness measurement uncertainty	87
3.4.7	Permeability uncertainty	88
3.4.8	Experimental permeability precision uncertainty	89

3.4.9	Diffusivity uncertainty	89
3.4.10	Experimental diffusivity precision uncertainty	93
3.5	Results and discussion	93
3.5.1	Experimental results for Toray-90 samples and comparison with literature	93
3.5.2	CL through-plane permeability	97
3.5.3	CL through-plane diffusivity	102
3.6	Conclusions	106
4	Conclusion and future work	108
4.1	Conclusion	108
4.2	Future work	109
A	GDL through-plane diffusivity analysis software	118
B	CL/filter through-plane diffusivity analysis software	126
C	CL through-plane permeability and effective pore diameter	127
D	Factory certificates	130

List of Tables

1.1	Flow regimes and the corresponding Knudsen number [26]	11
2.1	Uncertainties in nitrogen mass flow controller (Unit in SLPM)	34
2.2	Uncertainties in oxygen mass flow controller (Unit in SLPM)	34
2.3	Toray-90 in-plane permeability at two different porosities	38
2.4	Toray-90 in-plane diffusibility at two different porosities	39
2.5	Properties of samples used in the study	43
2.7	In-plane permeability of Toray-90 at different gas flow rate (porosity: 0.78)	45
2.8	Volume fraction in carbon matrix vs. least-square error between experimental permeability and Carman-Kozeny equation	49
2.9	Models used for comparison with experimental data	58
2.10	Fitting parameters in the model	58
2.11	Volume fraction in carbon matrix vs. least-square error between experimental diffusibility and model	60
3.1	Properties of catalyst: Pt/C ratio, Nafion loading, number of layers, thickness measured by Micrometer and SEM	74
3.2	Porosity and I/C ratio of measured CLs	77
3.3	Toray-90 (0%PTFE) through-plane permeability	89
3.4	Toray-90 (0%PTFE) through-plane diffusibility	93
3.5	Toray-90 through-plane permeability	95
3.6	Toray-90 through-plane diffusibility	96
3.7	CL permeability using Darcy's law with nitrogen and helium	99
3.8	Measured CL permeability and effective pore diameter	100
3.9	PTFE filter through-plane diffusibility	102
3.10	PTFE filter through-plane diffusibility and effective diffusivity for different pressure	102
3.11	CL diffusivity and diffusibility (Working gas: Nitrogen and Oxygen)	103
3.13	CL diffusivity and diffusibility and comparison to literature results	104

3.13 Knudsen transport resistance vs. molecular transport resistance 106

List of Figures

1.1	Schematic of a PEM fuel cell	3
1.2	Flow channel designs	4
1.3	SEM image of 29 BA GDL	5
1.4	SGL-38 BC coated with MPL (taken with a stereoscopic optical microscope)	6
1.5	Typical polarization curve of a PEM fuel cell	8
1.6	Closed tube setup	13
1.7	Two-bulb setup	14
1.8	Point source setup	15
1.9	Evaporation tube setup	15
1.10	Diffusion bridge setup	16
2.1	Photograph of (a) steel plate and (b) diffusion bridge assembly	24
2.2	Experimental setup for in-plane permeability	25
2.3	Experimental setup for in-plane diffusivity	26
2.4	Nitrogen mass flow controller calibration curve	33
2.5	Oxygen mass flow controller calibration curve	34
2.6	Oxygen sensor calibration curve	36
2.7	GDL pore size distribution	41
2.8	GDL SEM images: (a) Toray-90 (0%PTFE), (b) Toray-90 (20%PTFE), (c) 24 BA, (d) 28 BA, (e) 29 BA, (f) H2315	42
2.9	Carbon matrix structure in BA series GDL	43
2.10	In-plane permeability results for untreated Toray-90	44
2.11	Experimental results for in-plane permeability at various porosities and liter- ature results (Gostick [19], Feser [4], Mangal [28])	45
2.12	In-plane permeability of different type of GDL samples	46
2.13	In-plane permeability of different type of GDL samples at porosity 0.55 to 0.75	47
2.14	Ratio of $B_v(He)$ to $B_v(N_2)$ at varying compression levels for measured GDL samples	48

2.15	Comparison of experimental permeability to the Carman-Kozeny equation. (a) Toray-90 (0%PTFE), (b) Toray-90 (20%PTFE), (c) Freudenberg H2315, (d) SIGRACET 29 BA, (e) SIGRACET 24 BA, (f) SIGRACET 28 BA	50
2.16	Experimental results for Toray-90 (untreated) in-plane diffusibility	51
2.17	Comparison of experimental in-plane diffusibility to literature results (Rashapov [45], Kramer [41], Mangal [28])	52
2.18	Toray-90 (untreated) in-plane diffusibility at different porosities with different flow rates	53
2.19	Pressure difference between nitrogen and oxygen channel at 0.5 SLPM gas flow rate	54
2.20	Ratio of diffusive to convective flux	55
2.21	In-plane diffusivity and diffusibility of a Toray-90 (0%PTFE) sample	56
2.22	In-plane diffusibility of different type of GDL samples	56
2.23	Comparison of experimental in-plane diffusibility to model estimates	59
3.1	Photograph of one acrylic plate	63
3.2	Prepared GDL samples	64
3.3	Images of: (a) Dimatix 2831 inkjet printer, (b) Printer cartridge	65
3.4	Pictures of: (a) PTFE filter fixed on aluminum foil, (b) Catalyst printed on PTFE filter	65
3.5	CL sample assembly	66
3.6	Through-plane diffusion bridge assembly	66
3.7	Experimental setup for through-plane permeability	67
3.8	Experimental setup for through-plane diffusivity	69
3.9	Photograph of the through-plane setup (Data acquisition card is not shown in this picture)	70
3.10	Pressure difference and oxygen concentration readings for a CL sample	71
3.11	Experimental setup for CL through-plane diffusivity measurement	71
3.12	Catalyst layer placed in epoxy	73
3.13	Catalyst layer SEM images deposited on PTFE filter: (a) 20%Pt/C, 20%Nafion, (b) 20%Pt/C, 30%Nafion, (c) 20%Pt/C, 40%Nafion, (d) 40%Pt/C, 30%Nafion	74
3.14	Surface images of catalyst layers: (a) 20%Pt/C, 20%Nafion, (b) 20%Pt/C, 30%Nafion, (c) 20%Pt/C, 40%Nafion, (d)40%Pt/C, 30%Nafion, (e) 46.7%Pt/C, 30%Nafion	75
3.15	Variation in CL porosity with I/C ratio obtained experimentally and reported by Shukla et al. [69, 72], Yu et al. [36], Inoue et al. [46]	77

3.16	Diffusion resistance network of CL/filter sample	83
3.17	Inlet pressure vs time for Toray-90 with 0%PTFE	94
3.18	Pressure drop vs velocity for Toray-90 with 0%PTFE and 20%PTFE	95
3.19	Differential pressure and oxygen concentration vs time for Toray-90 with 0%PTFE	96
3.20	Oxygen concentration vs pressure drop for Toray-90 with 0%PTFE and 20%PTFE	96
3.21	Filter pressure drop vs. gas velocity using nitrogen and helium	97
3.22	Fitting results for PTFE filter	98
3.23	CL pressure drop vs. gas velocity using nitrogen	99
3.24	CL pressure drop vs. gas velocity using helium	99
3.25	Effective pore diameter vs. CL porosity	100
3.26	Comparison of experimental pressure drop vs. gas velocity using Krypton and CO ₂ to estimated profiles using Knudsen's expression and Darcy's law for dif- ferent catalyst: (a)20%Pt/C, 20%Nafion (b)20%Pt/C, 30%Nafion (c)40%Pt/C, 30%Nafion (d)46.7%Pt/C, 30%Nafion	101
3.27	The oxygen concentrations in nitrogen channel for different CL/filter assembly	103
3.28	CL diffusibility vs porosity and comparison to literature results reported by Z. Yu [36] and G. Inoue [46]	105
3.29	CL diffusibility vs I/C ratio and comparison to literature results reported by Z. Yu [36] and G. Inoue [46]	105
D.1	Factory certificate of pressure transducer	130
D.2	Factory certificate of mass flow controller 1	131
D.3	Factory certificate of mass flow controller 2	132

Nomenclature

English Letters

A	cross-sectional area, m^2
A_o	Surface area per solid volume, m^2/m^3
B_v	Viscous permeability of the porous media, m^2
B_I	Inertial permeability of the porous media, m
D	Diffusion coefficient, m^2/s
D_K	Knudsen diffusivity, m^2/s
D_M	Molecular bulk diffusivity, m^2/s
D^{eff}	Effective diffusivity of the porous media, m^2/s
D_{bulk}	Bulk diffusivity of the porous media, m^2/s
d_f	Fibre diameter, m
d_p	Local pore diameter of the porous media, m
d_p^{eff}	Effective pore diameter of catalyst layer, m
\mathbf{J}	Diffusion flux vector, $kg/m^2 s$
Kn	Knudsen number
k_K	Kozeny constant
L	Width of measured sample, m
M	Molecular mass of a gas, g/mol

\dot{m}	Mass flux of gas in porous media, $kg/(m^2 s)$
\dot{M}	Mass flow rate of gas in porous media, kg/s
\dot{n}	Molar flux of gas in porous media, $mol/(m^2 s)$
\dot{N}	Molar flow rate of gas in porous media, mol/s
N_M	MacMullin number
∇P	Pressure gradient across the porous media, m/s
ΔP	Pressure drop across the porous media, Pa
P	Absolute pressure of gas in channel, Pa
P_x	Precision uncertainty, -
P_1	Inlet pressure of gas in channel, Pa
P_2	Outlet pressure of gas in channel, Pa
R	Gas constant, $J/(mol K)$
r	Fibre radius, m
r_P	Pore radius, m
s	Saturation, -
S_x	Sample standard deviation, -
T	Temperature, K
t_o	Thickness of porous media in uncompressed state, m
t	Thickness of porous media in compressed state, m
V_{pore}	Pore volume of the porous media, m^3
V_{bulk}	Bulk volume of the porous media, m^3
V_o	Volume of measured sample in uncompressed state, m^3
V_c	Volume of measured sample in compressed state, m^3

v	Gas velocity across the porous media, m/s
\dot{V}	Volume flow rate of gas, m^3/s
\dot{V}_p	Volume flow rate of gas in porous media, m^3/s
V_i	Intruded volume of mercury in porous media, m^3/s
w	Mass fraction, -
w_f	Overall uncertainty, -
x_{O_2}	Oxygen mole fraction, -
X	Cumulative pore volume fraction, -

Greek Letters

ϵ_o	Porosity of porous media in uncompressed state, -
ϵ	Porosity of porous media in compressed state, -
η	Dynamic viscosity, $Pa \cdot s$
ρ	Density of a gas, kg/m^3
λ	Mean free path of a gas, m
ϵ_p	Percolation threshold, -
γ	Surface tension of mercury, $ergs/cm^2$
θ	Contact angle, $^\circ$
α	Fitting parameter in percolation correlation, -
τ	Tortuosity
μ	Fitting parameter in percolation theory

Abbreviations

BPC	Back Pressure Controller
CCL	Cathode Catalyst Layer
CL	Catalyst Layer
DPC	Differential Pressure Controller
GDL	Gas Diffusion Layer
HOR	Hydrogen Oxidation Reaction
IPA	Isopropanol
MFC	Mass Flow Controller
MIP	Mercury Intrusion Porosimetry
MPL	Microporous Layer
ORR	Oxygen Reduction Reaction
PEM	Polymer Electrolyte Membrane
PG	Propylene Glycol
PSD	Pore Size Distribution
PT	Pressure Transducer
PTFE	Polytetrafluoroethylene
SEM	Scanning Electron Microscope
SLPM	Standard Liter Per Minute

Chapter 1

Introduction

1.1 Motivation

Global energy demand continues to grow as the world population keeps increasing. According to the International Energy Agency, global energy needs will increase by 30% between 2017 and 2040 due to population growth [1]. Fossil fuels are currently the main source of energy; however, the massive use of fossil fuels is causing serious environmental problems. Carbon dioxide, a green house gas, is produced during the combustion of fossil fuels and it is a major contributor to global warming. Burning fossil fuels emits a number of air pollutants, i.e., SO_2 , NO_x and particulate matter, that are harmful to both the environment and public health [2].

In the last few decades, alternative renewable energy sources and relevant technologies have gained popularity such as wind energy, ocean energy, and solar energy. However, most of these renewable energies are intermittent and their uses are limited by climate or geographical factors. For example, solar technology is cost-effective only in those places where sufficient sunshine is available, while most of nuclear power plants are located off the coast because massive amount of sea water are needed as cooling water. Thus, more stable and reliable types of renewable energy resources are desired to meet the rising energy demand.

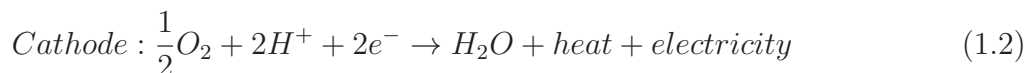
Hydrogen is an ideal energy carrier that can be produced by a myriad of methods, such as water electrolysis using renewable resources. It can be used to replace fossil fuels in the transportation and stationary power sectors because of its high energy density compared to batteries, and zero emissions. In recent years, polymer electrolyte membrane (PEM) fuel cells have proven to be a promising technology due to their higher efficiency and reliability. A PEM fuel cell systems converts the chemical energy stored in hydrogen into electrical

energy. Further, compared to other technologies, fuel cells can be used at any time without producing any green house gas and other pollutants and without being limited by climate conditions or geographical factors. Thus, fuel cell technology is worthy of being further developed.

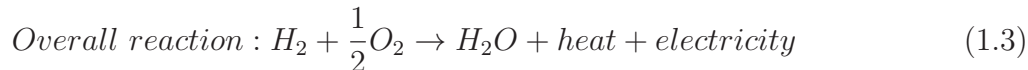
1.2 PEM fuel cell

A PEM fuel cell is an electrochemical system that converts chemical energy into electrical energy. Hydrogen and oxygen are commonly used as fuels and they generate water and heat, so the lack of GHG emissions and particulate matter is one of its advantages compared to other methods of generating electricity. Fuel cells also have higher efficiency because chemical energy is directly converted into electricity thereby minimizing conversion losses. In traditional power plants, the energy conversion is more cumbersome, i.e., chemical energy of fossil fuels is first converted to thermal energy which is then converted to mechanical energy in a turbine, and at a final step, the mechanical energy is converted into electricity.

A fuel cell is composed of an anode, a cathode, a membrane and bipolar plate. Hydrogen is supplied as fuel at the anode side, then flows through the gas diffusion layer (GDL), micro porous layer (MPL), and into the catalyst layer (CL), where it undergoes an oxidation reaction and produces electrons and protons. At the cathode side, oxygen or air is supplied as oxidant, and is then transported to the cathode catalyst layer (CCL), where it combines with electrons and protons and water is produced. The electrochemical reactions for cathode and anode can be written as:



The overall chemical reaction can be obtained by adding equation (1.1) and equation (1.2):



From equation (1.3), it can be seen that the only byproducts of the overall reaction are water, heat and electricity. The water is produced at the cathode, and the electricity is generated by the electron transport in the external circuit.

The structure of a PEM fuel cell is shown in Figure 1.2. The fuel cell is a very compli-

cated system and each of the components has a specific function which will be discussed in the next sections.

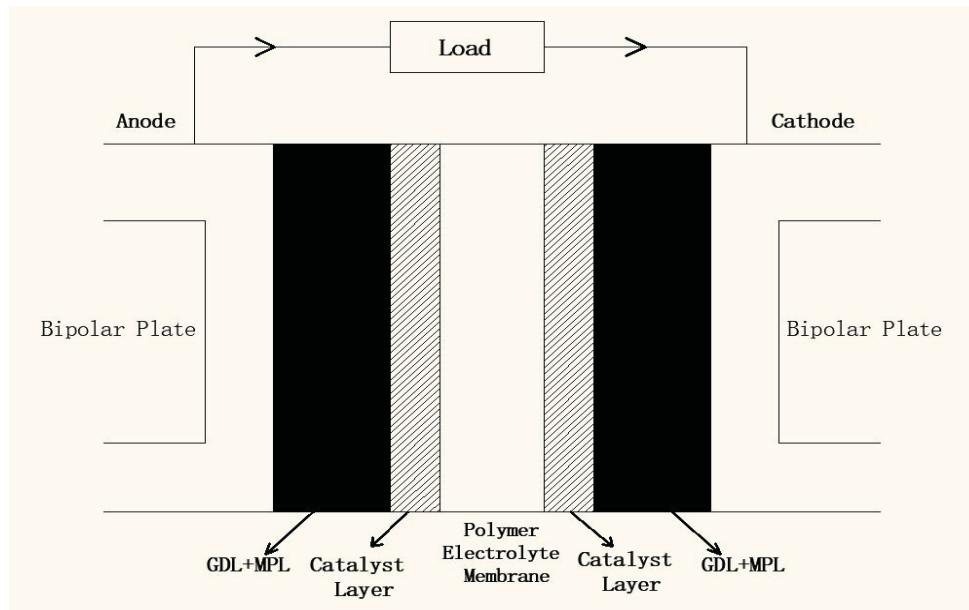


Figure 1.1: Schematic of a PEM fuel cell

1.2.1 Bipolar plate

The bipolar plates are commonly made up of a graphite composite or metals with high thermal and electrical conductivity. Graphites have high resistance to corrosion; however metals have more favorable manufacturability and durability for vibration [3]. The bipolar plates are placed at the two sides of a fuel cell and gas flow channels are machined into it. The bipolar plates play many important roles in a fuel cell such as current collection and transport between cells, gas supply to the reaction site, as well as water and thermal management [3].

There are several types of gas channels. Three types that are commonly used are parallel, serpentine and interdigitated flow fields, which are shown in Figure 1.2. Each type of flow field has both advantages and disadvantages. It is really important to select an appropriate type of flow channel depending on the application.

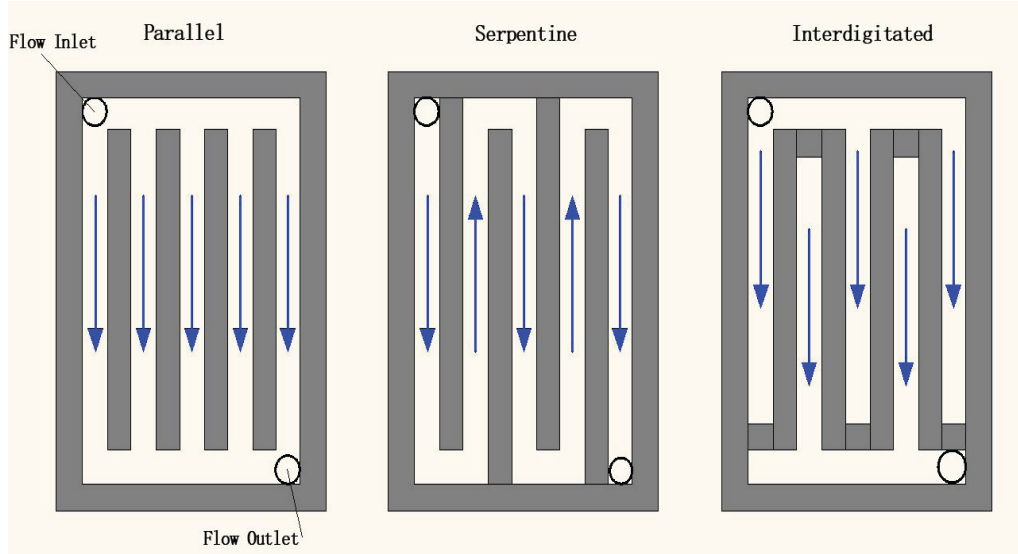


Figure 1.2: Flow channel designs

1.2.2 Gas diffusion layer

The gas diffusion layer (GDL) is a porous media, as shown in Figure 1.3, which is placed next to the bipolar plates. The porous structure enables the reactant gases in the flow channel to reach the active sites in the catalyst layer. The GDL also has other essential functions: (a) mechanical support for the proton exchange membrane; (b) electronic conductivity; (c) heat removal; and (d) water removal [4]. Figure 1.3 shows a scanning electron microscope (SEM) image of the porous structure of a 29BA GDL sample. GDLs are always treated with polytetrafluorethylene (PTFE) to facilitate the liquid removal. Besides, many GDLs, such as SGL GDLs, contain certain amount of carbon matrix (see Figure 1.3) that hold fibres together. As explained by SGL Carbon company, during the manufacturing of GDLs, the raw carbon paper is impregnated with carbonisable thermoset resins (with optional addition of carbon fillers), cured and re-carbonized. The treatment can enhance the conductivity and is used to control the porosity [5]. The carbon matrix affects the transport properties of GDLs but they have been seldom studied by researchers.

The porosity of a GDL sample, ϵ_o , is defined as the ratio of pore volume to the bulk volume of the sample. Mathematically,

$$\epsilon_o = \frac{V_{pore}}{V_{bulk}} \quad (1.4)$$

As discussed before, one of the key roles of the GDL is to transport gases. Its gas

transport abilities are dictated by its porosity, tortuosity and pore size distribution. The pore size distribution (PSD) of the GDL can be measured by mercury intrusion porosimetry (MIP). Mercury is intruded into the pores of a GDL sample, the pore size is estimated by using Washburn equation based on the pressure required for intrusion. More details on MIP measurements will be discussed in the next chapter.

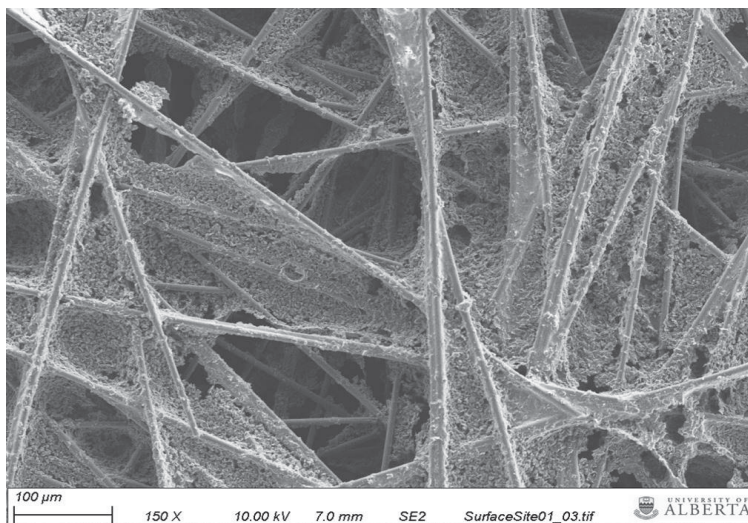


Figure 1.3: SEM image of 29 BA GDL

Carbon-based GDLs are widely used because they can achieve (i) relative stability in acidic environment; (ii) good transport properties for gases and liquids; (iii) high electrical conductivity; and, (iv) good elasticity with compression [6]. In this thesis, carbon papers are studied as they are more commonly used in PEM fuel cells.

1.2.3 Microporous layer

The microporous layer (MPL) is usually made of carbon particles and a hydrophobic agent such as PTFE. The MPL is often coated on one side of the GDL and can be used on both of anode and cathode electrode [7]. The thickness of the MPL has been reported in the range of $38.8 \mu\text{m}$ - $112.2 \mu\text{m}$ and the pore size varies from 7 nm to 133 nm [8]. Figure 1.4 shows a photo of a SGL-38 BC sample taken by a stereoscopic optical microscope (Leica MC170 HD).

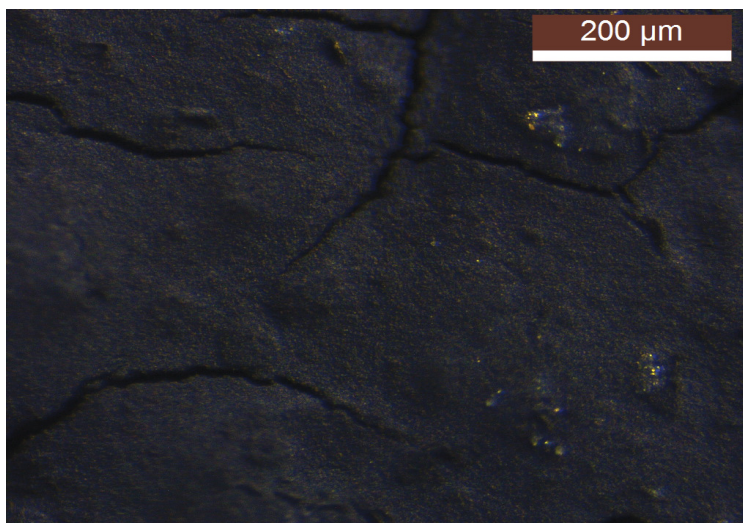


Figure 1.4: SGL-38 BC coated with MPL (taken with a stereoscopic optical microscope)

The MPL has many essential functions such as (i) reduce the negative effects of electrode flooding, (ii) improve the electrical contact between gas diffusion layer and catalyst layer; and, (iii) prevent fast dry-out of PEM at low current densities or low humidity [9] .

1.2.4 Catalyst layer

The catalyst layer is generally applied to the membrane at both anode and cathode side [10]. It is a thin film consisting of ionomer (usually Nafion), platinum/carbon particles and void regions. The protons are transported through the electrolyte (Nafion), while the electrons are transported in the solid phase (Pt/carbon) and the void regions enable the gas reactants and liquid products to transport between the GDL and the reaction sites. The thickness of catalyst layer is usually in the range of $5\mu\text{m}$ - $60\mu\text{m}$ [11]. The pore size distribution of catalyst layer has been reported in the range of 5nm - 130nm [12].

The typical size of Pt nanoparticles is 2nm - 5nm . Most of the utilized Pt catalyst is placed at the cathode side due to the inherently sluggish oxygen reduction reaction (ORR) in the cathode catalyst layer (CCL) [12]. The ORR kinetics in cathode CL have been reported to be approximately six orders of magnitude slower than the hydrogen oxidation reaction (HOR) kinetics in anode CL [13]. High cost and Pt supply limitations are big issues for the commercialization of fuel cell. Some researchers have been working on developing active, selective, and durable non-precious metal catalysts based on earth-abundant materials [14] [15].

1.2.5 Polymer electrolyte membrane

Current polymer electrolyte membranes for fuel cell are mostly based on a sulfonated tetrafluoroethylene polymer called Nafion. The polymer electrolyte membrane is sandwiched between anode catalyst layer and cathode catalyst layer. The PEM is used for transporting the H^+ ions in the anode side to the cathode side. Another function of the PEM is preventing gas and electrons from crossing from anode to cathode and vice versa. PEMs possess the following properties: (i) good ion conductivity, (ii) gas tight, (iii) electric insulator, (iv) good chemical and mechanical stability [16]. PEMs range in thickness from 20 μm [17] to 260 μm [18].

1.2.6 Fuel cell performance

PEM fuel cell performance is usually expressed by a voltage vs. current density curve, commonly known as a polarization curve and shown in Figure 1.5. There are three main losses in fuel cells: (a) reaction rate loss (kinetics loss), (b) resistance loss (ohmic loss), and (c) mass transport loss. Mass transport loss is due to the reactants not being transported to the reaction sites fast enough. The insufficient reactant supply limits the current density and reduces the cell performance. Therefore, increasing fuel cell performance with the same amount of catalyst can be achieved by studying and improving the mass transport properties of different PEM fuel cell electrode layers.

GDL and CL are the components where gas transport takes place so it is crucial to determine the transport properties, i.e. permeability and diffusivity of the porous media in fuel cells. In addition, for accurate numerical simulation of fuel cell, these transport parameters are also needed. The goal of this thesis is to develop an experimental setup to measure all gas transport properties of these materials.

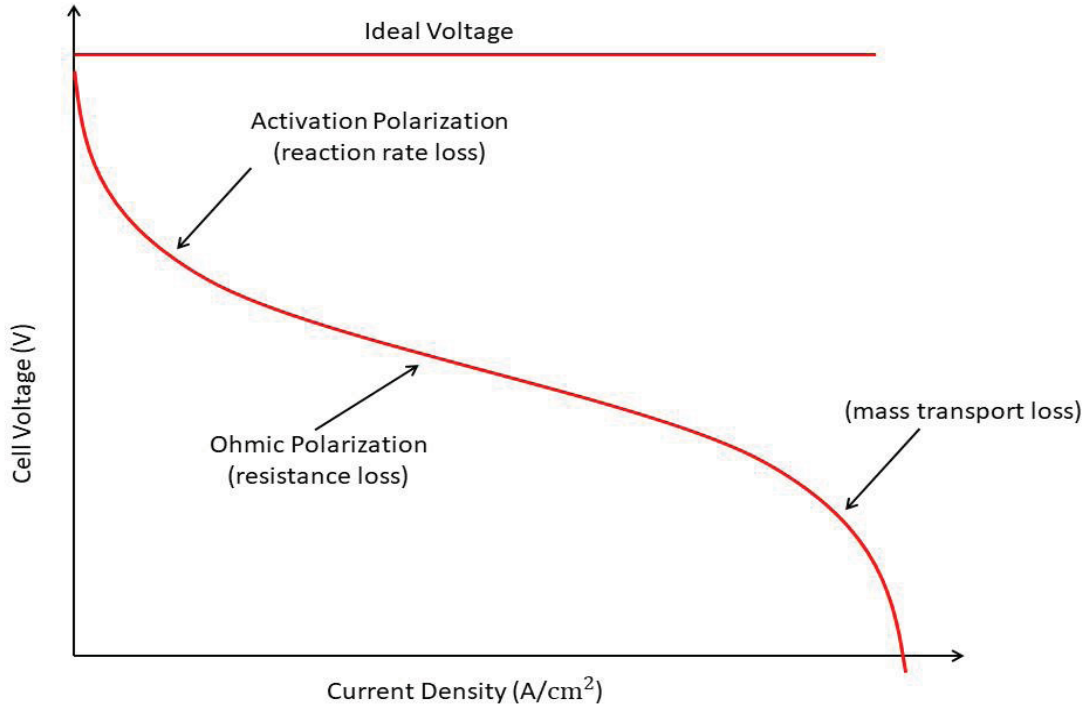


Figure 1.5: Typical polarization curve of a PEM fuel cell

1.3 Literature review

1.3.1 Permeability

In porous media, such as gas diffusion layers, permeability is a key parameter to be determined as it determines the mass flow rate of gas that can cross a porous media for a given pressure difference. Darcy's law is the most commonly used equation to describe low Reynolds number flow through a porous material. It relates the fluid velocity to the pressure gradient by means of the porous media permeability, B_v :

$$\nabla P = -\frac{\eta}{B_v} \mathbf{v} \quad (1.5)$$

where ∇p is the pressure gradient across the porous media in Pa/m, η is the dynamic viscosity of the fluid in Pa·s, \mathbf{v} is the velocity; and, B_v is the permeability of porous media in m^2 .

As the gas velocity becomes higher, the gas transport in the porous media becomes complicated and the inertial effect, also known as Forcheimer effect, needs to be considered.

For one-dimension gas flow, the Darcy-Forcheimer equation is used to extend Darcy’s law to include inertial effects:

$$\nabla P = -\frac{\eta}{B_v}v - \frac{\rho}{B_l}v^2 \quad (1.6)$$

where B_l is the inertial permeability in m and it is used to account for inertial effects.

1.4.1.1 Experimental studies of gas permeability in fuel cell

Many experimental approaches have been employed to measure the permeability of GDLs. Gostick et al. [19] measured in-plane and through-plane permeability of GDLs with two different testing devices. In the through-plane direction, a circular GDL sample was compressed between two plates. The gas flowed through the GDL sample in the through-plane direction from one side to the other side and the flow rate across the sample was measured using a digital flow meter. The pressure drop was measured at different flow rates in order to create a plot of pressure drop vs. flow rate through the material. The through-plane permeability range was between $5.7 \times 10^{-12} \text{ m}^2$ and $69.4 \times 10^{-12} \text{ m}^2$.

To measure permeability in the in-plane direction, the pressure drop was measured in two perpendicular directions. Shims of known thickness were used to control the spacing between the plates and in-plane permeability was measured at different compressions. The gas flowed into the inlet header, travelled through the GDL sample to the outlet header and exhausted to the atmosphere. The in-plane permeability of GDLs was found to decrease by around ten times as the sample was compressed from a compressed volume fraction of 95% to 50%. It is found that direction has no obvious effect on the in-plane permeability [19].

Ismail et al. [20] measured the in-plane permeability of a number of carbon substrates and MPL-coated GDLs using a setup similar to Gostick et al. [19]. The GDL sample (54 mm long \times 20 mm wide) was placed between steel plates. It was shown that the in-plane permeability of carbon substrates decreases with increasing PTFE content, in contrast, the higher is the PTFE content in the MPL, the higher is the permeability.

Ismail et al. [21] also measured the through-plane permeability of GDL samples with and without PTFE. The inertial effect on the permeability value was also analysed. The mass flux vs. pressure gradient across the GDL was plotted and the fitting curve was compared to Darcy-Forchheimer equation to calculate the permeability. Ismail et al. reported that there was an optimal PTFE content where the permeability was the highest. It was also found that under operating conditions used in the experiment, the inertial effect was small enough

to be ignored as it only results in a 0.65% of error. Furthermore, using the same setup, Orogbemi et al. [22] measured the through-plane permeability of GDLs coated with MPLs of various carbon loadings. The carbon loadings were 0.5, 1.0, 1.5, 2.0 and 2.5 mg cm⁻². The permeability of coated GDL and carbon substrate were measured using Darcy’s law and the permeability of the MPL was estimated based on the assumption that the pressure drop across the coated GDL is equal to the sum of the pressure drop across the MPL and carbon substrate. The MPL-coating was found to reduce the permeability of GDL by at least one order of magnitude. In addition, the permeability of the MPL was found to be 2-3 orders of magnitude lower than that of carbon substrate. Finally, the permeability of the GDL was slightly reduced by the MPL sintering.

Gurau et al. [23] also measured the through-plane and in-plane permeability of carbon fibre cloth with different types of micro porous layers. For through-plane experiment, the sample is clamped between two fixtures, each of them consisting of a cylindrical compartment and an annular compartment. The pressure across the sample can be measured by the pressure-differential gauge and flow rate was measured with a rotameter. For in-plane experiment, an annular sample was clamped between an upper and a lower fixture. The assembly was located between the platens of a press. The upstream pressure was measured at different compression levels and different flow rates. Gurau et al. reported the through-plane permeability to be in the range of 0.44×10^{-12} m² to 13×10^{-12} m² and in-plane permeability to be in the range of 0.7×10^{-12} m² to 17.4×10^{-12} m². The permeability of microporous layer with higher PTFE content was found to be higher than that of microporous layer with lower PTFE content. The in-plane permeability was measured to be higher than the through-plane permeability.

Tamayol et al. [24] built an air permeability test bed to investigate the effect of PTFE content on the through-plane permeability of gas diffusion layers. An air tank was used for high pressure air supply and the air pressure was controlled using a digital air pressure regulator. Tamayol et al. found that there was a reverse relationship between the PTFE content and the through-plane permeability.

Carrigy et al. [25] measured the through-plane permeability of GDL/MPL assemblies using a diffusion bridge. Permeability of GDL was estimated with several gases to estimate Knudsen slip in the MPL. The pore size of the MPL is very small, i.e., 7 nm-133 nm, and gas flow was shown to be no longer in the continuum regime. The flow regime is defined by

the Knudsen number, which is mathematically defined as :

$$Kn = \frac{\lambda}{d_p} \quad (1.7)$$

where λ is the mean free path of the gas and d_p is the average pore diameter of porous media. Table 1.1 [26] shows the different flow regimes and corresponding Knudsen number. Carrigy et al. studied the effect of PTFE content in MPL-coated GDL on through-plane permeability. The permeability was measured to decrease with increasing PTFE loadings. In addition, they found that Knudsen's expression provided a more accurate prediction of gas transport in the GDL/MPL sample than the compressible form of Darcy's law. A similar study was also conducted by Pant et al. [26] and similar conclusion was found in their study.

Table 1.1: Flow regimes and the corresponding Knudsen number [26]

Knudsen number	Flow regime
$Kn < 0.001$	Continuum regime, Navier-Stokes(N-S) valid with no-slip boundary condition
$0.001 < Kn < 0.1$	Continuum-transition region; N-S valid only with slip boundary condition
$0.1 < Kn < 10$	Transition region; N-S not valid; moment equations or Burnett equation with slip boundary condition
$Kn > 10$	Free molecule flow; no continuum model valid

Mangal et al. [27] modified the through-plane diffusion bridge used by Pant et al. [26] and measured the through-plane permeability of 34BA and Toray-90 samples with different PTFE content. The bridge consisted of two acrylic plates with two rectangular flow channels machined in them. 34BA shows the highest permeability among all the samples. Increasing the PTFE loading was found to have an adverse effect on GDL permeability. Permeability of Toray-90 varied from $1.1 \times 10^{-12} \text{ m}^2$ to $0.35 \times 10^{-12} \text{ m}^2$ with PTFE content between 0% - 40%.

Mangal et al. [28] also measured in-plane permeability of Toray-90 (untreated) and Toray-90 (40% PTFE) using a setup similar to Gostick et al. [19]. The samples were measured at four compression levels. Permeability was found to be between $0.98 \times 10^{-11} \text{ m}^2$ and $0.13 \times 10^{-11} \text{ m}^2$ and shown to decrease with compression and PTFE content. Mangal also measured in-plane permeability of GDL in four different directions [29] and it was found that direction has no obvious effect on mass transport parameters.

1.4.1.2 Mathematical studies on permeability

The permeability of the GDL has been numerically studied by some researchers [30–35]. The Carman-Kozeny equation is a semi-empirical relation that is most widely used to estimate permeability of porous media and is written as [30]:

$$B_v = \frac{\epsilon^3}{k_K(1 - \epsilon)^2 A_o^2} \quad (1.8)$$

where k_K is the Kozeny constant, ϵ is the porosity of the porous space, A_o is the surface area per solid volume, i.e., A_{fs}/V_s where A_{fs} is the interfacial area between the fluid and solid phases and V_s is the solid volume. For a mean particle diameter d , the specific surface area can be estimated using [30],

$$A_o = \frac{6}{d} \quad (1.9)$$

For fibres of diameter d_f , d can be estimated as $(3/2)d_f$ [30] and equation (1.8) can be given as:

$$B_v = \frac{\epsilon^3}{16k_K(1 - \epsilon)^2 d_f^2} \quad (1.10)$$

In this thesis, the experimental results are used to fit in equation (1.10) to obtain k_K . Other models to predict permeability will not be introduced in this section since this thesis mainly focuses on experimental measurement.

1.3.2 Diffusivity

Diffusivity is an important parameter for porous layers because diffusion is considered to be the primary gas transport mode in the porous media of PEM fuel cells. Fick's law is commonly used to describe gas diffusion in porous material:

$$\mathbf{J} = -D \nabla C \quad (1.11)$$

where \mathbf{J} is a diffusion flux vector, C is the concentration or density, and D is the diffusion coefficient or diffusivity. Under the condition of non-steady state diffusion, a mass balance result in Fick's second law of diffusion:

$$\frac{\partial C}{\partial t} = -D \nabla^2 C \quad (1.12)$$

where t is time.

When diffusion occurs in the transition region, some researchers use Bosanquet approx-

imation to account for Knudsen effects when predicting diffusivity D [36]:

$$\frac{1}{D} = \frac{1}{D_K} + \frac{1}{D_M} \quad (1.13)$$

where D_K is Knudsen diffusivity, D_M is molecular bulk diffusivity. Knudsen diffusivity is given by: [36]

$$D_K = \frac{d_p}{3} \sqrt{\frac{8RT}{\pi M}} \quad (1.14)$$

where d_p is local pore diameter, M is molar mass of the gas, R is gas constant and T is temperature.

1.4.2.1 Experimental apparatus to measure diffusivity

Different experimental methods for measuring effective gas diffusivity have been proposed in the literature [37] [38]. Loschmidt [37] developed closed-tube method, also known as Loschmidt cell method in 1972. It consisted of a top and bottom chambers as shown in Fig 1.6. A valve was located in the middle and used to separate or connect the chambers. Two different gases were initially separated, then started to diffuse after the valve was opened. The effective diffusivity was estimated using Fick's second law. The determination of effective diffusivity requires measurements of temperature, pressure, concentration, time and geometry. The uncertainty is mainly caused by convection from buoyancy effects and can be minimized by using lighter gas in the top chamber. It was reported that the method often has reproducibilities better than 1%, and the measurements have the accuracy of 1% - 3%.

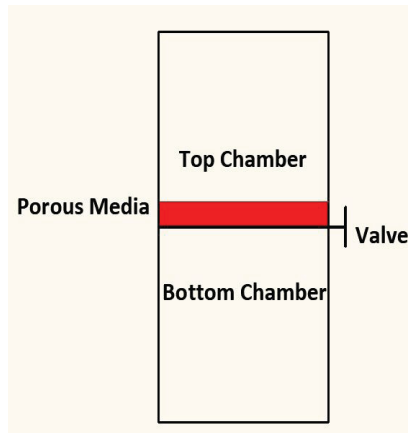


Figure 1.6: Closed tube setup

Ney and Armistead [37] developed two-bulb method in 1947. Two bulbs filled with two

different gases of interest were connected by a narrow tube as shown in Fig 1.7. It was assumed that the diffusion process was in quasi-stationary state and pressure and temperature were constant. The connecting tube volume was considered to be much smaller than either bulb volume. The two-bulb method has similar uncertainties with the closed tube method, but less chance of convective effects. The inaccuracies of two-bulb method have been reported to be 1% - 3.5%.

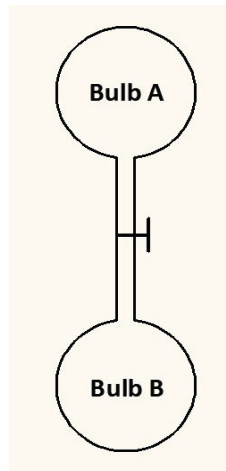


Figure 1.7: Two-bulb setup

Walker and Westenberg [37] developed the point source method in 1958. This method was developed especially for measuring effective diffusion coefficients at high temperatures. A trace gas was steadily supplied through a hypodermic tube into a carrier gas flowing in the same direction. The mixture concentration was measured by a probe located at various distances downstream. The important assumption was steady-state flow, axial symmetry of the mixture concentration, uniform flow velocity, infinitely dilute mixture and absence of convection effects. The sources of error are probe position, measurements of flow, wake caused by the injector tube, difference in density between the trace and carrier gas. The diffusion coefficients have been measured with accuracy in the range of 4% [37].

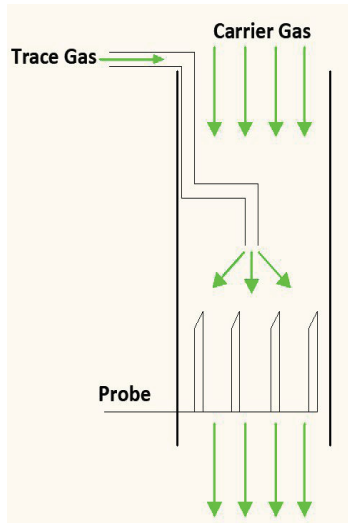


Figure 1.8: Point source setup

Stefan developed the evaporation-tube method in 1873 [37]. This method is useful for determining of diffusion coefficients for vapor-gas mixtures. The tube was partially filled with liquid and the evaporation rate was controlled by diffusion. Across the tube outlet gas flows and carries the vapor away. The setup is shown in Fig 1.9. The rate of liquid loss was observed for long durations in order to estimate effective diffusion coefficient. The assumption was quasi-steady state, gas insolubility, axial symmetry and the absence of convection effect. The temperature range is strongly dependent on the volatility of the liquid to be tested. The reliabilities of diffusion coefficient by the evaporation tube method are several percent [37].

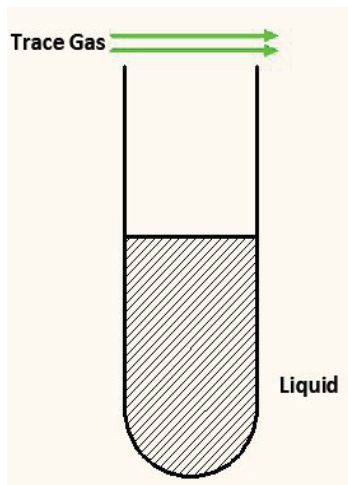


Figure 1.9: Evaporation tube setup

Bendt developed the diffusion bridge setup in 1958 [39]. The setup consisted of two flow channels for two different gases (see Figure 1.10). The channels were connected by a hollow

capillary tube or a porous media to allow the gas diffusion. The pressure difference across the capillary was produced by controlling and adjusting the flow rates. The sources of error are fluctuations in flow rate and measurements of concentration. The advantage of the diffusion bridge is that the method is amenable to operation over a wide range of temperature [39].

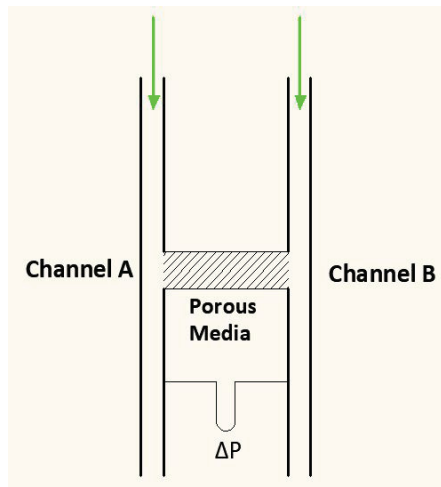


Figure 1.10: Diffusion bridge setup

In this thesis, the diffusion bridge is selected as the method to estimate effective diffusivity because: (1) The setup allows for permeability and diffusivity to be measured simultaneously, (2) The gas flow rate can be controlled to minimize diffusive layer effect, (3) The gas diffusion process can be maintained in a steady state, (4) High accuracy of oxygen level measurement, (5) faster and convenient than other methods, such as evaporation-tube.

1.4.2.2 Experimental studies of gas diffusivity in fuel cell

Martinez et al. [40] used a conductivity cell apparatus to measure GDL conductivity. Based on this value, the effective diffusivity was obtained using $D^{eff} = \frac{D_{bulk}}{N_M} = D_{bulk} \frac{R_o}{R}$ where N_M is the MacMullin number. The setup consisted of a Lexan polycarbonate reservoir and a center division that was used to attach the sample holder. Two coated Ti electrodes were placed on both sides of the sample and served as working and counter electrodes. The reservoir was filled with electrolyte solution consisting. Two Pt wire electrodes located at the center of the cell and at each side of the sample served as the reference and sensing electrodes to measure the potential difference along across sample. A square-wave form of the current was applied through the coated Ti electrodes, and the potential difference was measured with the Pt wire electrodes. The resistance with and without the sample in the path was measured so that the MacMullin number can be obtained. It was found that the carbon-cloth GDLs follow the Bruggeman expression but the carbon-paper GDLs had a different relationship.

This difference can be explained in terms of the path length created by the orientation of the fibres in each type of GDL. The following equation was found to best fit the experimental data for carbon-paper GDLs:

$$N_M = \epsilon^{-3.8} \quad (1.15)$$

Using similar equipment, Kramer et al. [41] measured the effective ionic conductivity of electrolyte-soaked Toray-060 sample in both through-plane and in-plane direction at various compression levels using electrochemical impedance spectroscopy. To investigate the in-plane direction, the sample holder consists of two acrylic glass blocks. Two cavities are machined into the lower block and served as electrolyte inlet. Two Pt wires located at a distance of 3 cm served as potential probes. The sample was placed in-between. A glass frit was incorporated to enable compressing the GDL in the through-plane direction, while retaining uniform electrolyte entry. For porosities in the range of 0.5-0.8, the effective diffusion coefficient was found to be in the range of 0.2-0.6 for in-plane direction and 0.1-0.3 for through-plane direction.

Fluckiger et al. [42] extended the work of Kramer et al. [41] by studying the effect of PTFE content on the effective diffusivity. Untreated and PTFE-treated Toray-60 and SGL (24 and 25 series) were investigated. The effective diffusivity of Toray-60 sample was found to decrease with increasing PTFE loading in both in-plane and through-plane directions. However, the effective diffusivity of GDL 24 DA was slight higher than that of the untreated GDL 24 AA.

Zamel et al. [43] was the first to measure gas diffusion directly. They used a Loschmidt cell to measure the through-plane effective diffusion coefficient of Toray-120 with different PTFE loadings. The cell is made up of top and bottom chambers. A ball valve is used to connect the chambers or separate the chambers. The gas flow rate was controlled by two mass flow controllers that are connected to the inlets. An oxygen sensor is installed in the top chamber to measure the oxygen concentration. The through-plane diffusibility showed a linear downward trend with PTFE content and was measured to be in the range of 0.13-0.33 for PTFE loadings in the range of 0-40%.

Unsworth et al. [44] measured gas diffusion using a setup similar to Zamel et al. [43]. The modified correlation between the through-plane GDL diffusibility and porosity below was obtained. The relationship is only valid for carbon papers with less than 10% PTFE

loading.

$$f(\epsilon) = \left(1 - (2.72\epsilon)\cosh(2.53\epsilon - 1.61) \left(\frac{3(1 - \epsilon)}{3 - \epsilon} \right) \right) \quad (1.16)$$

Chan et al. [8] used the same Loschmidt cell to study the effect of MPL on the through-plane effective diffusion coefficient. The effective diffusivity was found to be around 42% of the corresponding effective diffusivity for the GDL substrate (SolviCore Type A, 5% PTFE).

Mangal et al. measured the through-plane diffusivity of GDL using the same diffusion bridge discussed before [27]. A differential pressure controlled was used to control the static pressure difference between the gas channels. A back pressure controller was connected to the nitrogen channel and used to control the static pressure of the system. An oxygen sensor probe was used to measure the oxygen concentration in the nitrogen channel. Diffusibility of the GDL was found to decrease with PTFE loading. In addition, they found that diffusibility of the GDL was independent on absolute pressure but the diffusibility for He-O₂ was significantly different from the diffusibility for N₂-O₂.

Gostick et al. [45] developed an in-plane diffusion bridge to measure the in-plane diffusivity of GDL. The GDL was compressed between two stainless steel plates and shims were used to control the thickness. The sample was flushed with nitrogen to set a zero oxygen initial condition. The experiment began the moment the flushing stopped, since oxygen immediately started to diffuse through both ends into the sample. An oxygen sensor probe placed at a fixed location inside the GDL recorded the oxygen concentration as a function of time. Fick's second law was solved for one dimension in order to estimate the effective diffusion coefficient. The in-plane effective diffusivities were found to decrease with higher compression level.

Even though many studies exist in literature measuring GDL effective diffusivities, measurements of CL diffusivity are sparse. Shen et al. [11] measured the effective diffusivity of catalyst layer using the modified Loschmidt cell discussed in Ref. [43]. An automated spray coater was employed to deposit CL onto an Al₂O₃ membrane substrate. For the catalyst layers under investigation the effective diffusivity was found to be $1.47 \pm 0.05 \times 10^{-7} \text{m}^2/\text{s}$. They found that Bruggeman's formula overestimates the effective diffusivity of CL because it fails to take into account the Knudsen effect, however Knudsen effects could not be separated from molecular diffusion effects.

Inoue et al. [46] studied the relationship between porosity and effective diffusivity of CL

using a diffusion bridge similar to the one discussed by Mangal et al [27]. Pure nitrogen and oxygen flowed over the surface of sample and the diffusion flux was obtained by downstream gas analysis using gas chromatography. For porosities in the range of 0.4-0.75, the diffusibility was reported from 0.01 to 0.3 and decreased with increasing ionomer-to-carbon ratio.

Yu and Carter [47] studied the effective diffusivity in electrodes using a conventional PEMFC platform with 50 cm² flow fields. Nitrogen flows through the middle channel and air through the two outer channels. Effective diffusivity of the electrodes was obtained by solving the Fick's first law. The effective diffusivity was found to decrease with higher ionomer-to-carbon ratio.

Zhao et al. [48] measured the permeability of CL using Darcy's law and reported effective gas permeability to be in the range of 1.5 - 3.7 × 10⁻¹⁵ m². However, the Knudsen diffusivity effect was ignored.

1.4.2.3 Mathematical studies on diffusivity

The effective diffusivity, D^{eff} , of partially wetted porous media is typically written as [29]:

$$D^{eff} = D_{bulk}f(\epsilon)g(s) \quad (1.17)$$

where $f(\epsilon)$ is a function of porosity representing the impact of the porous media structure and $g(s)$ is a function used to account for pore blockage due to water. ϵ is the porosity, s is the saturation and D_{bulk} is the bulk diffusivity of a pair of gases.

Bruggeman type approximation [49] is one of the most commonly used correlations that predict the effective diffusivity of porous media. Bruggeman equation was derived based on the effective medium approximation. Mathematically, the Bruggeman type approximation is written as:

$$D^{eff} = D_{bulk}(\epsilon)^a \quad (1.18)$$

where a is the fitting parameter.

Tomadakis and Sotirchos [50] applied percolation theory to predict the effective diffusion coefficient in porous media. A Monte Carlo simulation scheme was employed to determine the effective diffusion coefficient from the mean-square displacement of random walkers travelling

in the interior of porous structure. The equation is defined as:

$$D^{eff} = D_{bulk} \epsilon \left(\frac{\epsilon - \epsilon_p}{1 - \epsilon_p} \right)^\alpha \quad (1.19)$$

where parameters ϵ_p and α are fitting parameters.

In this thesis, the experimental results are used to fit in equation (1.18) and (1.19). Other models [51–54] to predict diffusivity will not be discussed in this section since this thesis mainly focuses on experimental measurement.

1.4 Research gap and objectives

Based on the literature review on transport properties of PEM fuel cell porous media, following research gaps are identified:

- The Knudsen effects under high GDL compression levels have not been studied. Some studies measured GDL under compressed state but in a small range of compression [19, 20]. Besides, even though the effect of PTFE content and MPL on GDL permeability and diffusivity have been studied, the effect of carbon matrix (see Figure 1.3) that results in a dual pore size distribution, has not been well studied.
- Even though some studies have measured CL diffusivity, CL permeability and Knudsen diffusivity have not been well studied. In addition, no studies have measured CL permeability, effective Knudsen diffusivity and diffusivity simultaneously.

The first goal of this thesis is to study the effect of carbon matrix and morphology on GDL transport properties. To achieve this goal, MIP technique is employed to obtain the PSD and volume fraction in matrix of GDLs. SEM imaging is also used for better observing the GDL pore structure. The GDL is measured in the in-plane direction at various thickness in order to study the effect of matrix and Knudsen effect. The second goal of this thesis is to measure the CL permeability, effective pore diameter, Knudsen diffusivity and effective diffusivity. The catalyst ink is prepared and printed by an inkjet printer. The effect of I/C ratio and different carbon support on the CL transport properties are studied. The CL is measured in the through-plane direction because of its thin thickness.

1.5 Thesis outline

The thesis consists of four chapters. Chapter 1 discusses motivation, background and literature review. Chapter 2 focuses on theory and measurements of GDL in-plane permeability and diffusivity. SEM images and PSD curves of measured GDL samples are also presented. Different GDL types are measured at various compression levels and the effect of carbon matrix and morphology are analysed based on experimental results. Chapter 3 looks at theory and measurements of transport properties of CL. Several CL types are fabricated using different Pt/C powder and ionomer-carbon ratio to study their effect on transport properties. Different gases, i.e., Krypton and CO₂ are used to validate the accuracy of Knudsen's expression. The diffusibility of CLs obtained from experiment is compared to literature. Chapter 4 talks about conclusions and future work.

Chapter 2

Measurement of in-plane PEM fuel cell gas diffusion layer gas transport properties

2.1 Introduction

Typical materials used as GDLs are carbon paper and carbon cloth which show anisotropic transport characteristics. Carbon paper has a high degree of in-plane alignment, increasing transport in this direction compared with through-plane [55]. In-plane transport is important for distributing gases beneath the flow-field ribs, facilitating a more uniform current-density across the cell, and increased durability [56] [57]. As a result, it is necessary to study the transport properties of GDL in the in-plane direction.

In this chapter, a metal diffusion bridge is introduced for measuring in-plane GDL transport properties. The setup was originally proposed by Mangal et al. [29], however, the experimental setup did not show good agreement with other literature. In this work, the setup was modified to increase accuracy. First, the back pressure and differential pressure controller were removed to reduce the uncertainty arising from equipment. Also, multiple layers of sample were stacked together for the measurement to reduce the uncertainty in thickness measurement and ensure sufficient oxygen transport through the sample. The new setup is more accurate and it is capable of reproducing previous literature results. As introduced in previous chapter, most literature studied the relationship between PTFE content and transport parameters, however, the effect of pore size distribution and carbon matrix were ignored. Recent GDL materials, such as SIGRACET 28 BA, have a large amount of

carbon matrix creating a dual pore size distribution. The impact of this additional material on transport properties has not been studied. The primary goal of this chapter is to study the effect of pore size distribution and carbon matrix on GDL transport properties.

Section 2.2 discusses the experimental setup for the in-plane permeability and effective molecular diffusivity. Section 2.3 describes the theory and mathematical models for estimating the gas transport properties. Section 2.4 discusses measurement uncertainty for in-plane GDL permeability and diffusivity. In section 2.5, GDL sample characterization is provided and the experimental results for Toray-90 samples are compared to literature to validate setup accuracy. Different GDL types were then measured and compared with each other to analyse the effect of pore size distribution and carbon matrix on transport properties.

2.2 Experimental setup

2.2.1 In-plane diffusion bridge

The in-plane diffusion bridge used in this thesis is made up of two steel plates with two circular flow channels machined into them, as shown in Figure 2.1. The diameter and length of the circular channel are 9 mm and 5 cm, respectively. Four shims of known thickness were placed between top and bottom plates in order to control the sample compression level. Two strips of silicon gaskets were placed around the flow channels to prevent leakage. To estimate the porosity of the compressed sample, it was assumed that compression only reduced the pore volume but not the solid volume. The porosity of a compressed sample is then calculated as:

$$\epsilon = 1 - (1 - \epsilon_o) \frac{t_o}{t} \quad (2.1)$$

where ϵ_o and t_o are the porosity and thickness of the uncompressed sample, and t is the thickness of sample in compressed state.

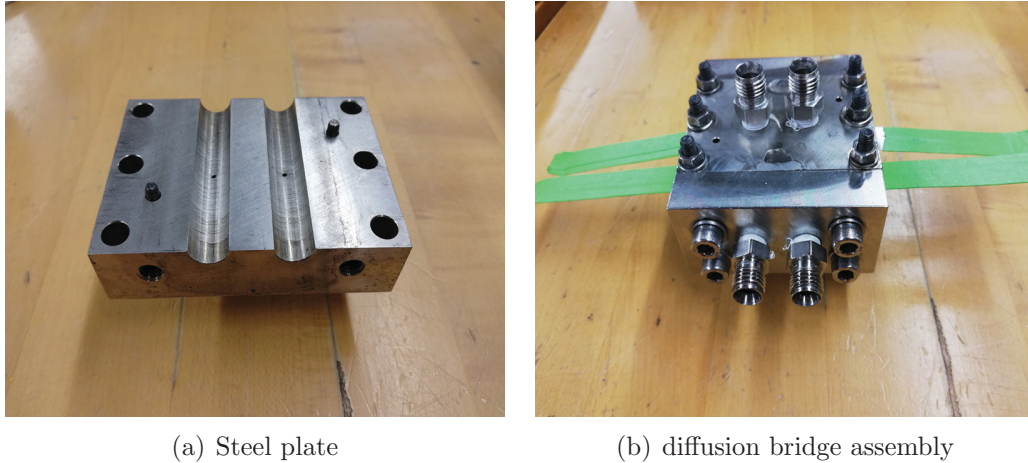


Figure 2.1: Photograph of (a) steel plate and (b) diffusion bridge assembly

2.2.2 Sample preparation

For the purpose of testing GDL, the sample was cut into $1 \times 5 \text{ cm}^2$ using a precision knife. Four layers of sample were stacked together and placed between the top and bottom plates. The bolts were then tightened using a torque value of 4.5 N-m (40 inch-lb) in a cross cyclic manner to create a uniform compression on the diffusion bridge. The final assembly is shown in Figure 2.1 (b). To detect leakage, the bridge was filled with nitrogen, pressurized up to 50 psig, and placed in water for 3 minutes. No bubbles were visible leaving the diffusion bridge, which proved that there was no leakage.

2.2.3 In-plane permeability

The in-plane diffusion bridge contains two channels and each channel has four ports. In the permeability experiment, one port of the channel is connected to the gas bottle via a mass flow controller (MFC) and another port is connected to the high pressure end of pressure transducer (PT). The other two ports of the channel are closed so that the gas is forced to flow from one channel to the other through the porous media in the in-plane direction. One port of low-pressure channel is then connected to the low-pressure port of the PT and the other ports are open to the atmosphere. A schematic diagram of the setup is shown in Figure 2.2.

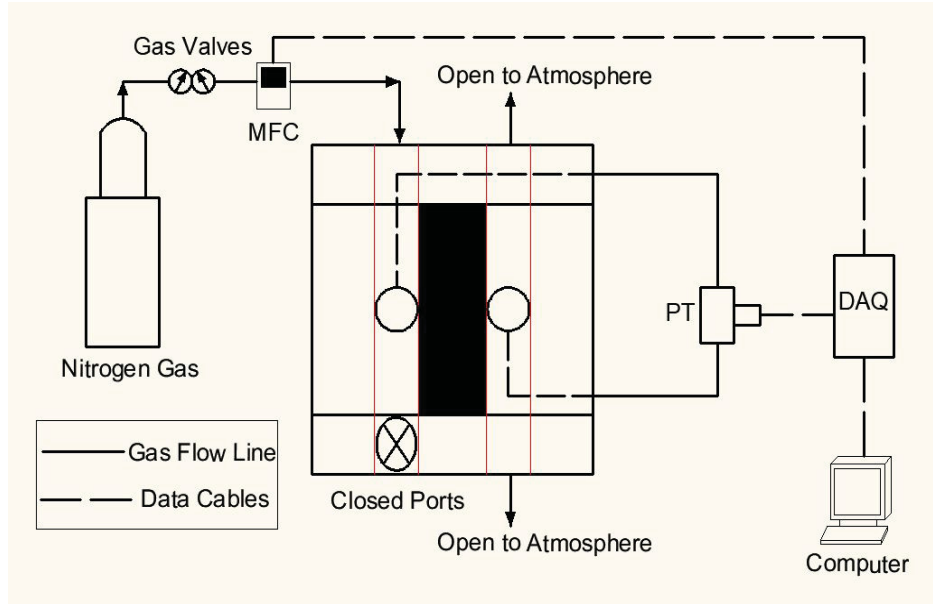


Figure 2.2: Experimental setup for in-plane permeability

Compressed nitrogen (PRAXAIR, UHP 5.0) from a gas cylinder at 50 psig flows to the mass flow controller (Cole-Parmer, Serial Number: 62704, range: 0-5 SLPM) which is used to control the gas flow rate. The pressure transducer (OMEGA, Serial Number: 418617, range: 0-3.5 bar) is connected to both channels so that the pressure drop across the porous media at different flow rates can be measured. The MFC is connected to a computer via an RS-232 communication port. A data acquisition card (National Instruments USB 6221) is used to read data from the PT. LabWindows/CVI is used to communicate with the setup and log data from the MFC and PT into a text file. The data is logged for 125 seconds (25 readings) for each flow rate to ensure steady state.

2.2.4 In-plane diffusivity setup

In the in-plane diffusivity experiment, nitrogen and oxygen gases enter each one of the channels. The two compressed gases are adjusted to 50 psi before flowing to the MFCs. Nitrogen (Cole-Parmer, Serial Number: 62704, range: 0-5 SLPM) and oxygen mass flow controllers (Cole-Parmer, Serial Number: 62661, range: 0-5 SLPM) are used to control the flow rate of the gases. The oxygen channel outlet is open to ambient and nitrogen channel outlet is connected to the oxygen sensor.

In contrast to the setup previous proposed by Mangal [28], the back pressure controller (BPC) and differential pressure controller (DPC) were not used in the in-plane diffusivity

measurement. There are mainly two reasons: (1) removing DPC and BPC simplified the setup and reduced the uncertainty arising from the controllers, and, (2) the increase in oxygen concentration of nitrogen channel is very small even for significant pressure difference. A schematic diagram of the setup is shown in Figure 2.3.

To measure the oxygen mole fraction in the gas mixture at the outlet of the nitrogen channel, a NEOFOX oxygen sensor (Ocean Optics, Model: FOSPOR-600-32MM, range: 0 - 21% in gas) is used. To achieve accurate measurements, the oxygen sensor is recalibrated every day before running the experiment. Two mass flow controllers are used to create a gas mixture of known oxygen concentration, and the results are compared to the measured oxygen levels by the NEOFOX sensor in order to calibrate the sensor by changing oxygen levels. Calibrated compressed nitrogen-oxygen gas mixtures (PRAXAIR, Accuracy: $\pm 2\%$ Rel) containing 1% and 10% oxygen are finally used to validate the calibration results. The sensor is considered to be properly calibrated when for the two different gas mixture, the measurement results are $1\% \pm 0.02\%$ and $10\% \pm 0.1\%$ respectively. The calibration file is uploaded in the NEOFOX software, and the calibration is done.

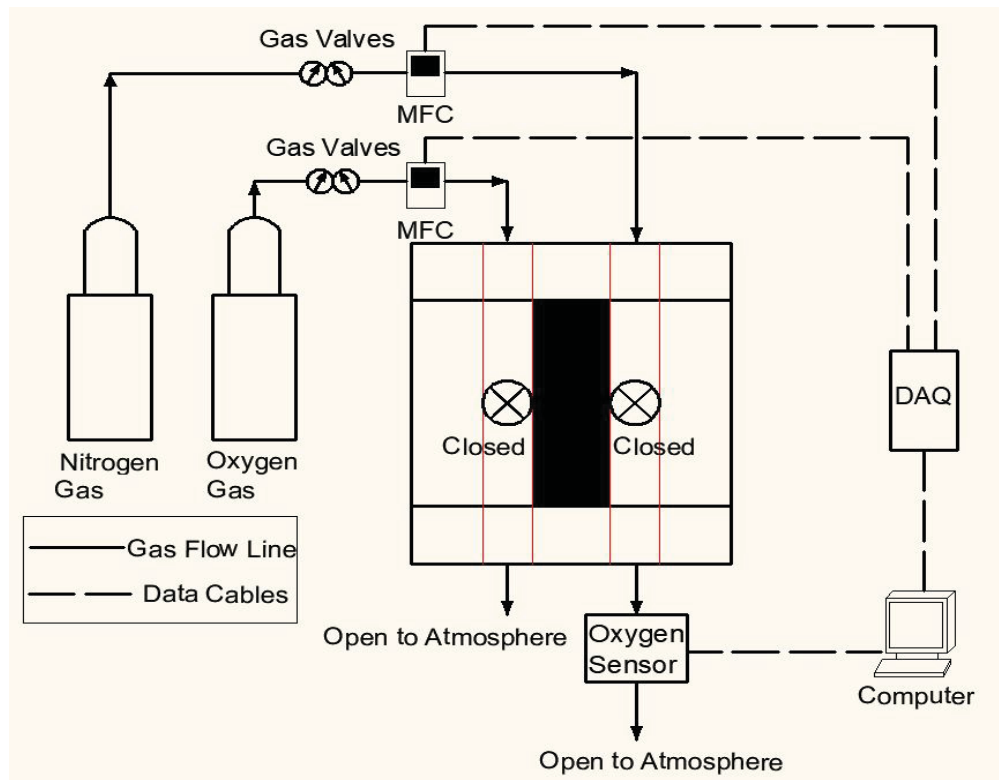


Figure 2.3: Experimental setup for in-plane diffusivity

The mass flow controller is connected to a computer via an RS-232 communication port.

A data acquisition card is used to read data from pressure transducer. LabWindows/CVI is used to communicate with the mass flow controller. The NEOFOX software logs data from the oxygen sensor and stores oxygen volume fraction vs. time in a CVS file every 5 seconds for 5 minutes after oxygen concentration is stabilized. Then the flow rate of the gas and average oxygen concentration are used for data processing.

2.2.5 Experimental conditions

To measure the in-plane permeability of GDL sample, the mass flow rate of nitrogen is varied from 0 to 1 standard liters per minute (SLPM) in 10 even intervals. The experiment is run at zero flow rate to estimate the offset of the PT.

In the in-plane diffusivity experiments, the mass flow rate of both gases is controlled to be 0.5 SLPM. Different flow rates were also used for validation and it was found that the in-plane diffusivity is almost independent on the flow rate. The details will be discussed in the next sections.

Unless otherwise stated, 4 layers of GDL samples are stacked together and tested at different compression levels. Experiments are also conducted using 2-layer sample and the number of layers was found to have no significant effect on permeability and diffusivity. Permeability and diffusivity experiments are performed three times using different samples. For each sample, the permeability and diffusibility are measured without opening/closing the diffusion bridge.

2.3 Governing equation and data analysis

2.3.1 Governing equation

2.3.1.1 Governing equation for in-plane permeability

Darcy's law is commonly used to describe the fluid flow through a porous media at low Reynolds number and is defined as [19]:

$$\nabla P = -\frac{\eta}{B_v} \mathbf{v} \quad (2.2)$$

where ∇P is pressure gradient across the porous media, η is the dynamic viscosity, \mathbf{v} is the velocity, and B_v is permeability of the porous media. For steady, one-dimension flow, the

equation is:

$$\frac{dP}{dx} = -\frac{\eta}{B_v}v \quad (2.3)$$

Darcy's law is well applicable for flow in porous media in the creep regime (Reynolds number < 10) [58]. As mass flow rate increases, the gas velocity also becomes higher in the porous media and inertial effects start to play a significant role. Inertial effects are taken into consideration by using the Darcy-Forcheimer equation [23]; which at steady-state, for one-dimension flow, reads:

$$\frac{dP}{dx} = -\frac{\eta}{B_v}v - \frac{\rho}{B_l}v^2 \quad (2.4)$$

where x is the coordinate taken as positive in the direction of gas flow, ρ is the density of a gas, and B_l is the inertial permeability (in m). Assuming ideal gas and substituting ideal gas law into equation (2.4) one finds:

$$\frac{dP}{dx} = -\frac{RT}{P} \left(\frac{\eta}{B_v}\dot{n} + \frac{M}{B_l}\dot{n}^2 \right) \quad (2.5)$$

where \dot{n} is molar flux ($\text{mol}/\text{m}^2 \text{ s}$). Rearranging equation (2.5) gives:

$$\frac{P}{RT}dP = - \left(\frac{\eta}{B_v}\dot{n} + \frac{M}{B_l}\dot{n}^2 \right) dx \quad (2.6)$$

In the absence of chemical reactions, the molar flux across the sample is constant. Integrating equation (2.6) from 0 to L and P_1 to P_2 , the compressible form of Darcy-Forcheimer equation can be expressed as [27]:

$$\frac{P_1^2 - P_2^2}{2RTL} = \frac{\eta}{B_v}\dot{n} + \frac{M}{B_l}\dot{n}^2 \quad (2.7)$$

where P_1 and P_2 are the pressure values in the high and low pressure channel respectively, \dot{n} is molar flux, T is the temperature in Kelvin, R is the gas constant, L is the thickness of the sample, and M is the molar mass of the gas. Equation (2.7) can also be written in terms of mass flux, \dot{m} , as

$$\frac{P_1^2 - P_2^2}{2RTL} M = \frac{\eta}{B_v}\dot{m} + \frac{1}{B_l}\dot{m}^2 \quad (2.8)$$

2.3.1.2 Governing equation for in-plane diffusivity

Fick's first law is widely used to estimate the diffusive flux of a species in a steady state system. In this case, Fick's first law is written in one dimension as [59]:

$$\dot{m}_i^D = -\rho_t D_{ij} \frac{dw_i}{dx} \quad (2.9)$$

where \dot{m}_i^D is the diffusion flux in $\text{kg}/\text{m}^2 \cdot \text{s}$, ρ_t is total density in kg/m^3 , D_{ij} is the diffusion coefficient or diffusivity in m^2/s . In porous media, D_{ij} is usually replaced by D_{ij}^{eff} in order to account for the porous media. In the experiment, oxygen is transported across the GDL by diffusion from the oxygen channel to the nitrogen channel. Assuming a linear variation in mass fraction, equation (2.9) can be written in discrete form as:

$$\dot{m}_{O_2}^D = D_{N_2, O_2}^{eff} \frac{\rho_t \Delta w_{O_2}}{L} \quad (2.10)$$

where $\dot{m}_{O_2}^D$ is superficial oxygen diffusive mass flux in GDL ($\text{kg}/\text{m}^2 \cdot \text{s}$), D_{N_2, O_2}^{eff} is the effective diffusivity of GDL sample, w_{O_2} is oxygen mass fraction, L is the thickness of sample and ρ_t is the interstitial gas mixture density in the sample. The latter is approximated to be $\frac{\rho_{O_2} + \rho_{N_2}}{2}$.

According to the mass conservation, the mass of oxygen that flows into the nitrogen channel through the GDL is equal to the mass of oxygen that leaves the nitrogen channel. For mass flux of oxygen flowing out of nitrogen channel is:

$$\dot{M}_{O_2}^{out} = \rho_{O_2} \dot{V}_{O_2} = \dot{V}_t x_{O_2} \rho_{O_2} \approx \dot{V}_{N_2} x_{O_2} \rho_{O_2} \quad (2.11)$$

where $\dot{M}_{O_2}^{out}$ is oxygen mass flux out of nitrogen channel (kg/s), x_{O_2} is oxygen molar fraction in nitrogen channel measured by oxygen sensor, \dot{V}_t is the volume flow rate of gas out of channel and \dot{V}_{N_2} is the volume flow rate of N_2 controlled by MFC (LPM). Equation (2.11) is based on the assumption that equal amount of N_2 diffuses through GDL into O_2 channel as O_2 diffuses through GDL into N_2 channel and convection has no contribution to the oxygen transport, then \dot{V}_{N_2} is approximately the same as the total volume rate in the N_2 channel.

As oxygen transport in the GDL is driven by diffusion, the mass flux of oxygen flowing into nitrogen channel through the GDL can be written as:

$$\dot{M}_{O_2}^{in} = D_{N_2, O_2}^{eff} A \frac{\rho_t \Delta w_{O_2}}{L} \quad (2.12)$$

where $\dot{M}_{O_2}^{in}$ is the oxygen diffusive mass flux into the nitrogen channel through the GDL (kg/s) and A is the cross-sectional area. Assuming w_{O_2} is 0 in the nitrogen channel and 1 in the oxygen channel, equation (2.12) results in:

$$\dot{M}_{O_2}^{in} = D_{N_2, O_2}^{eff} A \frac{\rho_t}{L} \quad (2.13)$$

According to mass conservation, $\dot{M}_{O_2}^{in} = \dot{M}_{O_2}^{out}$, then:

$$D_{N_2, O_2}^{eff} A \frac{\rho_t}{L} = \dot{V}_{N_2} x_{O_2} \rho_{O_2} \quad (2.14)$$

Assuming gas mixture density in the sample is equal to $\frac{\rho_{O_2} + \rho_{N_2}}{2}$, D_{N_2, O_2}^{eff} is finally written as:

$$D_{N_2, O_2}^{eff} = \frac{\dot{V}_{N_2} \rho_{O_2} x_{O_2} L}{A \rho_t} = \frac{2 \dot{V}_{N_2} \rho_{O_2} x_{O_2} L}{A (\rho_{O_2} + \rho_{N_2})} \quad (2.15)$$

Equation (2.15) is used to calculate the in-plane effective diffusivity of the GDL.

2.3.2 Data analysis

GDL permeability - In order to obtain viscous and inertial permeability in (2.7), the inlet pressure P_1 , and the molar flux of gas \dot{n} are measured. The molar flux \dot{n} in equation (2.7) is calculated using $\dot{n} = P_{standard} v / RT^\circ$, where $P_{standard}$ is the standard atmospheric pressure, i.e., 101325 Pa and T° is 298K. The inlet gas velocity, v , is obtained using $v = \frac{\dot{V}}{A}$, where \dot{V} is the volume flow rate at standard conditions controlled by the MFC in SLPM. P_1 is measured directly by the PT and P_2 is at ambient pressure. The experimental data is used to fit to equation (2.7) using a Python code to extract viscous permeability B_v and inertial permeability B_l . The code is used for the data fitting by employing a least squares regression technique. Simulations at different gas velocity with different permeability values are performed and a residual function is defined as:

$$Res = \sum_{i=10}^n (P_{1,exp} - P_{1,num}(B_v, B_l))^2 \quad (2.16)$$

where $P_{1,exp}$ is the experimental inlet pressure measured by PT, and $P_{1,num}$ is the numerical estimate of the inlet pressure obtained from equation (2.7). The values of B_v and B_l which minimize the residual function represent the permeabilities of GDL.

GDL diffusivity - In order to obtain the in-plane effective diffusivity of the GDL sample, the

volume flow rate of nitrogen and oxygen are controlled by two MFCs (Cole-Parmer, model: RK-32907-69, range: 0 - 5 SLPM) and the oxygen molar fraction in the nitrogen channel is measured by an oxygen sensor (Ocean Optics, Model: FOSPOR-600-32MM, range: 0 - 21% in gas). Assuming that the diffusive flux of oxygen and nitrogen across the CL sample are equal, and both of them are much less than the nitrogen flow from the MFC (details in results section), then the total volume flux in the nitrogen channel is considered to be approximately equal to the value from MFC. Therefore, the in-plane effective diffusivity can be obtained using equation (2.15).

2.4 Uncertainty analysis

To know the credibility of results and to learn how to improve the experiment, the influence of uncertainty in each variable on the experimental results is discussed. Suppose that f is a function of x_1, x_2, \dots, x_i , and the variables are measured with uncertainties $w_{x_1}, w_{x_2}, \dots, w_{x_N}$. If the uncertainties in x_1, x_2, \dots, x_N are independent and random, then the overall uncertainty w_f is [60]:

$$w_f = \sqrt{\left(\frac{\partial f}{\partial x_1} w_{x_1}\right)^2 + \left(\frac{\partial f}{\partial x_2} w_{x_2}\right)^2 + \dots + \left(\frac{\partial f}{\partial x_i} w_{x_N}\right)^2} \quad (2.17)$$

Systematic and precision uncertainties are two sources of uncertainty in the measurement. Systematic uncertainty is caused by measurement instruments and independent on repeated measurements, however precision uncertainty is caused by unknown and unpredictable changes in the experiment. Although manufacturers provide the accuracies of their equipment, most of them do not differentiate between systematic uncertainty and precision uncertainty [61]. Wheeler [62] recommends that manufacturer accuracy should be treated solely as systematic uncertainty because of the lack of a clear explanation of how to calculate the accuracies. Multiple precision experiments need to be performed before determining the overall uncertainty.

In a precision experiment, a fixed parameter is measured many times and the standard deviation of the measurements show the accuracy. Sample standard deviation S_x , is calculated using the mean value \bar{X} :

$$S_x = \sqrt{\frac{\sum_{j=1}^N (X_j - \bar{X})^2}{N - 1}} \quad (2.18)$$

where N is the sample size, X_j is the value of the j th measurement. For small sample size (less than 30), the t-distribution can be used and the precision uncertainty would be expressed in terms of S_x [61]:

$$P_x = t \frac{S_x}{\sqrt{N}} \quad (2.19)$$

where t is decided by sample size and level of confidence (in this case 95%), and N is the sample size.

After determining the precision uncertainty, the overall uncertainty for a single variable x can be calculated as:

$$w_x = \sqrt{B_x^2 + P_x^2} \quad (2.20)$$

where B_x is the systematic uncertainty provided by manufacturer and P_x is the precision uncertainty obtained from multiple experiments.

2.4.1 Mass flow controller uncertainty

The nitrogen and oxygen mass flow controllers are manufactured by Cole-Parmer. The range is 0-5 SLPM, and manufacturer accuracy is (0.8% of reading + 0.2% of full scale) for both controllers. Both controllers were calibrated with a bubble calibrator (Sensidyne, Gilibrator-2) which measures the volume flow rate based on the ideal gas law. Atmospheric pressure and temperature were measured before the calibration was conducted. The calibrator was connected to the outlet of the mass flow controller and 10 readings were recorded for each mass flow rate while nitrogen or oxygen is flowing through the calibrator. The largest sample standard deviation was calculated using equation (2.18), and precision uncertainty was then calculated to be 4.24×10^{-3} SLPM for both nitrogen and oxygen mass flow controller.

For the nitrogen MFC, none of the measured sample mean values fell within the manufacturer accuracy. A calibration curve was generated, shown in Figure 2.4, using 110 measurements. X and Y axis represent set point and actual value, respectively. A correlation equation for nitrogen MFC was obtained as:

$$V_{N_2,real} = 1.0291 * V_{N_2,set} + 0.0205 \quad (R^2 = 0.9999) \quad (2.21)$$

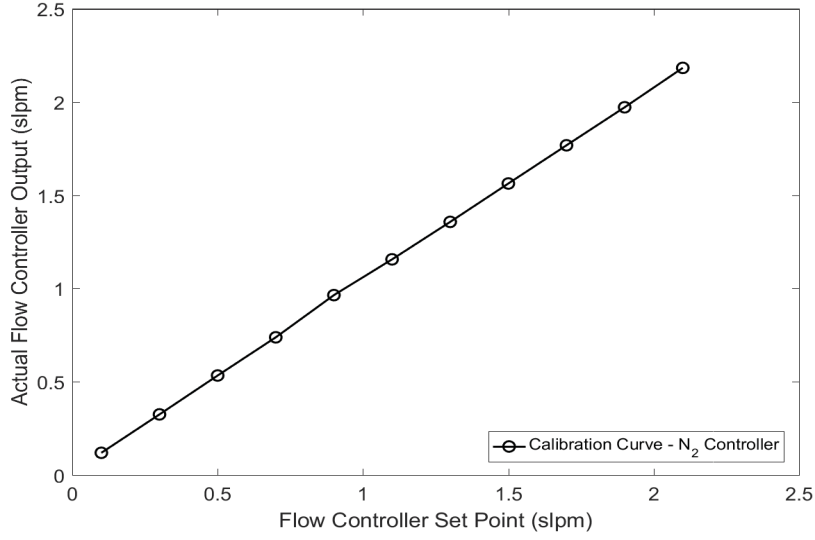


Figure 2.4: Nitrogen mass flow controller calibration curve

The standard error estimate is given by equation (2.22) and an equivalent uncertainty in the slope is expressed as equation (2.23) [62]:

$$\sigma_y = \sqrt{\frac{\sum_{i=1}^N (y_i - Y_i)^2}{N - 2}} \quad (2.22)$$

$$\sigma_{ye} = a\sigma_x \quad (2.23)$$

where N is equal to 110 since 10 readings were recorded at each flow rate and 11 different set point flow rates were measured, y_i is the measured value, Y_i is the predicted value obtained by correlation equation (2.21), a is the slope of the calibration curve, and σ_x is the factory accuracy at set point. The new systematic uncertainty is then calculated as:

$$w_{N_{N_2}} = \sqrt{\sigma_y^2 + \sigma_{ye}^2} \quad (2.24)$$

The overall uncertainty of the nitrogen MFC at different mass flow rate is calculated by equation (2.20) and shown in Table 2.1.

Table 2.1: Uncertainties in nitrogen mass flow controller (Unit in SLPM)

Mass Flow Rate	Manufacturer Systematic Uncertainty	New Systematic Uncertainty	Precision Uncertainty	Overall Uncertainty
0.1	0.0108	0.0130	4.24×10^{-3}	0.0136
0.3	0.0124	0.0128	4.24×10^{-3}	0.0135
0.5	0.0140	0.0144	4.24×10^{-3}	0.0150
0.7	0.0156	0.0160	4.24×10^{-3}	0.0165
0.9	0.0172	0.0177	4.24×10^{-3}	0.1820
1.1	0.0188	0.0193	4.24×10^{-3}	0.0197
1.3	0.0204	0.0210	4.24×10^{-3}	0.0214
1.5	0.0220	0.0230	4.24×10^{-3}	0.0233
1.7	0.0236	0.0240	4.24×10^{-3}	0.0243
1.9	0.0252	0.0260	4.24×10^{-3}	0.0263
2.1	0.0268	0.0276	4.24×10^{-3}	0.0279

The overall uncertainty of oxygen MFC can be obtained following the same procedure. The calibration curve is shown in Figure 2.5. The overall uncertainty of oxygen MFC is obtained by following the same procedure and shown in Table 2.2.

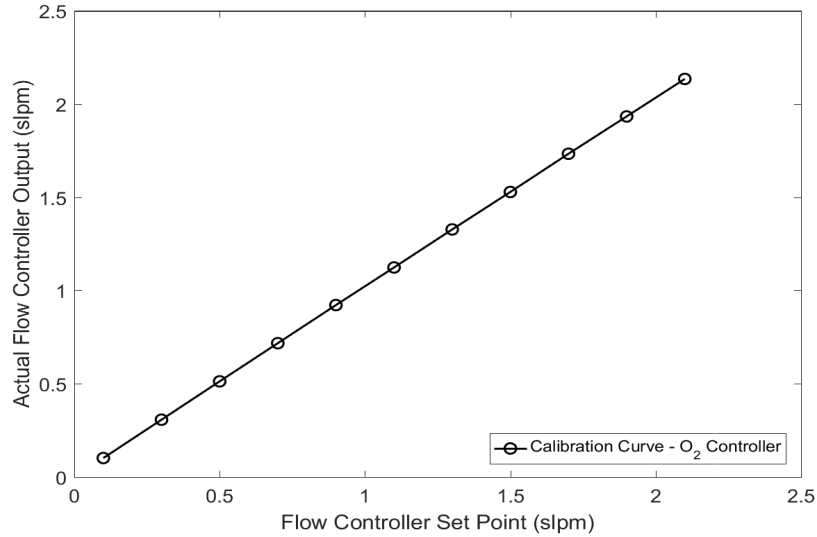


Figure 2.5: Oxygen mass flow controller calibration curve

Table 2.2: Uncertainties in oxygen mass flow controller (Unit in SLPM)

Mass Flow Rate	Manufacturer Systematic Uncertainty	New Systematic Uncertainty	Precision Uncertainty	Overall Uncertainty
0.1	0.0108	0.0110	4.24×10^{-3}	0.0117
0.3	0.0124	0.0126	4.24×10^{-3}	0.0132
0.5	0.0140	0.0142	4.24×10^{-3}	0.0148
0.7	0.0156	0.0158	4.24×10^{-3}	0.0164
0.9	0.0172	0.0175	4.24×10^{-3}	0.1790
1.1	0.0188	0.0191	4.24×10^{-3}	0.0195
1.3	0.0204	0.0207	4.24×10^{-3}	0.0210
1.5	0.0220	0.0223	4.24×10^{-3}	0.0227
1.7	0.0236	0.0240	4.24×10^{-3}	0.0243
1.9	0.0252	0.0256	4.24×10^{-3}	0.0259
2.1	0.0268	0.0272	4.24×10^{-3}	0.0275

2.4.2 Pressure transducer uncertainty

The pressure transducer is manufactured and factory calibrated by Omegadyne Inc. It has an accuracy of 0.05% of full scale= $0.05\% \times 3.5 \text{ bar} = 175 \text{ Pa}$. To perform precision experiment, the PT was used to measure the pressure drop across the GDL. The mass flow controller was set at different flow rates to create different pressure drops. The readings were recorded 60 times for each set point and the precision uncertainty was found to be 14.2 Pa using equation (2.19). Then the overall uncertainty of the PT was calculated as:

$$w_{PT} = \sqrt{B_{PT}^2 + P_{PT}^2} = \sqrt{175^2 + 14.2^2} = 175.6 \text{ Pa} \quad (2.25)$$

2.4.3 Oxygen sensor uncertainty

The oxygen sensor was manufactured and calibrated by NEOFOX (Ocean Optics, Model: FOSPOR-600-32MM, range: 0-21%). To achieve accurate measurement, the oxygen sensor is recalibrated every time before the experiments are performed. The calibration method has been discussed in the previous section. A calibration curve of actual reading vs. set point is shown in Figure 2.6 and correlation equation for oxygen sensor is obtained as:

$$y = -0.0065x^2 + 0.9289x - 0.8338 \quad (R^2 = 1) \quad (2.26)$$

The x represents oxygen sensor reading and y represents actual value. It is obvious to see that there is an offset at $y = 0$ and this offset is eliminated by the fitting. Two calibrated compressed nitrogen-oxygen gas mixtures (PRAXAIR, Accuracy: $\pm 2\%$ Rel) containing 1% and 10% oxygen are finally used to validate the calibration results. The sensor is considered to be properly calibrated when for the two different gas mixture, the measurement results are $1\% \pm 0.02\%$ and $10\% \pm 0.1\%$ respectively. The average uncertainty was taken as 5%.

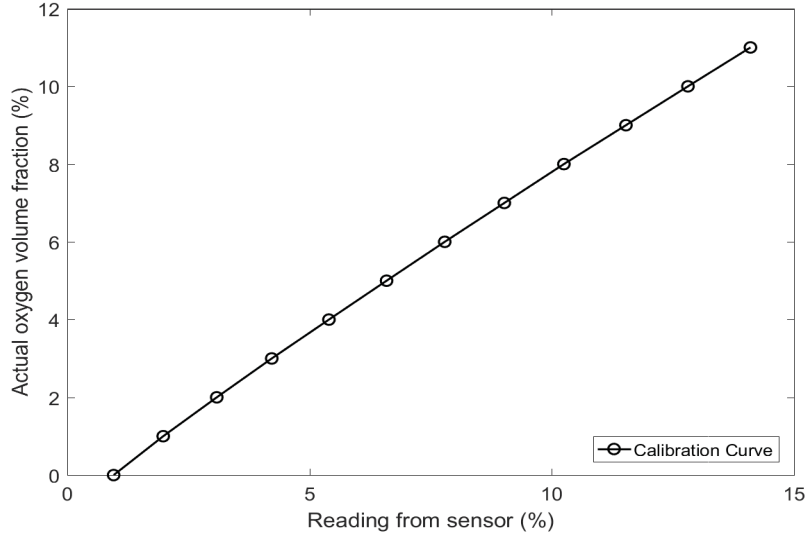


Figure 2.6: Oxygen sensor calibration curve

2.4.4 Thickness measurement uncertainty

The thickness of sample is controlled by incompressible metal shims (TBI FPSM-20). The shims of thickness 50, 100, 250 and 400 μm are measured by a micrometer (Mitutoyo Japan, Series NO.:008395) with an reported accuracy 2 μm . The measured results for the shims are 52.8 ± 0.83 , 102.8 ± 0.45 , 252.4 ± 0.55 and 399.6 ± 1.52 μm respectively. To be conservative, the uncertainty in thickness is taken as 4 μm .

2.4.5 Permeability uncertainty

Based on the discussion above, the uncertainty in function f is computed using the uncertainties in each variable, shown as equation (2.17). Applying this method to permeability equation (2.7) and ignoring the inertial effect due to its insignificant effect on permeability, permeability can be expressed as:

$$B_v = 2RT\eta \left(\frac{\dot{n}L}{P_1^2 - P_2^2} \right) \quad (2.27)$$

Taking R , T , η and P_2 as constants, the permeability uncertainty is given as:

$$w_{B_v} = 2RT\eta \sqrt{\left(w_{\dot{n}} \frac{L}{P_1^2 - P_2^2} \right)^2 + \left(w_L \frac{\dot{n}}{P_1^2 - P_2^2} \right)^2 + \left(w_{\Delta P_{PT}} \frac{2\dot{n}LP_1}{(P_1^2 - P_2^2)^2} \right)^2} \quad (2.28)$$

using $P_1 = P_2 + \Delta P_{PT}$ and equation (2.27), equation (2.28) can be rearranged to give:

$$\frac{w_{B_v}}{B_v} = \sqrt{\left(\frac{w_N}{N}\right)^2 + \left(\frac{w_L}{L}\right)^2 + \left(\frac{2w_{\Delta P_{PT}}}{\Delta P_{PT}} \frac{(P_2 + \Delta P_{PT})}{(2P_2 + \Delta P_{PT})}\right)^2} \quad (2.29)$$

In the in-plane permeability experiment, the flow rate, N varies from 0 - 1 SLPM. According to the overall uncertainty provided in Table 2.1 and 2.2, the average overall uncertainty in flow rate is taken as 4%. The average pressure drop measured in the study is several thousand pascals or higher, therefore the overall uncertainty in ΔP_{PT} is taken as 2%. Sample width, L , is measured using a micrometer gauge, and the uncertainty is very small uncertainty is very small and taken as 1%. As ΔP_{PT} is several thousand pascals or higher, the value of $\frac{(P_2 + \Delta P_{PT})}{(2P_2 + \Delta P_{PT})}$ can only go as high as 1. Take the maximum value, then the overall uncertainty for in-plane permeability of GDL will be:

$$\frac{w_{B_v}}{B_v} = \sqrt{(4\%)^2 + (1\%)^2 + (2\%)^2} = \pm 4.58\% \quad (2.30)$$

2.4.6 Experimental permeability precision uncertainty

In order to experimentally measure the permeability precision uncertainty of the setup, six experiments were repeated for the same material and the results were compared. A Toray-90 sample was measured at two different thickness and the results are shown in Table 2.3. The in-plane permeability for Toray-90 are 10.95 ± 0.105 and $5.17 \pm 0.03 \times 10^{-12} (m^2)$ at porosity 0.768 and 0.713 respectively. The standard deviation was calculated using equation (2.18), therefore P_x in equation (2.19) is calculated to be 0.105 and 0.03 respectively. The measurement uncertainty, P_x/B_v is calculated to be 0.96% and 0.58%, thus the setup precision is better than the theoretical precision calculated using equation (2.30).

Table 2.3: Toray-90 in-plane permeability at two different porosities

	Porosity	$B_v(N_2) \times 10^{-12}(m^2)$
Measurement 1	0.77	11.00
Measurement 2	0.77	11.00
Measurement 3	0.77	10.90
Measurement 4	0.77	11.10
Measurement 5	0.77	10.80
Measurement 6	0.77	10.90
	Porosity	$B_v(N_2) \times 10^{-12}(m^2)$
Measurement 1	0.71	5.15
Measurement 2	0.71	5.15
Measurement 3	0.71	5.22
Measurement 4	0.71	5.20
Measurement 5	0.71	5.17
Measurement 6	0.71	5.17

2.4.7 Diffusivity uncertainty

GDL in-plane effective diffusivity is calculated using equation (2.15). Using the same method shown in the previous section, the in-plane diffusivity overall uncertainty is calculated as:

$$w_{D_{N_2, O_2}^{eff}} = \frac{2\rho_{O_2}}{\rho_{O_2} + \rho_{N_2}} \sqrt{\left(w_{\dot{V}} \frac{x_{O_2} L}{A}\right)^2 + \left(w_{x_{O_2}} \frac{\dot{V} L}{A}\right)^2 + \left(w_L \frac{x_{O_2} \dot{V}}{A}\right)^2 + \left(w_A \frac{x_{O_2} \dot{V} L}{A^2}\right)^2} \quad (2.31)$$

Dividing both side by D_{N_2, O_2}^{eff} gives:

$$\frac{w_{D_{N_2, O_2}^{eff}}}{D_{N_2, O_2}^{eff}} = \sqrt{\left(\frac{w_{\dot{V}}}{\dot{V}}\right)^2 + \left(\frac{w_{x_{O_2}}}{x_{O_2}}\right)^2 + \left(\frac{w_L}{L}\right)^2 + \left(\frac{w_A}{A}\right)^2} \quad (2.32)$$

Here are four terms of uncertainties: (1) the overall uncertainty in flow rate is 4% under experimental condition, (2) the overall uncertainty in oxygen sensor is 5% of reading, (3) the uncertainty in the shims is taken as 4 μm and so the uncertainty in thickness is assumed to be 1%, and (4) the error in cross-sectional area is 4%. Substituting all the values into (2.32) gives the overall uncertainty of in-plane diffusivity of GDL:

$$\frac{w_{D_{N_2, O_2}^{eff}}}{D_{N_2, O_2}^{eff}} = \sqrt{(4\%)^2 + (5\%)^2 + (1\%)^2 + (4\%)^2} = \pm 7.6\% \quad (2.33)$$

2.4.8 Experimental diffusivity precision uncertainty

In order to experimentally measure the diffusivity precision uncertainty of the setup, three experiments were repeated for the same material and the results were compared. A Toray-90 sample was measured at two different thickness and the experimental raw data as well as results are shown in Table 2.4. The in-plane diffusibilities for Toray-90 are 0.432 ± 0.004 and 0.393 ± 0.005 at porosity 0.77 and 0.71 respectively. The standard deviation was calculated using equation (2.18), therefore P_x in equation (2.19) is calculated to be 0.004 and 0.005 respectively. The measurement uncertainty, P_x/B_v is calculated to be 0.93% and 1.27%, thus the setup precision is better than the theoretical precision calculated using equation (2.33).

Table 2.4: Toray-90 in-plane diffusibility at two different porosities

	Porosity	Oxygen level	Diffusibility
Measurement 1	0.77	0.58%	0.43
Measurement 2	0.77	0.58%	0.43
Measurement 3	0.77	0.58%	0.43
Measurement 4	0.77	0.59%	0.44
Measurement 5	0.77	0.58%	0.43
Measurement 6	0.77	0.58%	0.43
	Porosity	Oxygen level	Diffusibility
Measurement 1	0.71	0.42%	0.39
Measurement 2	0.71	0.42%	0.39
Measurement 3	0.71	0.42%	0.39
Measurement 4	0.71	0.43%	0.40
Measurement 5	0.71	0.43%	0.40
Measurement 6	0.71	0.42%	0.39

2.5 Results and discussion

Experiments are first performed on GDL samples with data available in literature. After making sure that the results were in good agreement with literature, the in-plane transport properties of several GDL samples are obtained. It is known that the gas transport properties of GDLs are dependent on the pore structure and overall porosity. As a result, investigating the pore structure and pore size distribution is helpful for us to fully understand the porous media in PEM fuel cell. The method of mercury intrusion porosimetry (MIP) was used to measure the porosity and pore size distribution. SEM images are also provided in order to better understand the pore structure of the GDL sample under study.

2.5.1 GDL sample characterization

MIP is commonly used by researchers to measure the porosity and pore size distribution of GDLs [63] [64]. In this study, porosimetry tests were conducted by Wei Fei (a PhD student in the group) using a PoreMaster 33 Mercury Porosimeter (Quantachrome Instruments).

Washburn equation is used to correlate the pressure applied to force the mercury into the pores in the sample to the pore size. The equation is given as:

$$r_p = -\frac{2\gamma\cos(\theta)}{P} \quad (2.34)$$

where P is the applied pressure, r_p is the pore radius, γ is the surface tension of mercury and θ is the contact angle between the mercury and the sample material. For the GDL samples, γ and θ were taken as 480 ergs/cm² and 140°, respectively.

The relation between logarithmic pore size distribution, $\frac{DX}{D(\ln(r_p))}$, and a given pressure P_i normalized with respect to total sample volume can be expressed using the following equation [29]:

$$\frac{DX}{D(\ln(r_p))} = \frac{(V_i - V_{i-1})/V_{pore}}{\ln(P_i) - \ln(P_{i-1})} \quad (2.35)$$

where X is the cumulative pore volume fraction, V_i is the volume of mercury intruded into the cell corresponding to pressure P_i , V_{pore} is the total volume of mercury intruded. The $\frac{DX}{D(\ln(r_p))}$ vs. pore radius is plotted to show the pore size distribution curve.

Figure 2.7 shows the pore size distribution curves for the GDL samples under study. The BA series GDL samples show a dual pore size distribution, in contrast, Toray-90 and Freudenberg GDL samples show a single pore size distribution. For BA series GDLs, the peak that appears between 0.1 μ m and 2 μ m is considered to be caused by the carbon matrix inside the GDL. To better understand the pore structure, SEM images (obtained by PhD student Manas Mandal) are shown in Figure 2.8. Carbon matrix/resins can be clearly seen in BA series samples and very small pores can be found in the matrix under high magnification (see Figure 2.9). It is interesting to see that Freudenberg H2315 shows a uniquely entangled fibre structure.

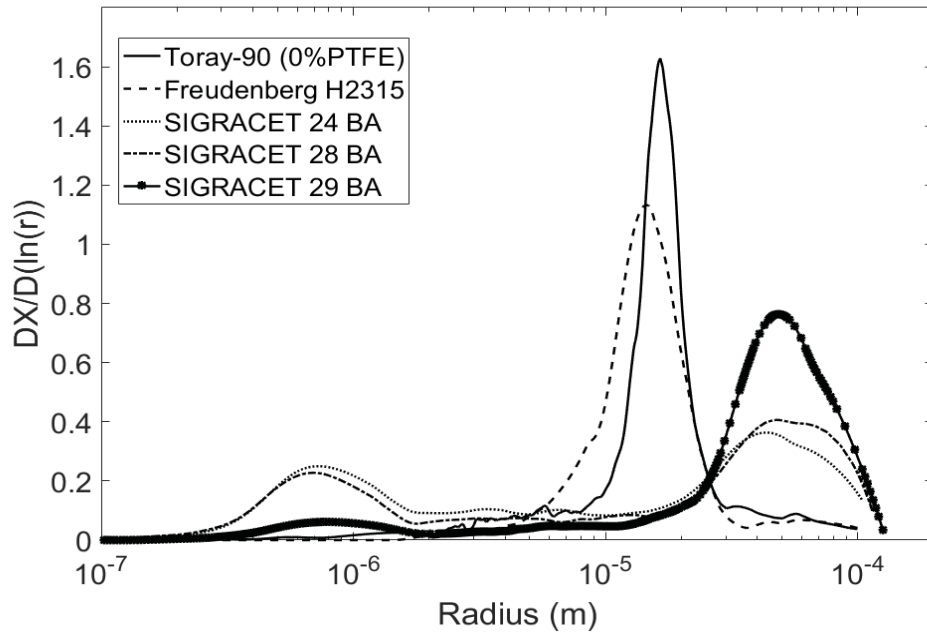
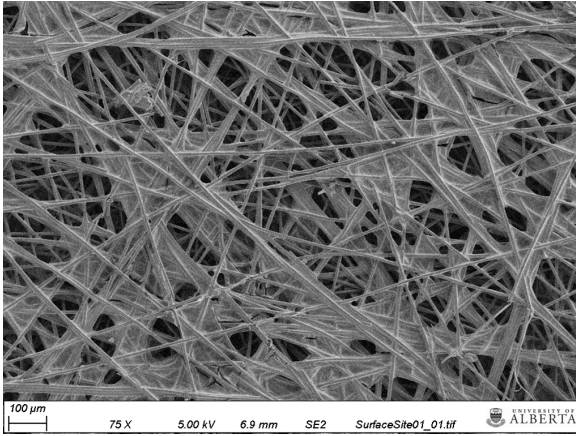
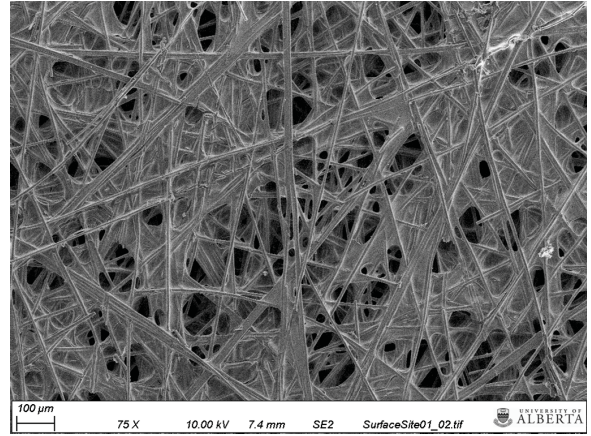


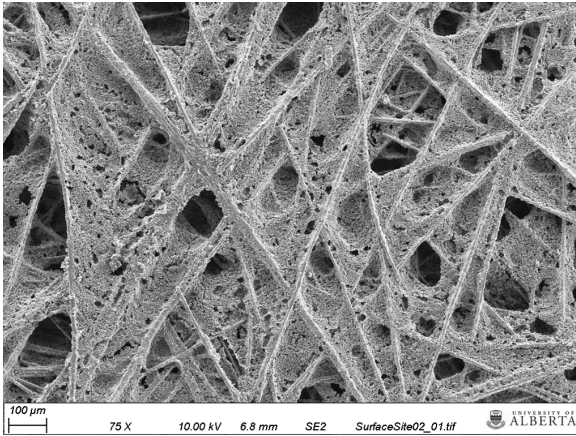
Figure 2.7: GDL pore size distribution



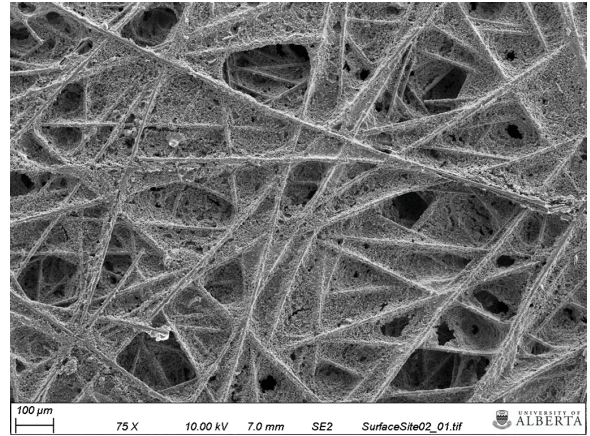
(a) Toray-90 (0%PTFE)



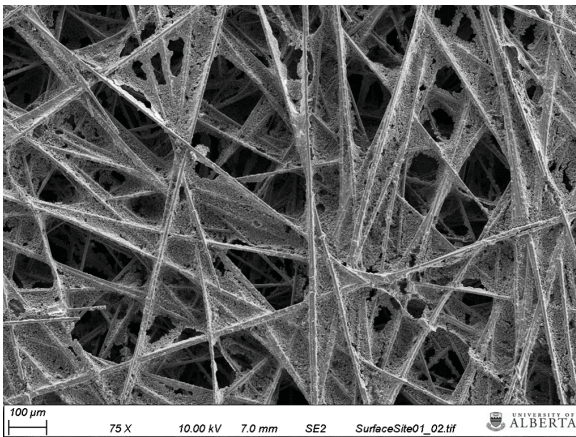
(b) Toray-90 (20%PTFE)



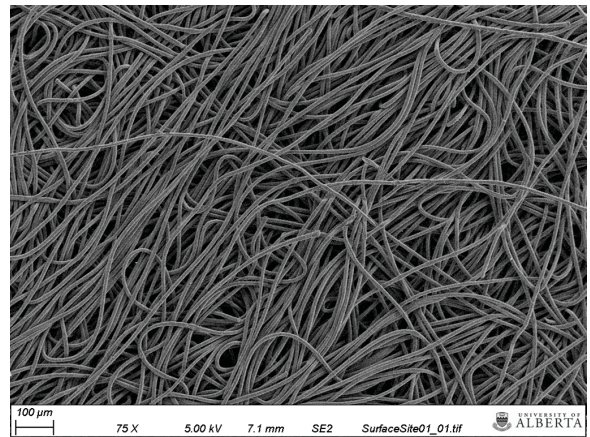
(c) SIGRACET 24 BA



(d) SIGRACET 28 BA



(e) SIGRACET 29 BA



(f) Freudenberg H2315

Figure 2.8: GDL SEM images: (a) Toray-90 (0%PTFE), (b) Toray-90 (20%PTFE), (c) 24 BA, (d) 28 BA, (e) 29 BA, (f) H2315

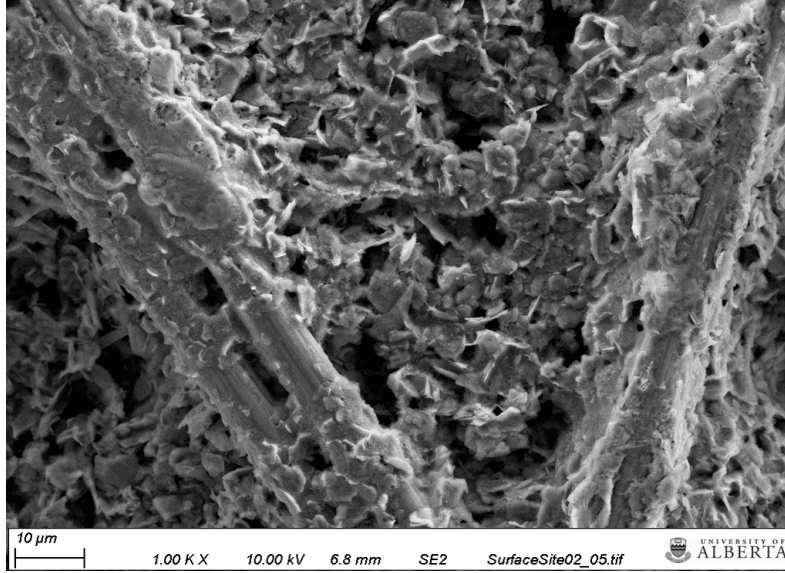


Figure 2.9: Carbon matrix structure in BA series GDL

The following parameters are needed for data analysis: 1) porosity, 2) volume fraction in carbon matrix, 3) fibre diameter. The porosity and volume fraction in carbon matrix can be obtained by PSD curve and the fibre diameter can be measured using SEM images. The calculation is done and provided by Wei Fei (a PhD student in the ESDLab group). The properties of the samples used in this thesis are shown in Table 2.5 and volume fraction in carbon matrix is defined as the volume fraction of pores between 0.1 and 2 μm . Among all the SGL GDL samples, 29 BA shows the smallest amount of matrix porosity, i.e., 5.3% of volume fraction of pores between 0.1 - 2 μm and 24 BA has the largest amount of matrix. Toray-90 and Freudenberg H2315 GDLs do not show any carbon matrix. In terms of maximum pore diameter, Figure 2.7 shows that BA series GDL show a larger value than Toray-90 and H2315.

Table 2.5: Properties of samples used in the study

Sample	Thickness (μm)	Porosity (%)	Volume fraction in carbon matrix	Fibre diameter (μm)
Toray-90 (0%PTFE)	290.0 \pm 3.0	79.5 \pm 0.5	0%	7.4 \pm 0.4
Toray-90 (20%PTFE)	289.0 \pm 4.0	70.0 \pm 1.0	0%	7.4 \pm 0.4
H2315	210.5 \pm 6.0	78.5 \pm 0.4	0%	10.5 \pm 0.2
SGL-24BA	187.8 \pm 3.0	75.3 \pm 3.4	26.5%	7.6 \pm 0.3
SGL-28BA	179.5 \pm 0.2	71.0 \pm 2.2	19.8%	6.5 \pm 0.3
SGL-29BA	193.3 \pm 0.7	84.0 \pm 2.9	5.3%	8.5 \pm 0.2

2.5.2 GDL in-plane permeability

2.5.2.1 Validation studies: Toray-90 GDL in-plane permeability and comparison with literature

To validate the reliability of the measurement, the in-plane permeability of Toray-90 samples are measured and compared with previous literature results. The sample is measured at various thickness in order to estimate the in-plane permeability vs. porosity curve. Three replicates are measured and results showed excellent repeatability (see Figure 2.10). Figure 2.11 shows that Toray-90 samples are also in good agreement with literature results at all porosities. It is therefore assumed that the experimental setup has excellent precision (Figure 2.10) and good accuracy (Figure 2.11).

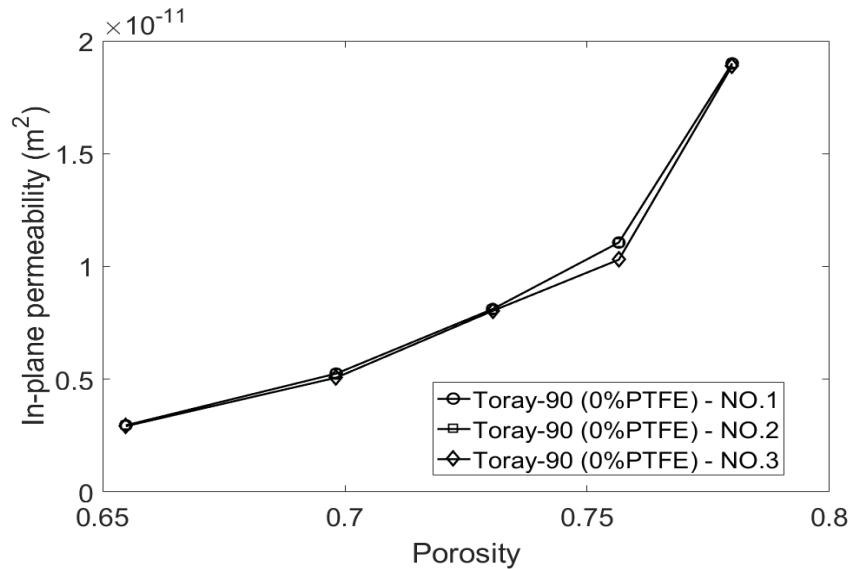


Figure 2.10: In-plane permeability results for untreated Toray-90

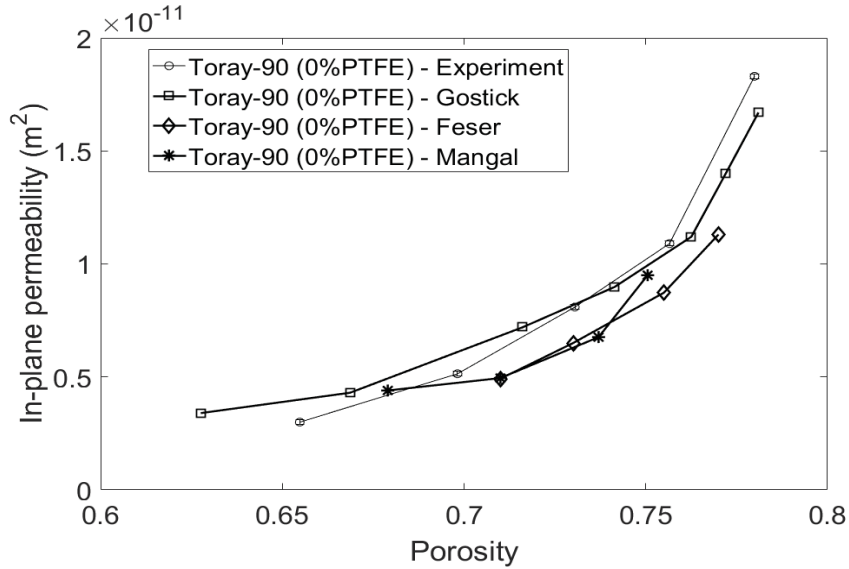


Figure 2.11: Experimental results for in-plane permeability at various porosities and literature results (Gostick [19], Feser [4], Mangal [28])

2.5.2.2 Validation studies: Effect of gas flow rate on permeability

The maximum gas flow rates are varied to study the effects of gas flow rate on permeability results. An untreated Toray-90 sample is tested at porosity 0.78 with maximum gas flow rate of 0.5, 1 and 2 SLPM. Table 2.7 shows the permeability does not change with gas flow rate.

Table 2.7: In-plane permeability of Toray-90 at different gas flow rate (porosity: 0.78)

Gas Flow Rate	$B_v(N_2) \times 10^{-11}(m^2)$
0.5	1.89 ± 0.02
1	1.86 ± 0.02
2	1.87 ± 0.02

2.5.2.3 In-plane permeability of different types of GDL samples

The GDL samples tested in this study include 24 BA, 28 BA, 29 BA, Toray-90 (0%PTFE), Toray-90 (20%PTFE) and Freudenberg H2315. The reason of choosing different samples is to study the effect of morphology and carbon matrix on the in-plane permeability. The in-plane permeability of all measured samples are shown in Figure 2.12. It is shown that compression has a negative influence on the in-plane permeability. Also, the GDL samples with a high matrix loading, such as 24 BA and 28 BA, show a rapid decrease in permeability with decreasing porosity. The reason is that 24 BA and 28 BA have a high volume fraction

in carbon matrix and relatively low volume fraction in carbon fiber, and when the samples get compressed, the big pores in carbon fibre get compressed first and as a result, the volume fraction in carbon fibre decreases faster for 24 BA and 28 BA. As shown in Figure 2.13, as compression level increases (porosity < 0.6 to 0.65), 24 BA exhibits the lowest permeability, followed by 28 BA. This indicates that carbon matrix has an adverse effect on permeability, especially at low porosities.

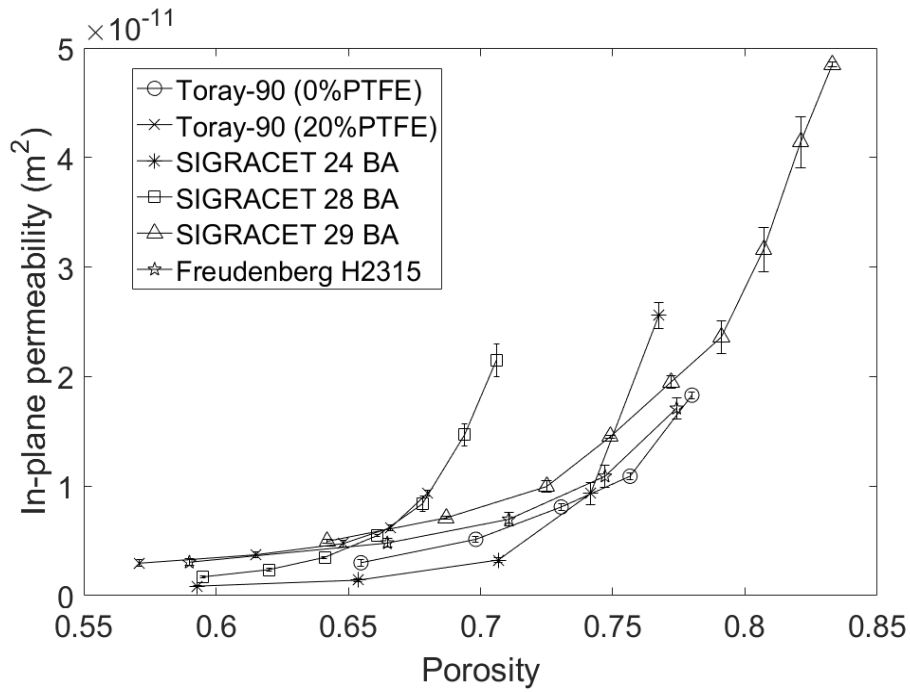


Figure 2.12: In-plane permeability of different type of GDL samples

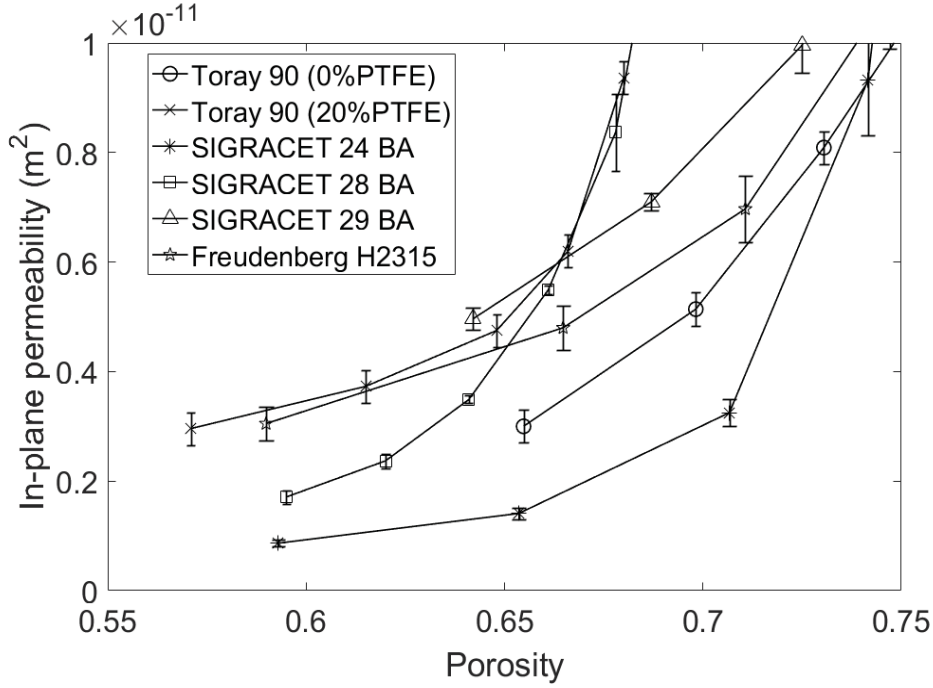


Figure 2.13: In-plane permeability of different type of GDL samples at porosity 0.55 to 0.75

2.5.2.4 Permeability obtained using helium as working gas

In theory, the permeability of the GDL is not expected to vary with different working gases. As discussed in the first chapter, Darcy's law is only accurate in continuum regime where the gas mean free path is much smaller than GDL pore diameter, i.e., Knudsen number $Kn < 0.001$. However, the pore diameter has an inverse relation with increasing compression level and gas flow would experience a transition from continuum region to transition region where Knudsen slip/diffusivity needs to be considered. Under compressed state, Knudsen slip will be particularly important in the carbon matrix which contains a lot of small pores. Assuming a GDL matrix pore diameter of $1 \mu\text{m}$, the Knudsen number is 0.06 for N_2 and 0.2 for He respectively, as a result, the gas flow in carbon matrix is in transition region. Therefore, it is necessary to study when Knudsen effects will become important to permeability and its effect can be studied by using different gases with varying gas mean free path.

Figure 2.14 shows the ratio of $B_v(He)$ to $B_v(N_2)$ at different compression levels for different GDL samples. The X-axis represents percentage of compressed volume, i.e., $(V_o - V_c)/V_o$ where V_o is uncompressed volume and V_c is the volume in compressed state. The data in the figure basically provides the following conclusions: (1) At small compression level ($< 10\%$), all the samples show very small ratio, i.e., $B_v(He) = B_v(N_2)$, which illustrates that the

gas permeability is mainly dependent on big pores and the small pores in the carbon matrix have little effect, (2) At high compression level ($> 40\%$), 24 BA and 28 BA which contain a large amount of porosity in the carbon matrix (see Table 2.5), show a bigger ratio than other GDL types, which proves that Knudsen slip is more significant and therefore transport in the small pores in the matrix becomes significant, (3) Even though 29 BA has 5.3% of volume in matrix and Toray-90 (0%PTFE) and H2315 do not show any matrix, 29 BA still shows smaller Knudsen slip compared to the other two because it has a larger maximum pore diameter. Therefore, the GDL permeability and Knudsen effects are dependent on a combination effect of matrix and pore diameter.

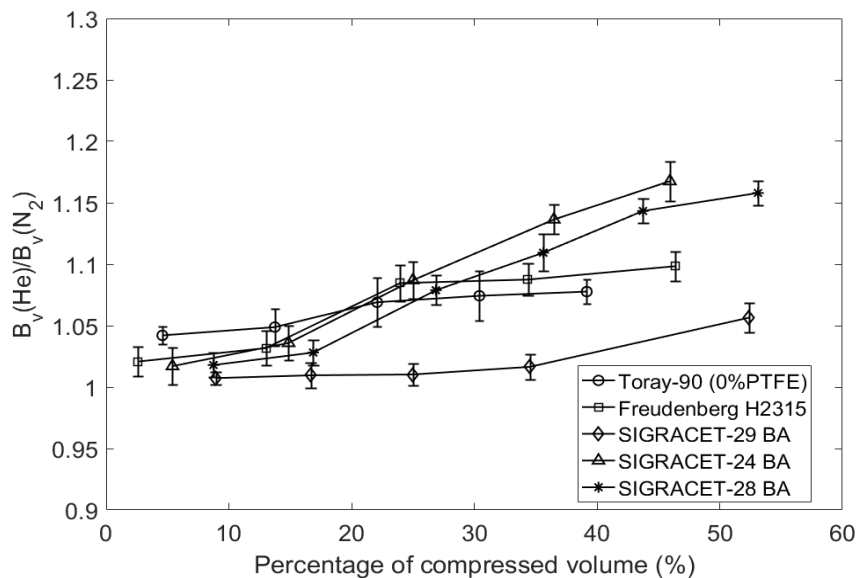


Figure 2.14: Ratio of $B_v(He)$ to $B_v(N_2)$ at varying compression levels for measured GDL samples

2.5.2.5 Comparison of in-plane permeability to theoretical model

As introduced in the literature review, for fibrous porous media, the dependence of permeability on porosity is commonly predicted by the Carman-Kozeny equation [30]:

$$B_v = \frac{\epsilon^3}{16k_K(1-\epsilon)^2} d_f^2 \quad (2.36)$$

where d_f is the fibre diameter measured by SEM images, ϵ is the porosity and k_K is the Kozeny constant. The in-plane permeability results for measured samples were fitted to equation (2.36) to obtain k_K . The measured fibre diameter and value of k_K for the

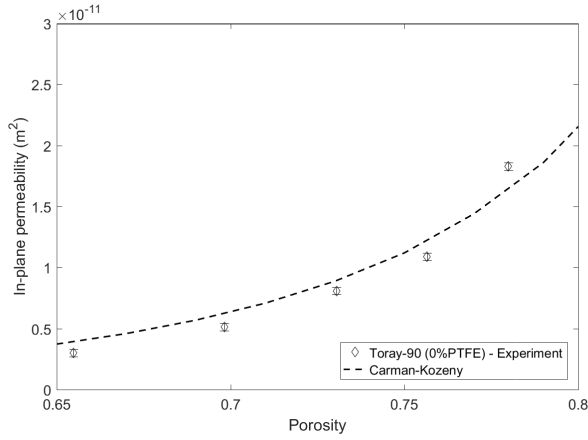
measured GDL samples are shown in Table 2.8. The least-square error is calculated as:

$$Res_{B_v} = \frac{1}{N} \sqrt{\sum_1^N \left(\frac{B_{v,exp} - B_{v,model}}{B_{v,exp}} \right)^2} \quad (2.37)$$

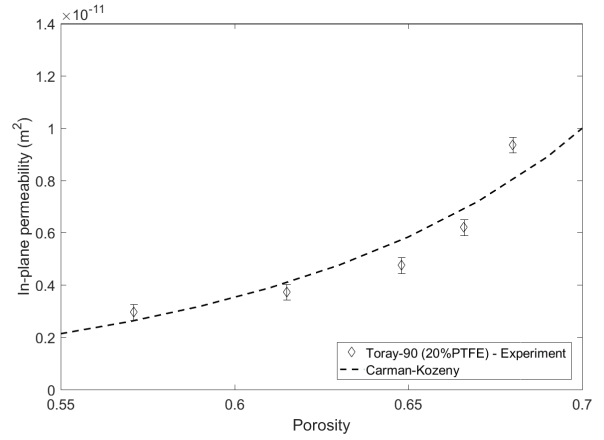
Figure 2.15 shows the Carman-Kozeny prediction and experimental results for all the measured samples. The error for all the measured samples are calculated and shown in Table 2.8. The table illustrates that for BA series GDL, the error increases with increasing volume fraction in matrix. For Toray-90 and Freudenberg H2315 which do not have small pores below 2 μm , the error is much lower than 24 BA and 28 BA but higher than 29 BA. This is mostly because 29 BA has larger maximum pore diameter than Toray-90 and Freudenberg (see PSD curve). Also, the PTFE content does not show an obvious influence on error between experimental permeability and prediction value. It can be concluded that the reliability of Carman-Kozeny correlation is influenced by mainly two factors: (1) the maximum pore diameter, (2) the amount of matrix in GDL, i.e., small-sized pores (less than 2 μm). The discussion above also provides an idea for simulation studies that the morphology of the sample should be fully understood before Carman-Kozeny correlation is used for permeability prediction.

Table 2.8: Volume fraction in carbon matrix vs. least-square error between experimental permeability and Carman-Kozeny equation

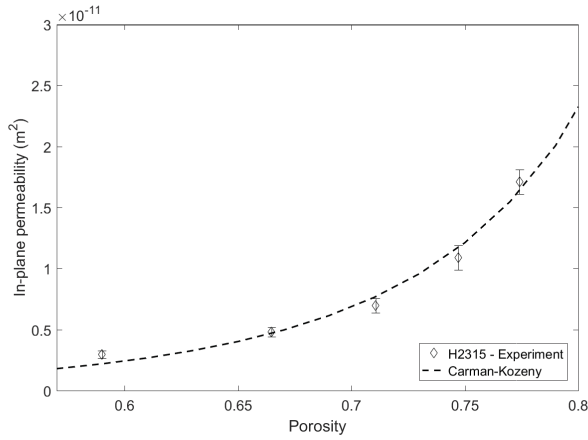
GDL type	Fibre diameter (μm)	k_K	Volume fraction in matrix	Error
Toray-90 (0%PTFE)	7.4 \pm 0.4	2.08	0%	12.9 \pm 3.5%
Toray-90 (20%PTFE)	7.4 \pm 0.4	1.33	0%	13.0 \pm 3.4%
H2315	10.5 \pm 0.2	3.84	0%	11.6 \pm 11.0%
24BA	7.6 \pm 0.3	1.50	26.50%	60.1 \pm 18.8%
28BA	6.5 \pm 0.3	0.74	19.80%	42.7 \pm 16.9%
29BA	8.5 \pm 0.2	2.11	5.34%	5.7 \pm 3.8%



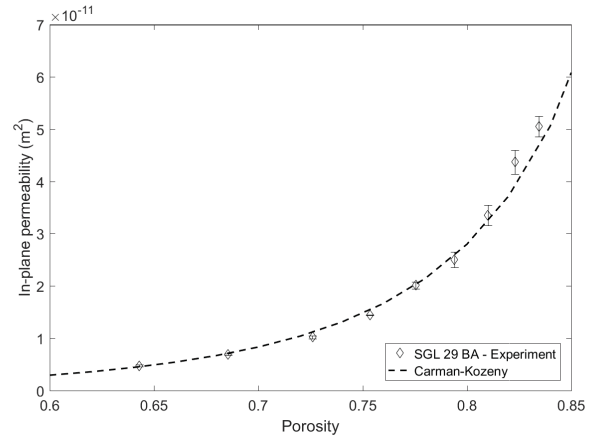
(a) Toray-90 (0%PTFE)



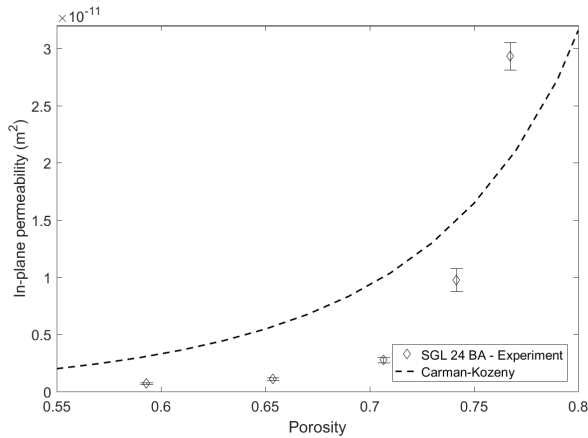
(b) Toray-90 (20%PTFE)



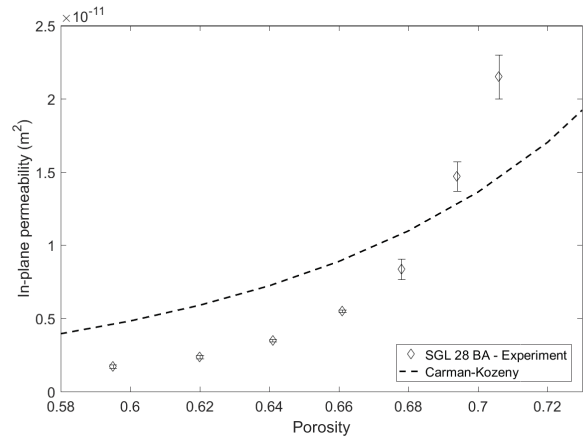
(c) Freudenberg H2315



(d) SIGRACET 29 BA



(e) SIGRACET 24 BA



(f) SIGRACET 28 BA

Figure 2.15: Comparison of experimental permeability to the Carman-Kozeny equation. (a) Toray-90 (0%PTFE), (b) Toray-90 (20%PTFE), (c) Freudenberg H2315, (d) SIGRACET 29 BA, (e) SIGRACET 24 BA, (f) SIGRACET 28 BA

2.5.3 GDL in-plane diffusivity

2.5.3.1 Validation studies: In-plane diffusivity of Toray-90 GDL and comparison with literature

To validate the accuracy of the diffusivity setup, the Toray-90 GDL in-plane diffusivity is measured and the result is compared to literature data. The sample is measured at various thickness in order to estimate the variation of diffusivity with compression. Figure 2.16 shows the in-plane diffusibility at varying porosity where diffusibility is defined as the ratio of effective diffusivity to bulk diffusivity. Three replicates of Toray-90 GDL samples are measured and experimental results show good repeatability. Figure 2.17 shows the experimental results agree with literature results at most of porosities (with 8% error in the gap), except the results reported by Mangal et al. [28]. The value for Mangal et al. under compression might not be accurate due to a defeat on the diffusion bridge leading to uneven compression of the sample. The slight difference between experimental and literature results reported by Rashapov et al. [45] at low compression may be caused by the sample differences and different porosity used in their study.

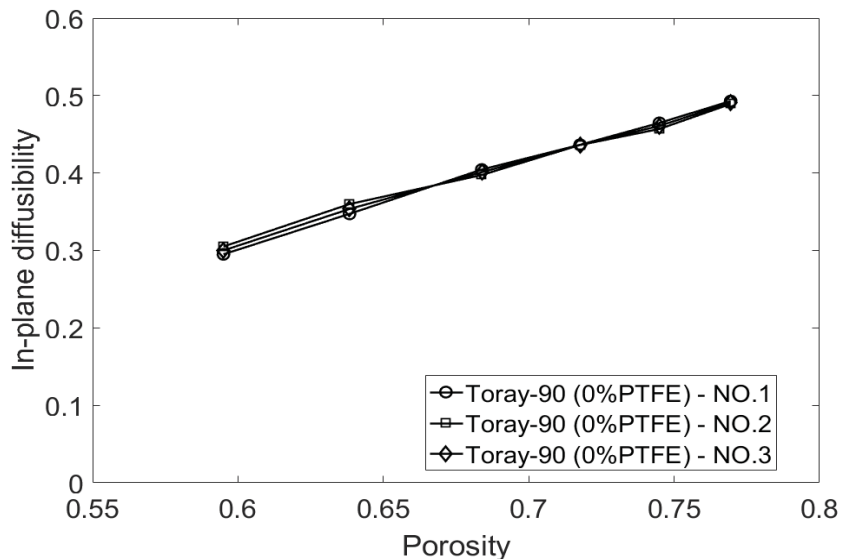


Figure 2.16: Experimental results for Toray-90 (untreated) in-plane diffusibility

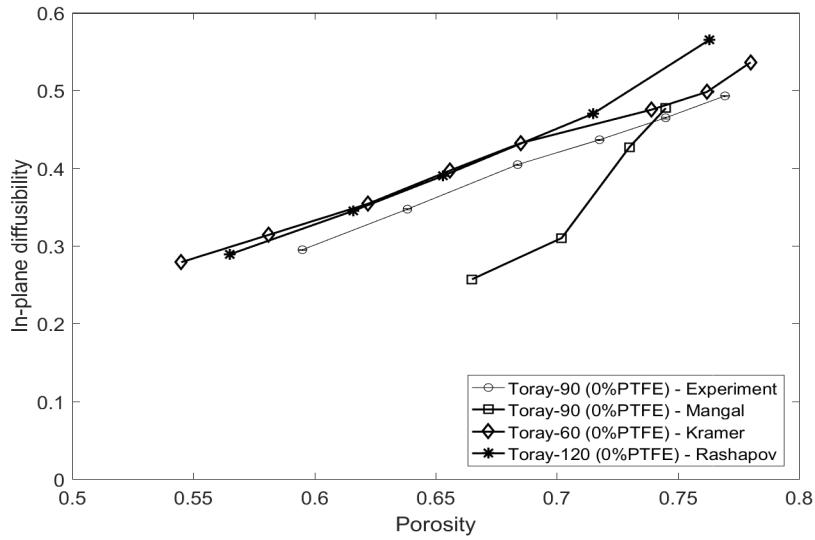


Figure 2.17: Comparison of experimental in-plane diffusibility to literature results (Rashapov [45], Kramer [41], Mangal [28])

The discussion above proves that the experimental setup was working properly and able to reproduce the results in literature.

2.5.3.2 Validation studies: Effect of gas flow rate on in-plane diffusivity

The nitrogen and oxygen flow rates are varied to study the effect of diffusive boundary layers in the channel on diffusivity results. One untreated Toray-90 sample is tested at different porosities at flow rates of 0.2, 0.3, 0.4, 0.5 and 0.6 SLPM. Figure 2.18 shows the in-plane diffusibility at different porosities with different flow rates. It can be found that the diffusibility changed slightly at low flow rates of 0.2 - 0.4 SLPM and remained stable at higher flow rates from 0.4 - 0.6 SLPM. Same trend can also be found for other GDL types. Therefore, the gas flow rate does not affect diffusibility predictions as long as the flow rate is higher than 0.4 SLPM. In this thesis, a 0.5 SLPM was used as default value.

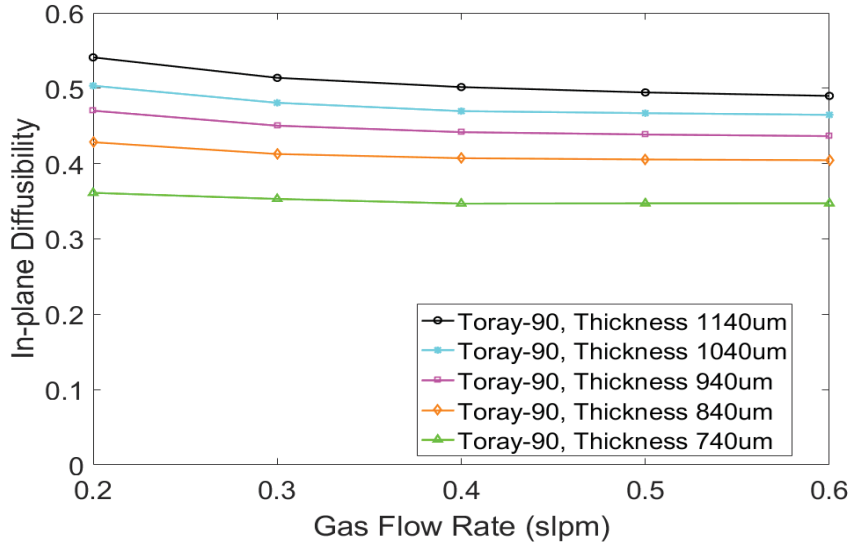


Figure 2.18: Toray-90 (untreated) in-plane diffusibility at different porosities with different flow rates

2.5.3.3 Validation studies: Pressure difference between oxygen and nitrogen channel

The experimental results are obtained based on the assumption that oxygen gas transport through the sample is only by diffusion and therefore convection has a negligible contribution to oxygen transport. In order to validate this assumption, the pressure difference between the two channels is measured during several experiments. The pressure transducer is connected to both nitrogen and oxygen channels while the experiment is being performed. The experiment was performed with 0.5 SLPM and 20 data points were obtained (every 10 seconds). Figure 2.19 shows that the average pressure difference between the two channels is less than 1.2 Pa. The maximum pressure difference is nearly 4 Pa.

The convective molar flux of oxygen through the sample can be calculated using the following equation:

$$\dot{N}_{convection} = \frac{P_{O_2} \dot{V}_p}{RT} = \frac{P_{O_2}}{RT} v A \quad (2.38)$$

where, A is the sample cross-sectional area and \dot{V}_p is the volume convective flux through porous media. Velocity, v , can be obtained using equation Darcy's law. The diffusive molar flux of oxygen through sample can be calculated using equation (2.13). Combining the three

equations, the ratio of diffusive molar flux to convective molar flux can be written as:

$$\frac{\dot{N}_{diffusive}}{\dot{N}_{convective}} = \frac{D_{N_2,O_2}^{eff} \eta}{B_v \Delta P} \quad (2.39)$$

where D_{N_2,O_2}^{eff} and B_v are measured from experiments and ΔP is the pressure difference between channels. Substituting experimental data into equation (2.39) and taking ΔP as 1.2 Pa, a curve of the ratio of diffusion to convection vs. porosity can be obtained as shown in Figure 2.20. In the case of Toray-90 (0%PTFE) and 28 BA, the diffusive flux contribution is more than 10 times higher than convective flux contribution, which proves that the oxygen transport through the sample is diffusion-dominated. If take the maximum value 4 Pa as the ΔP in equation (2.39), the ratio will be approximately 5 - 35 from porosity 0.75 to 0.5. As a result, the average error in diffusibility would be 0.7% - 7% and maximum error would be 2% - 17%.

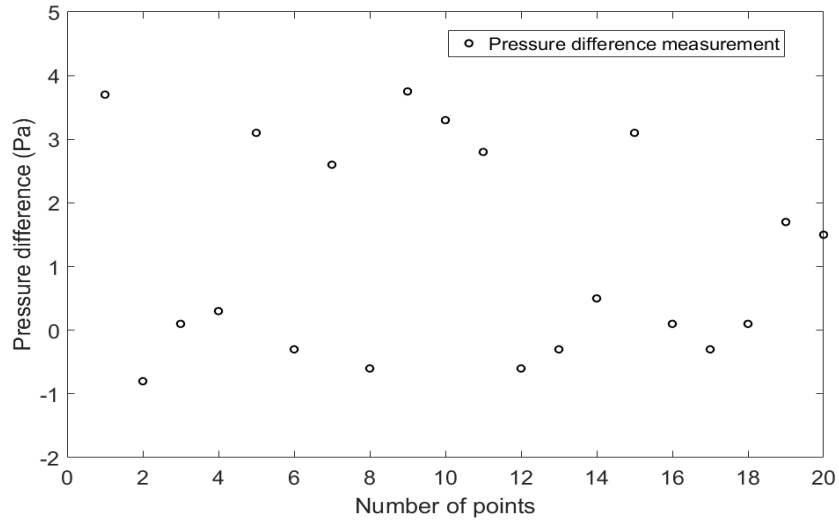


Figure 2.19: Pressure difference between nitrogen and oxygen channel at 0.5 SLPM gas flow rate

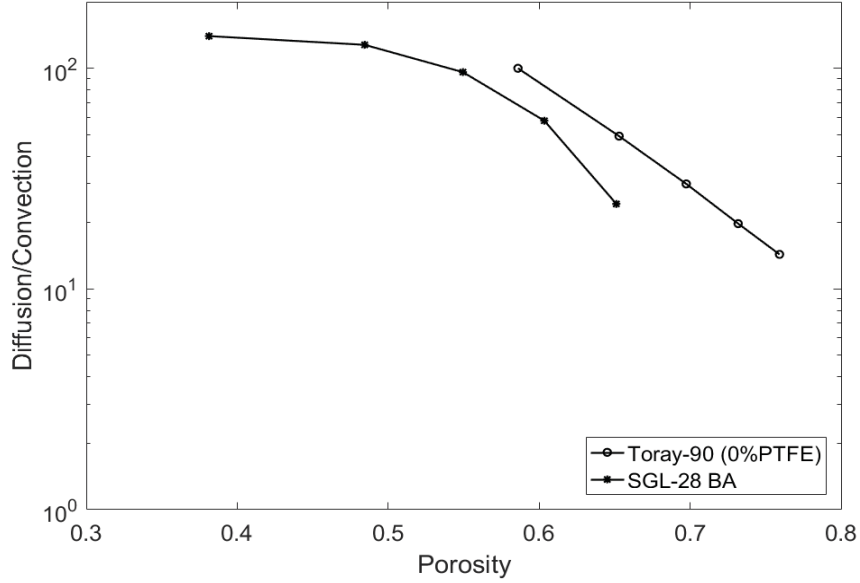


Figure 2.20: Ratio of diffusive to convective flux

2.5.3.4 Validation studies: In-plane diffusivity using different pairs of gases

The GDL diffusibility should not be expected to vary with the pair of working gases because it is a geometric property of the pore structure. Toray-90 (0%PTFE) was tested with two different pairs of gases i.e., $N_2 - O_2$ and $He - O_2$. The bulk diffusion coefficient for $N_2 - O_2$ and $He - O_2$ at atmospheric pressure are 2.2×10^{-5} [65] and $7.4 \times 10^{-5} m^2/s$ [66] respectively. As shown in Figure 2.21(a), the GDL effective diffusivity for $He - O_2$ is 3 to 4 times higher than $N_2 - O_2$ since $He - O_2$ has a higher bulk diffusion coefficient than $N_2 - O_2$. Figure 2.21(b) shows the GDL diffusibility for $He - O_2$ is found to be close to $N_2 - O_2$, which is in accordance with our expectation and indicates that the GDL diffusibility is an intrinsic property that only depends on the pore structure. It can be observed that the diffusibility for $He - O_2$ is slightly higher than $N_2 - O_2$ at high porosity, which is most possibly caused by the smaller diffusive layer in $He - O_2$.

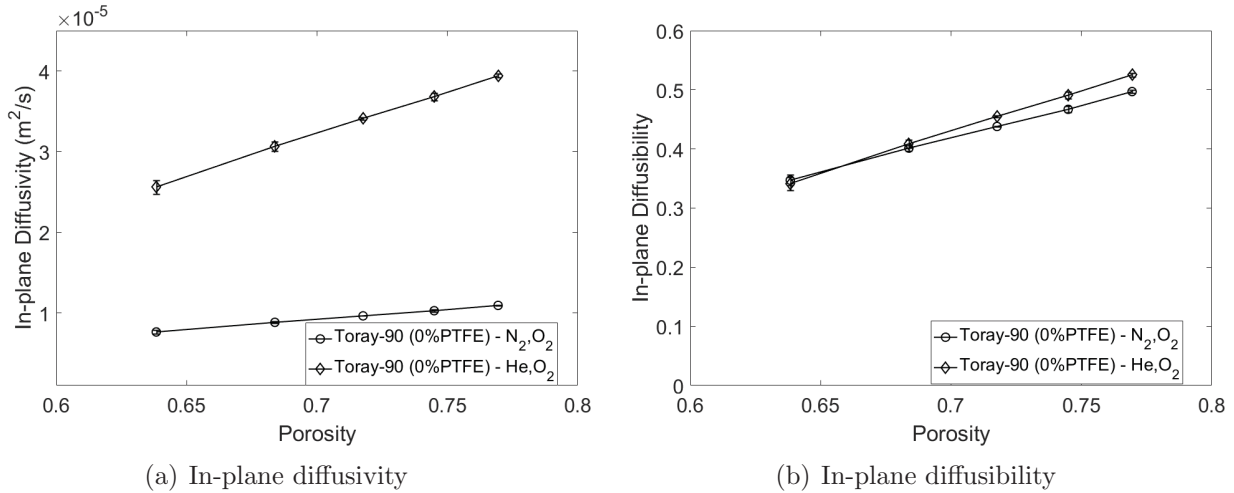


Figure 2.21: In-plane diffusivity and diffusibility of a Toray-90 (0%PTFE) sample

2.5.3.5 In-plane diffusivity of other types of GDL samples

The GDL samples tested in this study include 24 BA, 28 BA, 29 BA, Toray-90 (0%PTFE) and Freudenberg H2315. The reason for choosing different samples is to study the effect of morphology and matrix on in-plane diffusivity. The in-plane diffusibility of all measured samples are shown in Figure 2.22. Compression has a negative influence on the in-plane diffusibility and details will be discussed in the following sections.

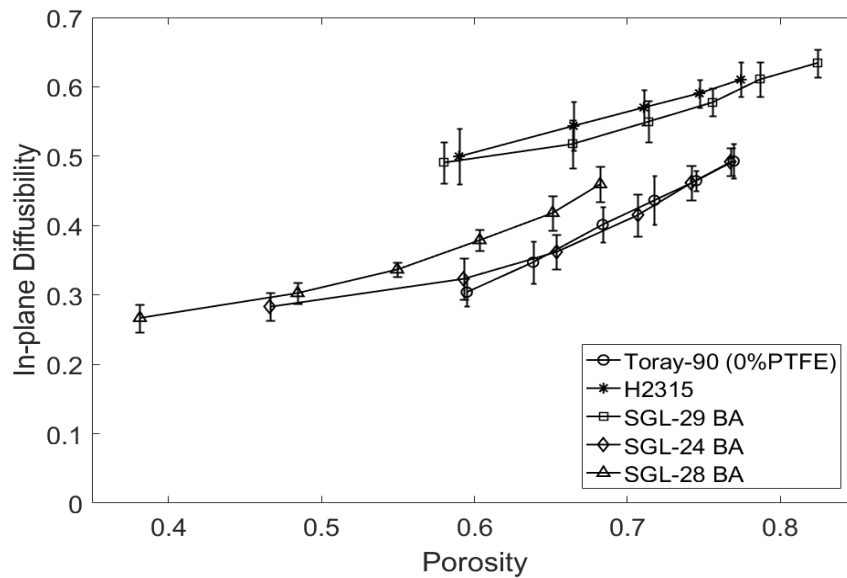


Figure 2.22: In-plane diffusibility of different type of GDL samples

Figure 2.22 shows that at the same porosity, Freudenberg H2315 has a higher diffusibility

than other samples, which is in accordance with the results reported by Rashapov et al. [45]. The reason may lie in the unique morphology of Freudenberg H2315. From Figure 2.8, it can be seen that Freudenberg H2315 shows an entangled fibre structure while other samples show a structure of straight carbon fibres piling up layer by layer. This unique structure of H2315 may be beneficial for the connectivity between pores, as explained by Rashapov et al. [45]. This conclusion can also be proved by the comparison between H2315 and Toray-90 (0%PTFE). From Figure 2.7, it can be seen that H2315 and Toray-90 (0%PTFE) have very similar pore size distribution, as a result, the effect of PSD on diffusibility is minimized. Therefore, the most possible reason for H2315 having a higher diffusibility than Toray-90 (0%PTFE) and other samples lies in the entangled fibre structure in Freudenberg H2315.

SGL-29 BA shows a higher diffusibility than 24 BA and 28 BA at the same porosity because it contains less matrix. 29 BA also shows a higher diffusibility than Toray-90 (0%PTFE) even though it contains more matrix than the latter, which can be explained by its larger maximum pore diameter that has a positive effect on diffusibility.

From this section, it can be concluded that H2315 and 29 BA have higher diffusibility because: (1) H2315 has a entangled fibre structure which is beneficial for pore connectivity, (2) 29 BA has smaller volume fraction in matrix than other BA series GDLs and larger maximum pore diameter.

2.5.3.6 Comparison of in-plane diffusibility to theoretical model

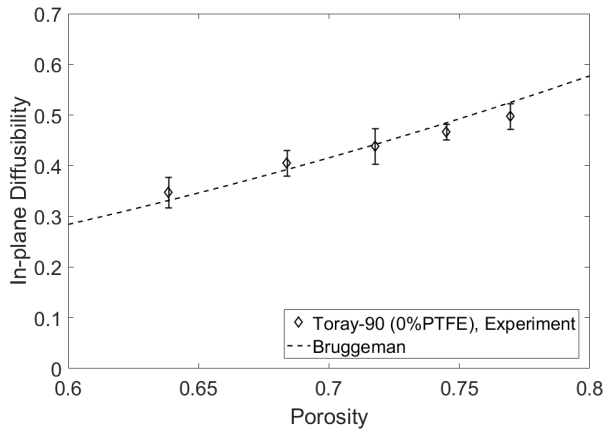
Several commonly used models for estimating the effective diffusion coefficient of porous media have been introduced in the literature review. The models used for comparison with experimental data in this study are shown in Table 2.9, where ϵ is the porosity. The fitting parameters are shown in Table 2.10 and ϵ_{th} was found to be very small for both Tomadakis and Sotirchos (T-S) model and percolation theory. As a result, all the models become exactly the same and provide same estimation for diffusibility. The fitting results using Bruggeman type approximation are shown in Figure 2.23.

Table 2.9: Models used for comparison with experimental data

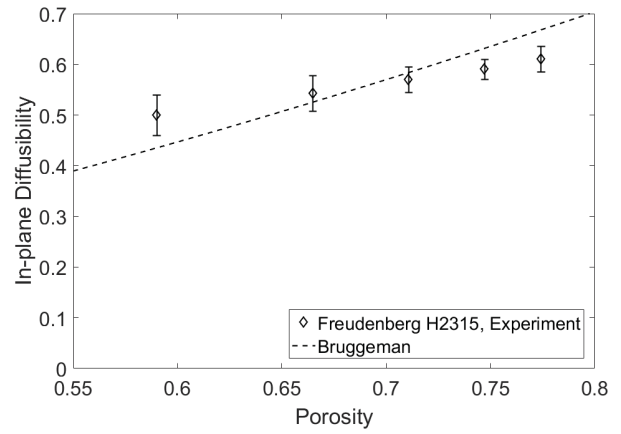
Model	Description
Bruggeman type approximation	ϵ^a
Tomadakis and Sotirchos	$\epsilon \left(\frac{\epsilon - \epsilon_{th}}{1 - \epsilon_{th}} \right)^r$
Percolation theory	$\left(\frac{\epsilon - \epsilon_{th}}{1 - \epsilon_{th}} \right)^\mu$

Table 2.10: Fitting parameters in the model

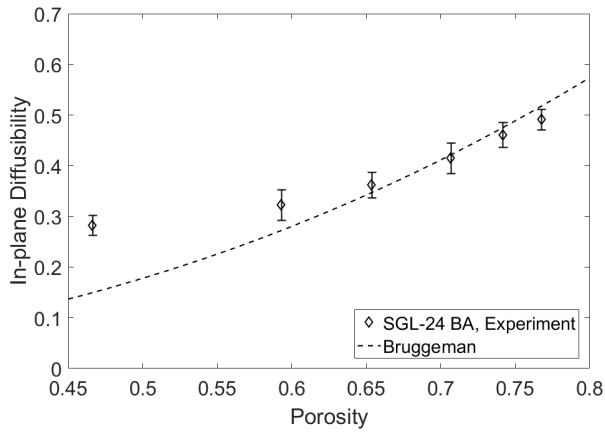
GDL type	a	ϵ_{th}	r	μ
Toray-90(0%PTFE)	2.48	$\ll 10^{-10}$	1.46	2.49
Freudenberg H2315	1.58	$\ll 10^{-10}$	0.58	1.58
24 BA	2.51	$\ll 10^{-10}$	1.49	2.51
28 BA	1.80	$\ll 10^{-10}$	0.79	1.80
29 BA	1.72	$\ll 10^{-10}$	0.72	1.73



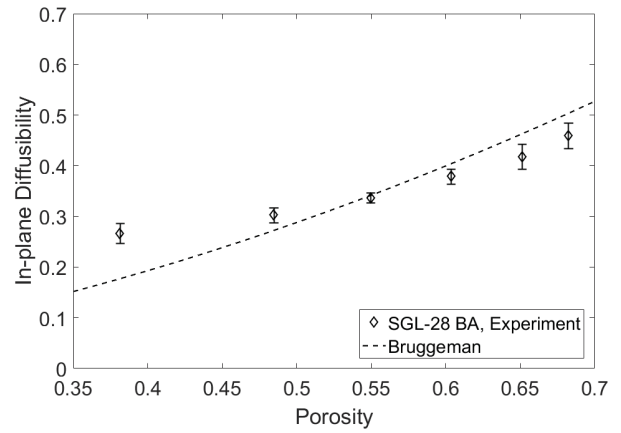
(a) Toray-90 (0%PTFE)



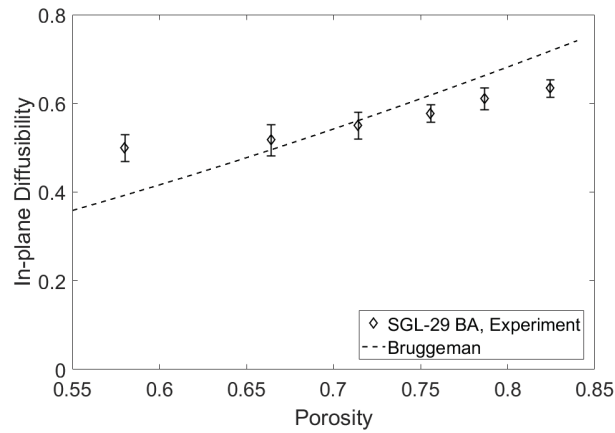
(b) Freudenberg H2315



(c) SIGRACET 24 BA



(d) SIGRACET 28 BA



(e) SIGRACET 29 BA

Figure 2.23: Comparison of experimental in-plane diffusibility to model estimates

The least-square error between experimental diffusibility and prediction is presented in

Table 2.11. Obviously, the error increases with higher carbon matrix and 29 BA has the lowest error among BA series samples. Meanwhile, Toray-90 (0%PTFE) and Freudenberg H2315 show smaller error than BA series GDLs. From Figure 2.23, it can be seen that the error gets bigger at lower porosity, which may be caused by two reasons: (1) The model is developed for random porous structure and it is not appropriate for the tested samples, (2) Knudsen diffusivity might start to play an important role at lower porosity. As shown in Figure 2.14, the ratio of $B_{v,He}/B_{v,N_2}$ is nearly 1.2 at high compression level, which indicates that the Knudsen diffusivity is not small enough to be ignored.

Table 2.11: Volume fraction in carbon matrix vs. least-square error between experimental diffusibility and model

GDL type	Volume fraction in matrix	Error
Toray-90(0%PTFE)	0%	$3.5 \pm 1.6\%$
Freudenberg H2315	0%	$7.1 \pm 4.4\%$
24 BA	26.5%	$12.6 \pm 17.6\%$
28 BA	19.8%	$14.6 \pm 16.4\%$
29 BA	5.3%	$10.0 \pm 8.3\%$

2.6 Conclusions

An in-plane diffusion bridge is proposed to measure the transport properties of GDLs, i.e., in-plane permeability and molecular diffusivity. To validate the setup accuracy, Toray-90 (0%PTFE) is tested and experimental results are used to compare to literature. In order to study the effect of pore size distribution and matrix loading on permeability and diffusivity of GDLs, several GDL types are measured and results are compared with each other.

The GDL permeability is obtained by measuring the pressure drop across the GDL sample and the GDL diffusivity is obtained by measuring oxygen mole fraction in nitrogen channel. The permeability and diffusibility of Toray-90 (0%PTFE) obtained in the experiments were in good agreement with literature. It was found that the pore size distribution and carbon matrix had a significant effect on permeability. Knudsen slip is more significant for those GDL samples containing a high matrix loading, such as 24 BA and 28 BA. In contrast, the samples with less carbon matrix, such as Freudenberg H2315 and SGL-29 BA, exhibited less Knudsen slip effect. In addition, the error between experimental permeability and Carman-Kozeny model increases with higher volume fraction in carbon matrix.

In terms of diffusivity, SGL-29 BA and Freudenberg H2315 show the highest diffusibility

at same porosity or compression level, which is attributed to less carbon matrix and large pore diameter. The error between experimental diffusibility and model can be significant at low porosity or high compression level. As a result, Knudsen diffusivity might need to be considered at high compression level and its effect on GDL diffusivity needs to be further studied by compressing the sample into lower thickness.

Chapter 3

Measurement of through-plane PEM fuel cell catalyst layer gas transport properties

3.1 Introduction

In this chapter, the experimental technique utilized for the purpose of measuring the through-plane gas transport properties of GDLs and CLs is described. Prior to the CL measurements, Toray-90 GDL samples measurements are discussed in order to compare experimental results to literature data to validate the accuracy of the setup. The setup was originally presented by Pant et al. [26] and extensively modified by Mangal et al. [29] by introducing a different set of pressure sensors, pressure controllers, and oxygen sensors, however CL permeability and diffusivity measurements have not previously been reported using this setup. Further, permeability results for a CL have seldom been reported in literature. Zhao et al. [48] measured CL permeability but Knudsen diffusivity was ignored.

Section 3.2 discusses the experimental setup for the through-plane permeability and effective molecular diffusivity as well as the catalyst layer characterization. Section 3.3 describes the theory and mathematical models for estimating the gas transport properties. Section 3.4 discusses measurement uncertainty for through-plane permeability and diffusivity of GDL and CL. In Section 3.5, the experimental results of Toray-90 GDL samples are compared with literature to validate measurement reliability. CL permeability and diffusivity results are presented next.

3.2 Experimental setup

3.2.1 Through-plane diffusion bridge

The diffusion bridge is made up of two acrylic plates with flow channels machined into them. Figure 3.1 shows the photograph of one acrylic plate. The cross-sectional area of the channel is $15 \times 2 \text{ mm}^2$ and the length is 15 cm. The channel length is selected to ensure that the gas flow field is fully developed before it reaches the sample [27].



Figure 3.1: Photograph of one acrylic plate

3.2.2 Sample preparation

GDL preparation - For the purpose of testing GDLs, samples are cut into $1.1 \times 2 \text{ cm}^2$ using a precision knife. Three layers of sample are then stacked together to form the specimen to test. The reason for using multiple layers is two fold [26]: (a) to have sufficient pressure drop across the porous media, and (b) to ensure that a representative elementary volume of GDL exists [67]. A 3 mil lamination sheet with a hole of diameter 8 mm punched in the center to allow the gas to flow through the sample in the through-plane direction was used as a lamination sheet. The sample was introduced between lamination sheets at the location of the hole and the sample was then laminated (HeatSeal H220 laminator) between the two sheets where the hole was located. Examples of prepared samples are shown in Figure 3.2. The thickness of the sample was measured before and after lamination and the amount of compression was calculated to be less than 1% of the thickness of the uncompressed sample. As a result, its effect on the porosity was ignored. Unless otherwise stated, 3 layers of GDL samples are stacked together for testing. The hole diameter for gas transport is fixed as 8 mm.



Figure 3.2: Prepared GDL samples

Catalyst layer fabrication and preparation - An inkjet printer (Dimatix 2831) is used to fabricate the CLs. Compared to traditional catalyst fabrication method, such as ultrasonic spray, inkjet printing has advantages of high precision and reduced catalyst waste [68].

Catalyst inks were first prepared by mixing 37.5 mg of platinum supported on carbon black (Alfa Aesar Vulcan 20%Pt/C and 40%Pt/C or TTK Ketjen 46.7% Pt/C) with a mixture of isopropanol (IPA) and propylene glycol (PG) as solvent. The mixture was bath sonicated for 30 minutes and then the desired amount of 5 wt% of Nafion ionomer solution (Ion Power, LQ-1105 1100EW) was added drop-wise during sonication. The ink was then probe sonicated (S-4000, Q-Sonica) to further help in breaking any catalyst particle aggregates for 15 minutes (Amplitude 20, 2 minutes on, 1 minute off). Further details on the preparation method can also be found in Ref. [69].

To measure the permeability and diffusivity of CL, each CL sample needs to be deposited on a substrate. An ideal substrate should fulfil the following functional requirements: (1) small pore diameters such that the catalyst inks would not penetrate into the substrate during printing, and (2) considerably similar or higher permeability and diffusivity than that of the CL such that the pressure drop or diffusion resistance that arises from the CL can be easily detected. We found that a PTFE filter satisfied both requirements. The filter is hydrophobic and inert to most chemically aggressive solvents, has a small pore diameter,

i.e., $0.1\ \mu\text{m}$, and relatively high porosity, i.e., 68%.

A Fujifilm Dimatix 2831 inkjet printer was used to print the CL on the PTFE filter. The ink was intruded in a cartridge that has 16 square nozzles in order to deposit the ink drop-by-drop. The printer and cartridge are shown in Figure 3.3. $1.3\times 1.3\ \text{cm}^2$ CLs were printed directly on the PTFE filter that was fixed to an aluminium foil piece (see Figure 3.4) and the loading was controlled by the number of layers printed on the filter. The total weight of the catalyst was measured by an electronic balance with accuracy of 0.1 mg. To avoid compressing the CL/filter sample, the sample is placed between two transparent tapes with a hole of diameter 8 mm in the center. Figure 3.5 shows the schematic of CL sample assembly.



Figure 3.3: Images of: (a) Dimatix 2831 inkjet printer, (b) Printer cartridge



Figure 3.4: Pictures of: (a) PTFE filter fixed on aluminum foil, (b) Catalyst printed on PTFE filter

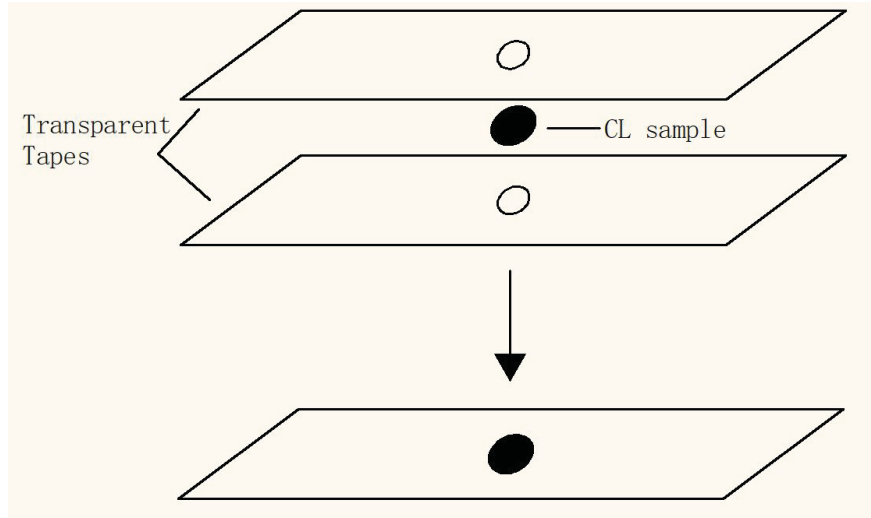


Figure 3.5: CL sample assembly

The prepared GDL or CL/filter samples were placed between the top and bottom plates. A 10 mil silicon gasket was placed between lamination sheet and plate to prevent any leakage. The bolts were then tightened using a torque value of 4 N-m (4 inch-lb) in a cross cyclic manner to create a uniform compression. The whole assembly is shown in Figure 3.6. To detect leakage, the bridge was filled with nitrogen, pressurized up to 50 psig, and placed in water. No bubbles were visible leaving the diffusion bridge, which proved that there was no leakage.



Figure 3.6: Through-plane diffusion bridge assembly

3.2.3 Through-plane permeability and Knudsen diffusivity setup

The through-plane diffusion bridge has two channels with each channel having five ports. In the permeability experiment, one port is connected to the bottle via a mass flow controller (MFC) and another port is connected to a pressure transducer (PT). The other three ports of the channel are closed so that the gas is forced to flow from one channel to the other through the porous media in the through-plane direction. One port of the low-pressure channel is then connected to the low-pressure port of the PT and the other ports are open to the atmosphere. A schematic diagram of the setup is shown in Figure 3.7.

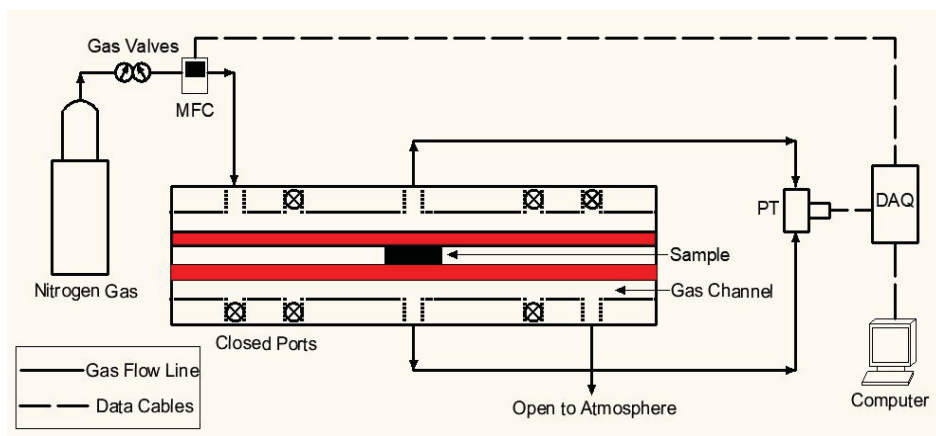


Figure 3.7: Experimental setup for through-plane permeability

Compressed nitrogen (PRAXAIR, UHP 5.0) from a gas cylinder at 50 psig flows to the mass flow controller (Cole-Parmer, Serial Number: 62704, range: 0-5 SLPM) which is used to control the gas flow rate. A pressure transducer (OMEGA, Serial Number: 422542, range: 0-70 mbar; OMEGA, Serial Number: 418617, range: 0-3.5 bar) is connected to both channels so that the pressure drop across the porous media at different flow rates can be measured. The MFC is connected to a computer via an RS-232 communication port. A data acquisition card (National Instruments USB 6221) is used to read data from the PT and MFC. LabWindows/CVI is used to communicate with the setup and log data from the MFC and PT into a text file. The data is logged for 125 seconds (25 readings) for each flow rate to ensure steady state.

The average pore size in the CL is much smaller than that in the GDL and it is comparable to the gas mean free path. As a result, the Knudsen slip effect can be significant in CLs [26]. To measure the through-plane permeability and Knudsen diffusivity of CL samples, the permeability experiments are performed with gases with varying mean free path, i.e., nitrogen and helium. Even though the permeability is an intrinsic property that only

depends on the pore structure, the permeability results are different for nitrogen and helium because of the influence of Knudsen slip. The Knudsen diffusivity can be estimated based on the difference in the permeability between nitrogen and helium and it will be discussed in the theory section.

3.2.4 Through-plane diffusivity setup

GDL diffusivity measurement - In the through-plane diffusivity experiment, nitrogen and oxygen gases are input into each one of the channels. The two compressed gases are adjusted to 50 psi before flowing through the MFCs. Nitrogen (Cole-Parmer, Serial Number: 62704, range: 0-5 SLPM) and oxygen mass flow controllers (Cole-Parmer, Serial Number: 62661, range: 0-5 SLPM) are used to control the flow rate of the gases.

A back pressure controller (Cole-Parmer, Serial Number: 84800, range: 0 - 100 psi) is connected to the outlet of the nitrogen channel and used to maintain the system pressure at a stable value. A differential pressure controller (Cole-Parmer, Serial Number: 84801, range: 0 - 500 pascals) is connected to the outlet of the oxygen channel and used to control the static pressure difference between the two channels using a differential pressure gauge. The oxygen pressure is set to be higher than nitrogen in order to enhance oxygen mass transport through the porous media via convection. A diagram of the setup is shown in Figure 3.8.

To measure the oxygen mole fraction in the gas mixture at the outlet of the nitrogen channel, a NEOFOX oxygen sensor (Ocean Optics, Model: FOSPOR-600-32MM, range: 0 - 21% in gas) is used. To achieve accurate measurements, the oxygen sensor is recalibrated every day before running the experiment. Two mass flow controllers are used to create a gas mixture of known oxygen levels, and the results are compared to the measured oxygen levels by the NEOFOX sensor in order to calibrate the sensor by changing oxygen levels. Calibrated compressed nitrogen-oxygen gas mixtures (PRAXAIR, Accuracy: $\pm 2\%$ Rel) containing 1% and 10% oxygen respectively are finally used to validate the calibration results. The sensor is considered to be properly calibrated when for the two gas mixture, the measurement results are $1\% \pm 0.02\%$ and $10\% \pm 0.1\%$, respectively. The calibration file is uploaded in the NEOFOX software, and the calibration is done.

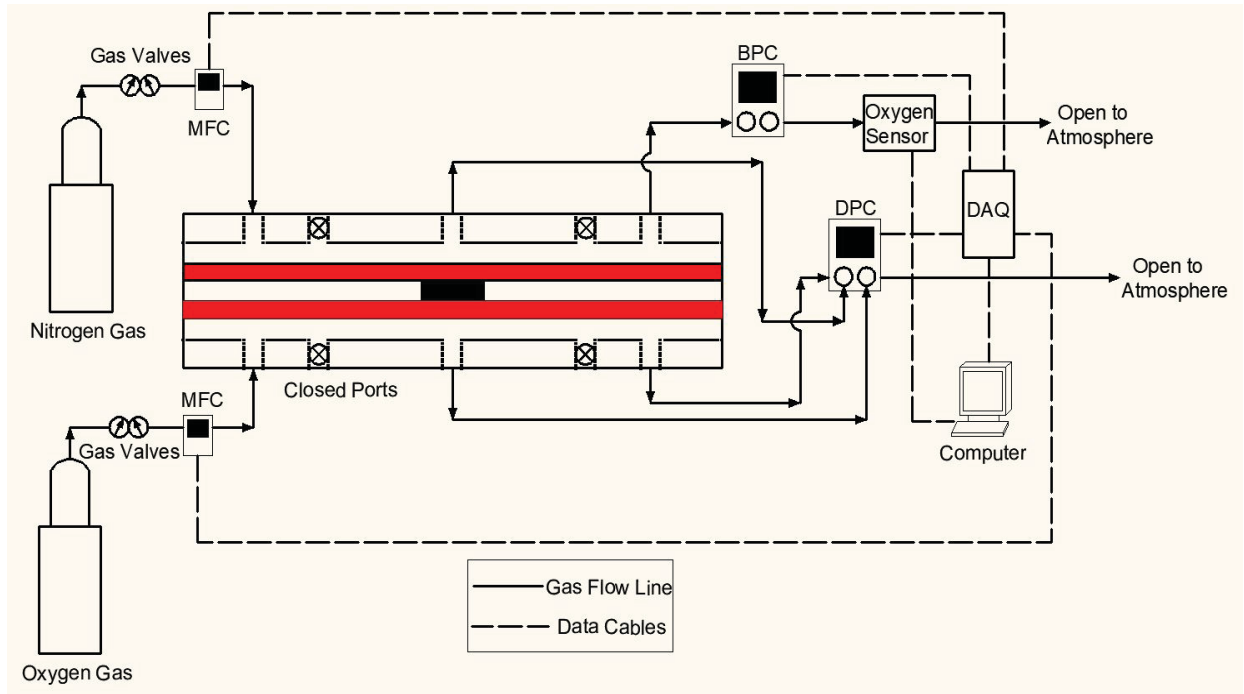


Figure 3.8: Experimental setup for through-plane diffusivity

The MFC, DPC and BPC are connected to a computer via an RS-232 communication port. A data acquisition card is used to read data from the pressure transducer. LabWindows/CVI is used to log data and store the data in a text file. The data is logged every 5 seconds for 5 minutes. The NEOFOX software logs data from the oxygen sensor and stores oxygen volume fraction vs. time in a CVS file every 5 seconds for 5 minutes. The real time is also recorded by both LabWindows/CVI and NEOFOX software and it is used to correlate oxygen volume fraction to its corresponding differential pressure. The data in the text and CVS file are merged manually and used for data processing. Figure 3.9 shows the photograph of the setup.

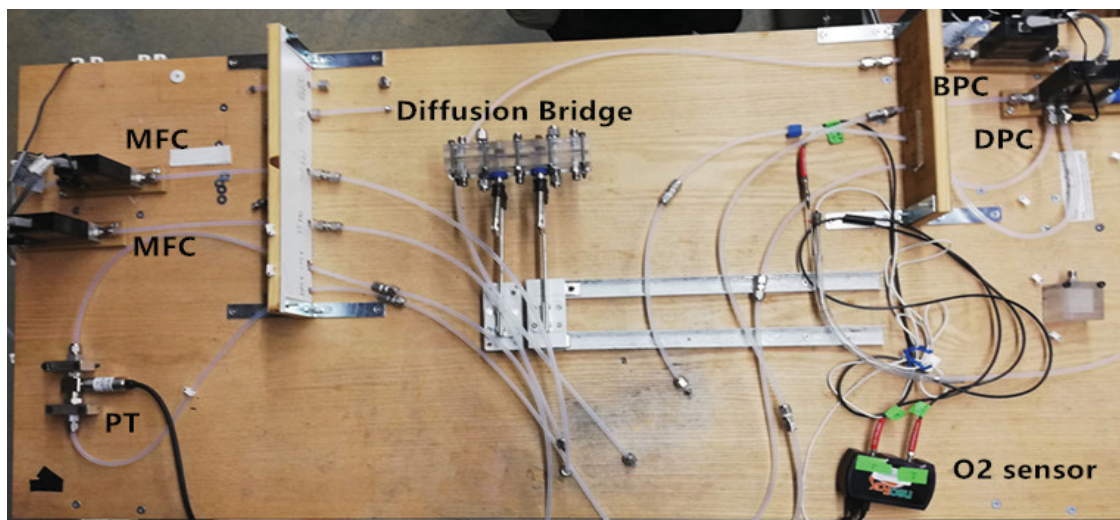


Figure 3.9: Photograph of the through-plane setup (Data acquisition card is not shown in this picture)

CL diffusivity measurement - To measure the through-plane diffusivity of CLs, nitrogen and oxygen gases are input into each one of the channels. The two compressed gases are adjusted to 50 psi before flowing through the MFCs. Nitrogen and oxygen MFCs (Cole-Parmer, Serial Number: 62704, range: 0-5 SLPM; Serial Number: 62661, range: 0-5 SLPM respectively) are used to control the flow rate of the gases. The oxygen channel outlet is open to ambient and nitrogen channel outlet is connected to the oxygen sensor.

The BPC and DPC were not used in the CL through-plane diffusivity measurements because of the following: (1) Removing the DPC and BPC simplifies the setup and reduces the uncertainty arising from the controllers; and, (2) The permeability of CL is low enough that oxygen transport through the CL by convection is negligible. Figure 3.10 shows differential pressure and oxygen mole fraction measurements of a CL sample. The oxygen mole fraction decreases from around 5.17% to 5.15% with differential pressures of 100 to 20 Pa. This difference is within the calibration error of the sensor and results in a difference of the predicted diffusivity of 0.05%. As a result, the pressure difference was not found to affect the oxygen diffusion results. A schematic diagram of the setup is shown in Figure 3.11.

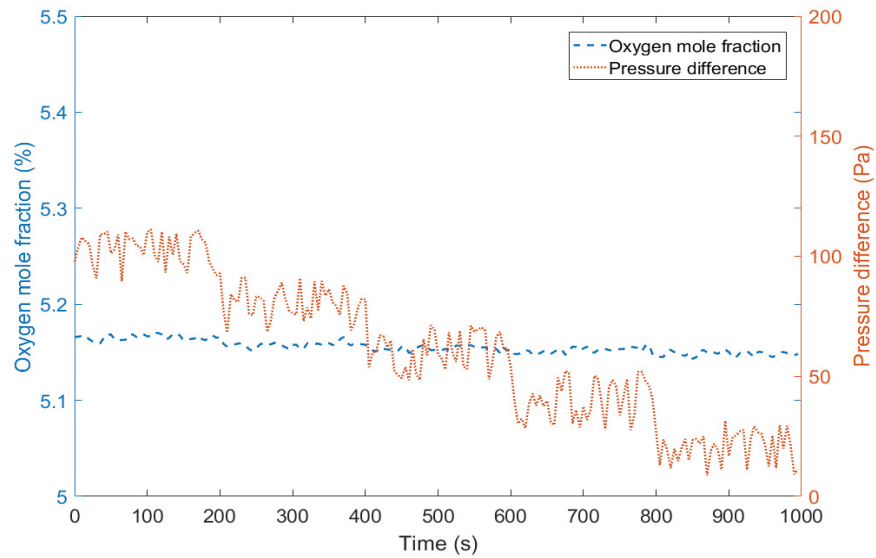


Figure 3.10: Pressure difference and oxygen concentration readings for a CL sample

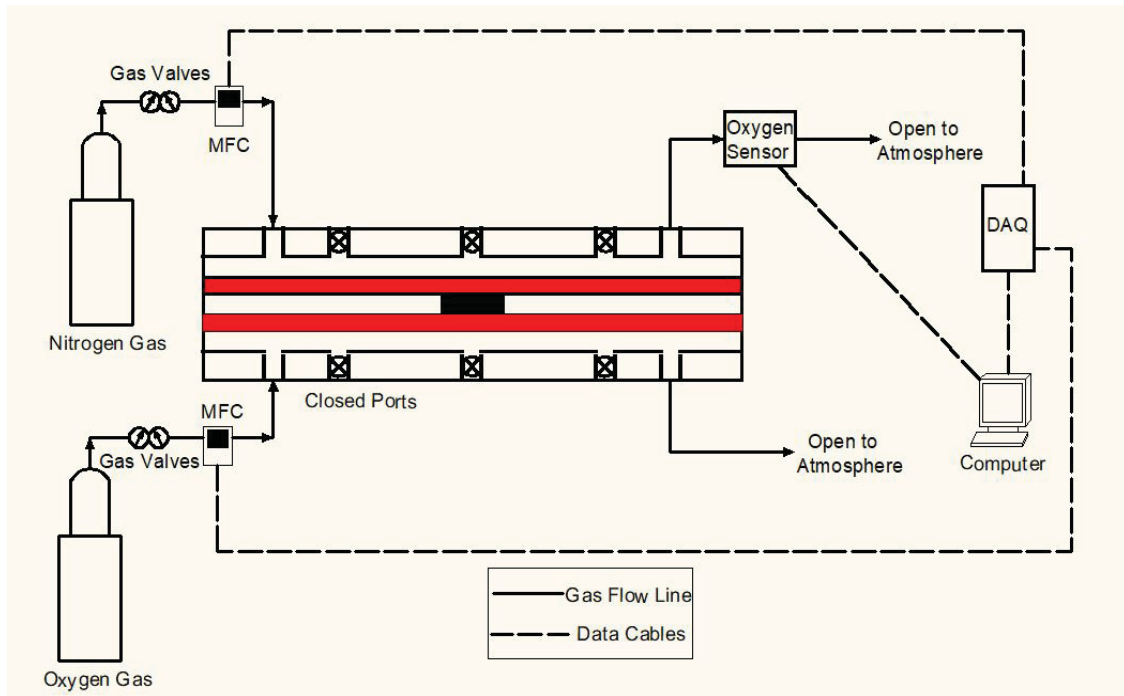


Figure 3.11: Experimental setup for CL through-plane diffusivity measurement

To measure the oxygen mole fraction in the gas mixture at the outlet of the nitrogen channel, a NEOFOX oxygen sensor (Ocean Optics, Model: FOSPOR-600-32MM, range: 0 - 21% in gas) is used. The detailed information of the sensor has been discussed before.

The MFC is connected to a computer via an RS-232 communication port. A data acquisition card is used to read data from the pressure transducer. LabWindows/CVI is used to communicate with the MFC. The NEOFOX software logs data from the oxygen sensor and stores oxygen volume fraction vs. time in a CVS file every 5 seconds for 5 minutes after oxygen concentration is stabilized. Then, the flow rate of the gas and average oxygen concentration are used to estimate the oxygen flow rate through the CL and details will be discussed in section 3.3

3.2.5 Experimental conditions

To measure the through-plane permeability of GDLs, the mass flow rate of nitrogen is varied from 0 to 1 standard liters per minute (SLPM) in 10 even intervals. For measuring the permeability and Knudsen diffusivity of the CL sample, the mass flow rate varies from 0 to 0.1 SLPM in 10 even intervals. Low flow rates are used in CL measurements to minimize any inertial effect. The experiment is run at zero flow rate to estimate the offset of the PT.

For measuring the through-plane diffusivity of the GDL, the mass flow rate of both gases is set to 1 SLPM. The reason for using high mass flow rate is two fold: (1) to make sure that the oxygen that flows to the nitrogen channel is swept away very quickly and the effect of the diffusive boundary layer is minimized; and, (2) to make sure that the oxygen volume fraction falls in a reasonable range, i.e., 1%-5%. The back pressure of the system is maintained at 10 psig pressure unless otherwise stated. The pressure difference between the two channels is varied from 2-10 Pa in 5 intervals.

For measuring the CL through-plane diffusivity, the mass flow rate of both gases are set to 0.5 SLPM. Different flow rates were also used for validation and it was found that the through-plane diffusivity is nearly independent on the flow rate, within an error 1.3% - 4.5%.

Permeability and diffusivity experiments are performed three times using three different samples. For each sample, the permeability and diffusibility are measured three times without opening/closing the diffusion bridge. An analysis of the experimental error from various sources is provided in section 3.4.

3.2.6 Catalyst layer characterization

To get permeability and diffusivity of the CLs, it is necessary to measure the CL thickness. Two approaches were employed to measure the CL thickness and the results were compared

with each other. The first approach was simple and fast: the catalyst was printed on a piece of aluminium foil first and the thickness was obtained by measuring the thickness of aluminium foil before and after printing. A micrometer (Mitutoyo Japan, Series NO.:008395) with an accuracy of $2\ \mu\text{m}$ was used for the measurement.

To validate the first method, SEM imaging was used to measure the thickness. Samples were placed in epoxy (see Figure 3.12) and taken to the SEM for imaging. Figure 3.13 shows the SEM images for different CLs (taken by Manas Mandal, a PhD student in my research group). The position of CL and PTFE filter are marked in the picture. The bright area is caused by sample charging. The thickness was measured at ten different locations. The measured thicknesses are shown in Table 3.1. The thicknesses measured by micrometer and SEM imaging are in good agreement and, due to the higher accuracy, SEM thickness is used as CL thickness. In addition, surface images were also taken using a stereoscopic optical microscope (Leica MC170 HD), shown in Figure 3.14, and no obvious macro-cracks were found. The white spots are considered to be contaminants or dusts.



Figure 3.12: Catalyst layer placed in epoxy

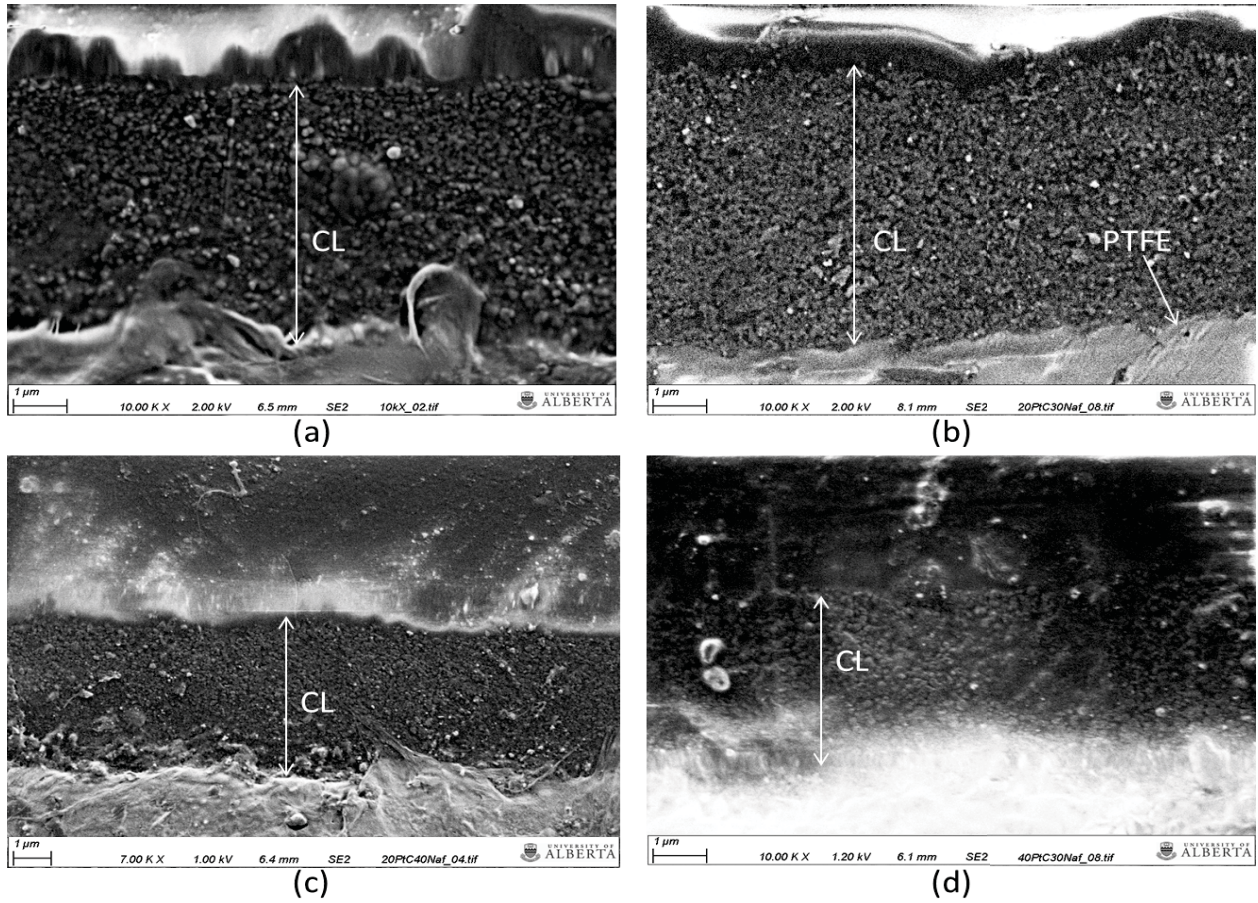
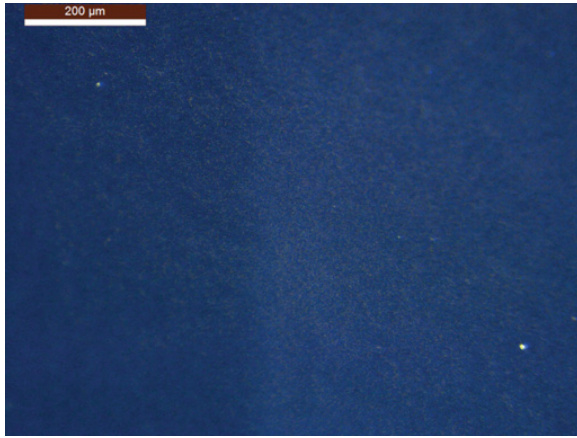


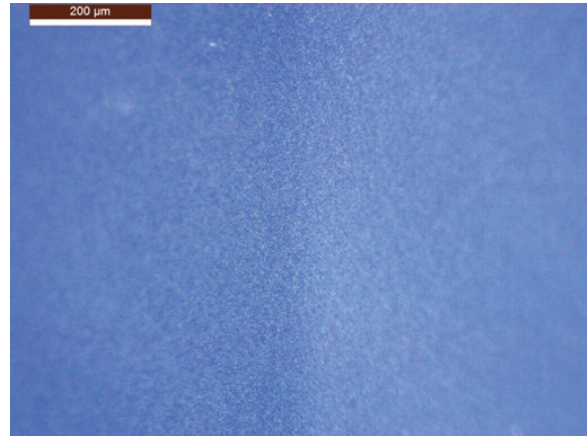
Figure 3.13: Catalyst layer SEM images deposited on PTFE filter: (a) 20%Pt/C, 20%Nafion, (b) 20%Pt/C, 30%Nafion, (c) 20%Pt/C, 40%Nafion, (d) 40%Pt/C, 30%Nafion

Table 3.1: Properties of catalyst: Pt/C ratio, Nafion loading, number of layers, thickness measured by Micrometer and SEM

Carbon support	Nafion loading	Pt loading	#of layers	Micrometer	SEM
Vulcan 20%Pt/C	20%	0.123 mg/cm ²	15	6.0±0.5μm	5.8±0.4 μm
Vulcan 20%Pt/C	30%	0.124 mg/cm ²	15	6.1±0.6μm	5.5±0.3 μm
Vulcan 20%Pt/C	40%	0.085 mg/cm ²	15	3.5±0.5μm	3.9±0.3 μm
Vulcan 40%Pt/C	30%	0.215 mg/cm ²	15	4.0±0.5μm	3.9±0.3 μm
Ketjen 46.7%Pt/C	30%	0.251 mg/cm ²	15	5.5±0.5μm	5.5±0.4μm



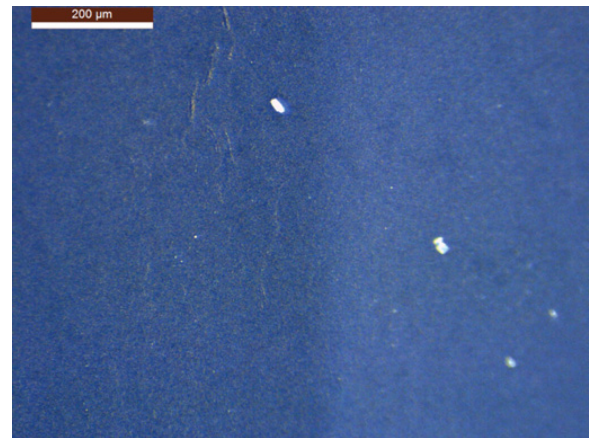
(a) 20%Pt/C, 20%Nafion



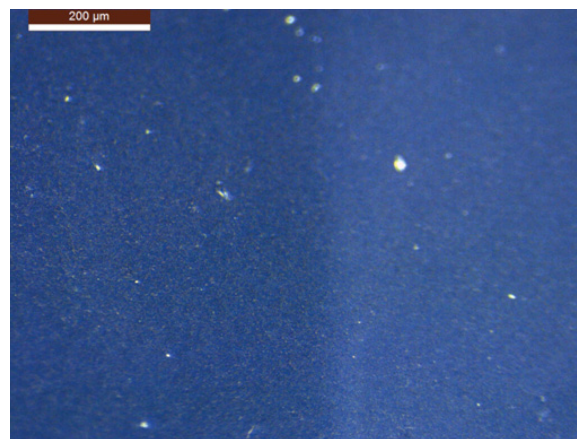
(b) 20%Pt/C, 30%Nafion



(c) 20%Pt/C, 40%Nafion



(d) 40%Pt/C, 30%Nafion



(e) 46.7%Pt/C, 30%Nafion

Figure 3.14: Surface images of catalyst layers: (a) 20%Pt/C, 20%Nafion, (b) 20%Pt/C, 30%Nafion, (c) 20%Pt/C, 40%Nafion, (d)40%Pt/C, 30%Nafion, (e) 46.7%Pt/C, 30%Nafion

CL Porosity was calculated using following process. First, the total weight of the catalyst

sample was measured which can be expressed as:

$$m_T = m_{Pt} + m_{carbon} + m_{Nafion} \quad (3.1)$$

where m_{Pt} , m_{carbon} and m_{Nafion} are the weight of Pt, carbon black and Nafion respectively. The volume of Nafion can be calculated as:

$$V_{Nafion} = \frac{m_{Nafion}}{\rho_{Nafion}} = \frac{m_T \text{wt}\%_{Nafion}}{\rho_{Nafion}} \quad (3.2)$$

where $\text{wt}\%_{Nafion}$ is the weight percentage of Nafion in the inks and ρ_{Nafion} is the density of Nafion which is taken as 2 g/cm³ [70]. The percent of Pt in Pt/C powder, $\text{wt}\%_{Pt/C}$ is expressed as:

$$\text{wt}\%_{Pt/C} = \frac{m_{Pt}}{m_{Pt} + m_{carbon}} = \frac{m_{Pt}}{m_s} \quad (3.3)$$

then, solid volume, V_s , in the catalyst can be written as:

$$V_s = V_{Pt} + V_{carbon} = \frac{m_{Pt}}{\rho_{Pt}} + \frac{m_{carbon}}{\rho_{carbon}} = \frac{\text{wt}\%_{Pt/C} m_s}{\rho_{Pt}} + \frac{(1 - \text{wt}\%_{Pt/C}) m_s}{\rho_{carbon}} \quad (3.4)$$

where ρ_{Pt} is the density of platinum and ρ_{carbon} is the density of carbon. Equation (3.4) can also be rearranged such that:

$$V_s = (1 - \text{wt}\%_{Nafion}) m_T \left(\frac{\text{wt}\%_{Pt/C}}{\rho_{Pt}} + \frac{1 - \text{wt}\%_{Pt/C}}{\rho_{carbon}} \right) \quad (3.5)$$

Finally, porosity of CL can be calculated as:

$$\epsilon_{CL} = \frac{V_{bulk} - V_s - V_{Nafion}}{V_{bulk}} \quad (3.6)$$

where, V_{bulk} , the total volume, is equal to the product of the CL thickness and area of the sample which is measured directly. The total weight, m_T is measured by an electronic balance (Sartorius ENTRIS124I-1S, accuracy 0.1 mg). The porosities calculated using equation (3.6) are shown in Table 3.2. Here, ρ_{carbon} , ρ_{Pt} and ρ_{Nafion} are taken as 2 g/cm³, 21.5 g/cm³ [71] and 2 g/cm³ [70], respectively. Ionomer-carbon (I/C) ratio, is calculated and shown in Table 3.2 as well as porosity. The experimental porosity is compared to literature data from Ref. [36, 46, 69, 72] in Figure 3.15. It can be seen that experimental porosity is in agreement with literature data from Ref. [69, 72] since same fabrication method is used in the studies. However, CLs fabricated using other methods show higher porosities [36, 46]. Also, the experimental data and Ref. [69, 72] show that CLs using Ketjen black as a support have

a higher porosity than CL using Vulcan support for the same I/C ratio, which is because Ketjen carbon black is more porous than Vulcan carbon black.

Table 3.2: Porosity and I/C ratio of measured CLs

CL components	Total weight	Porosity	I/C
Vulcan 20%Pt/C, 20%Naf	1.3 mg	42.98%	0.31
Vulcan 20%Pt/C, 30%Naf	1.5 mg	31%	0.54
Vulcan 20%Pt/C, 40%Naf	1.2 mg	20.01%	0.83
Vulcan 40%Pt/C, 30%Naf	1.3 mg	26.84%	0.71
Ketjen 46.7%Pt/C, 30%Naf	1.3 mg	50.88%	0.80

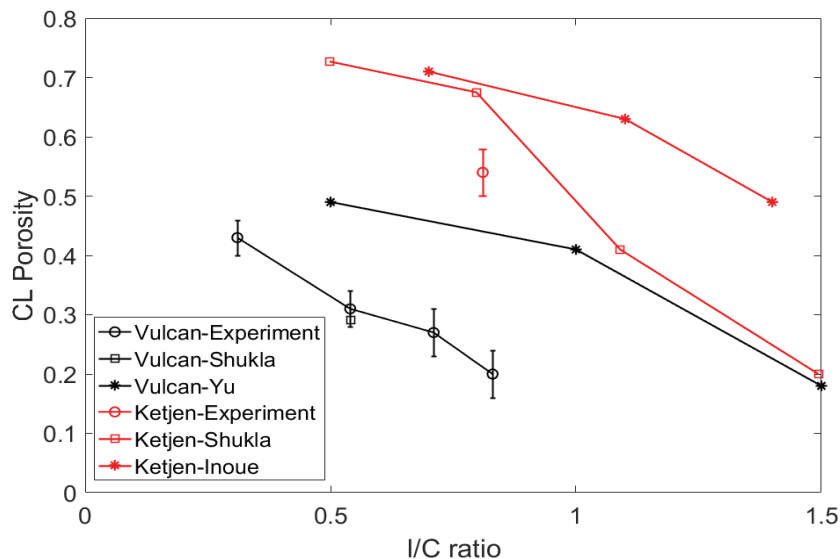


Figure 3.15: Variation in CL porosity with I/C ratio obtained experimentally and reported by Shukla et al. [69, 72], Yu et al. [36], Inoue et al. [46]

3.3 Governing equation and data analysis

3.3.1 Governing equation

3.3.1.1 GDL permeability

The governing equation for GDL through-plane permeability is obtained using the same process as in section 2.3.1.1.

3.3.1.2 CL permeability and effective pore diameter

Equation (2.7) is used for the uncompressed GDL samples. However, for the CL sample, the pore diameter is much smaller and Knudsen slip effects are found to be significant. Therefore, the Darcy's law can not accurately predict the permeability even at low Reynolds numbers. In the absence of inertial effects, the total flux is made up of two parts: viscous flux and Knudsen slip flux. In the experiment, very low mass flow rates (0-0.1 SLPM) were used to measure the permeability of the CL so that inertial effects could be ignored. This is expected to be the regime where the CL would operate. Knudsen proposed an semi-experimental expression to predict gas transport in the regime where $Kn \gg 1$, as explained by Cunningham and Williams [73]. At sufficiently high pressures, the Knudsen's expression for a capillary can be simplified to [25, 73]:

$$\dot{n} = -\frac{r_c^2}{8\eta} \frac{P_1 + P_2}{2} \frac{1}{RT} \frac{P_2 - P_1}{x_2 - x_1} - D_K \frac{c_1^k}{c_2^k} \frac{1}{RT} \frac{P_2 - P_1}{x_2 - x_1} = -\left(\frac{r_c^2}{8\eta} \frac{P_1 + P_2}{2} + D_K \frac{c_1^k}{c_2^k}\right) \frac{1}{RT} \frac{P_2 - P_1}{x_2 - x_1} \quad (3.7)$$

where r_c is the radius of the capillary, c_1^k and c_2^k are constants that depend on the gas and capillary, D_K is Knudsen diffusivity (m^2/s). The first term in equation (3.7) represents viscous flux and second term is Knudsen slip flux. Adzumi [74] [75] calculated c_1^k/c_2^k for several materials and Kerkhof [76] suggested that for engineering purposes:

$$\frac{c_1^k}{c_2^k} \approx 0.89 \quad (3.8)$$

Also, the Knudsen diffusivity in a capillary is given by [73]:

$$D_K = \frac{2r_c}{3} \sqrt{\frac{8RT}{\pi M}} \quad (3.9)$$

In order to apply Knudsen's expression to porous media, the following substitutions are made [26]:

$$\frac{r_c^2}{8} \Rightarrow B_v \quad (3.10)$$

Applying equation (3.8) and (3.10) to equation (3.7) and accounting for effective Knudsen diffusivity gives:

$$\dot{n} = -\left(\frac{B_v}{\eta} \frac{P_1 + P_2}{2} + 0.89 D_K^{eff}\right) \frac{1}{RT} \frac{P_2 - P_1}{x_2 - x_1} \quad (3.11)$$

where $x_2 - x_1$ is equal to the thickness of the sample, L . Applying ideal gas law to equation (3.11) gives: [25]

$$v = \frac{B_v}{2\eta L} \left(\frac{P_1^2 - P_2^2}{P_1} \right) + 0.89 \frac{D_K^{eff}}{L} \left(\frac{P_1 - P_2}{P_1} \right) = \frac{B_v}{2\eta L} \left(\frac{P_1^2 - P_2^2}{P_1} \right) + 0.89 d_p^{eff} \frac{1}{3} \sqrt{\frac{8RT}{\pi M}} \frac{1}{L} \left(\frac{P_1 - P_2}{P_1} \right) \quad (3.12)$$

where the effective Knudsen diffusivity D_K^{eff} is equal to $d_p^{eff} \frac{1}{3} \sqrt{\frac{8RT}{\pi M}}$ and d_p^{eff} is the effective pore diameter. Experimental data is fitted to equation (3.12) to obtain d_p^{eff} and gas-independent B_v .

The effective Knudsen diffusivity is dependent on the molar mass of the working fluid and pore geometry. To obtain the pressure drop across the CL, three filter replicates are measured prior to measuring the CL/filter sample and the pressure drop across the filter is recorded. The pressure drop across the CL is then obtained by subtracting ΔP_{filter} from ΔP_{total} . Experimental data are used to fit equation (3.12) to extract the permeability and CL effective pore diameter.

3.3.1.3 GDL through-plane diffusivity

In my experimental setup, oxygen transport in the GDL is driven by both diffusion and convection. Fick's first law is used to describe diffusion transport of species i assuming an infinite dilute mixture, defined as [59]:

$$\dot{m}_i^D = -\rho_t D_{ij} \frac{dw_i}{dx} \quad (3.13)$$

where \dot{m}_i^D is the diffusive mass flux of the species i with respect to a reference frame moving with mixture velocity v . The total mass flux \dot{m}_i , given as the sum of convective flux \dot{m}_i^C and diffusive flux \dot{m}_i^D , is then:

$$\dot{m}_i^D = \dot{m}_i - \dot{m}_i^C = \rho_i v_i - \rho_i v \quad (3.14)$$

Then equation (3.14) can be written as:

$$\dot{m}_i^D = \rho_i v_i - \rho_i v = -\rho_t D_{ij} \frac{dw_i}{dx} \quad (3.15)$$

where v is the mass-average mixture velocity, defined as:

$$v = \frac{\sum \rho_i v_i}{\sum \rho_i} = \frac{\sum \rho_i v_i}{\rho_t} = \sum w_i v_i \quad (3.16)$$

Assuming the gas mixture (oxygen and nitrogen) flow in one-direction, in the absence of chemical reaction, equation (3.15) can be expressed as,

$$\rho_t D_{N_2, O_2}^{eff} \frac{dw_{O_2}}{dx} = \rho_{O_2} v - \rho_{O_2} v_{O_2} \quad (3.17)$$

where D_{N_2, O_2}^{eff} is the effective diffusivity of oxygen in nitrogen. Equation (3.17) can be further rearranged as:

$$\rho_t D_{N_2, O_2}^{eff} \frac{dw_{O_2}}{dx} = \rho_{O_2} \frac{\dot{m}_t}{\rho_t} - \rho_{O_2} \frac{\dot{m}_{O_2}}{\rho_{O_2}} \Rightarrow \frac{dw_{O_2}}{dx} = \frac{1}{D_{N_2, O_2}^{eff}} \left(w_{O_2} \frac{\dot{m}_t}{\rho_t} - \frac{\dot{m}_{O_2}}{\rho_t} \right) \quad (3.18)$$

where w_{O_2} is the mass fraction of oxygen, \dot{m}_t and \dot{m}_{O_2} are the mass flux of gas mixture and mass flux of oxygen across sample. Applying mass conservation to the flow path in the porous media, assuming steady state flow in one-direction, in the absence of chemical reaction, the mass flux of oxygen and gas mixture is given by:

$$\frac{d\dot{m}_{O_2}}{dx} = 0 \quad (3.19)$$

$$\frac{d\dot{m}_t}{dx} = 0 \quad (3.20)$$

Based on the discussion in section 3.3.1.1, for one-dimension flow, Darcy's equation can be written as:

$$\frac{dP_t}{dx} = -\frac{\eta}{B_v} v = -\frac{\eta}{B_v} \frac{\dot{m}_t}{\rho_t} \quad (3.21)$$

where ρ_t is expressed as:

$$\rho_t = \frac{P_t}{RT} \sum w_i M_i = -\frac{P_t}{RT} (w_{O_2} M_{O_2} + (1 - w_{O_2}) M_{N_2}) \quad (3.22)$$

Equations (3.18)-(3.21) are used as governing equations for through-plane diffusivity, with four unknowns to solve: (1) \dot{m}_{O_2} : oxygen mass flux in the porous media, (2) \dot{m}_t : total mass flux in the porous media, (3) P_t : total gas pressure, (4) w_{O_2} : oxygen mass fraction in the porous media. The equations are solved using the MATLAB bvp4c solver which requires four boundary conditions. Assume that the oxygen flux is swept away very quickly in the nitrogen channel, the following boundary conditions are used: (1) the oxygen mass fraction is zero, $w_{O_2}=0$, in the nitrogen channel, (2) the oxygen mass fraction is one, $w_{O_2}=1$, in the oxygen channel, (3) the total pressure is equal to the nitrogen pressure in the nitrogen channel, $P_t=P_{N_2}$, (4) the total pressure is equal to the oxygen pressure in the oxygen channel, $P_t=P_{O_2}$. Here, P_{N_2} is equal to the system back pressure which is controlled by BPC; P_{O_2} is

equal to the back pressure plus the pressure difference which is controlled by the DPC. The MATLAB code is available in the appendix.

3.3.1.4 CL diffusibility

As discussed before, diffusibility is a term used to describe gas diffusion in porous media and defined as:

$$\widehat{D} = \frac{D^{eff}}{D} \quad (3.23)$$

where \widehat{D} is diffusibility, D^{eff} is effective diffusivity (m²/s) and D is gas bulk diffusivity (m²/s). In the case of a GDL, only molecular diffusion is considered so D is equal to molecular diffusivity. However, in the case of a CL, gas diffusion is in the transition region as discussed in previous sections and both molecular diffusion and Knudsen diffusion need to be considered. In this case, gas bulk diffusivity, D , is written as [36]:

$$\frac{1}{D} = \frac{1}{D_K} + \frac{1}{D_M} \quad (3.24)$$

where D_M is molecular diffusivity, D_K is Knudsen diffusivity which is calculated as [36]:

$$D_K = \frac{d_p}{3} \sqrt{\frac{8RT}{\pi M}} \quad (3.25)$$

where d_p is local pore diameter, M is molar mass of the gas, R is gas constant, T is temperature. The relation between CL effective diffusivity and bulk diffusivity is always expressed as a function of porosity ϵ :

$$D^{eff} = f(\epsilon)D \quad (3.26)$$

Combining equation (3.26) and (3.24) gives:

$$\frac{1}{f(\epsilon)D} = \frac{1}{f(\epsilon)D_K} + \frac{1}{f(\epsilon)D_M} \Rightarrow \frac{1}{D^{eff}} = \frac{1}{D_K^{eff}} + \frac{1}{D_M^{eff}} \quad (3.27)$$

where D_K^{eff} is the effective Knudsen diffusivity obtained from permeability experiment, D^{eff} is measured in the diffusivity experiment and D_M^{eff} is the effective molecular diffusivity.

Fick's first law is widely used to estimate the diffusive flux of a species in a steady state system. In this case, Fick's first law is written in one dimension as [59]:

$$\dot{m}_i^D = -\rho_t D_{ij} \frac{dw_i}{dx} \quad (3.28)$$

where \dot{m}_i^D is the diffusion flux in $\text{kg}/\text{m}^2\cdot\text{s}$, ρ_t is total density in kg/m^3 , D_{ij} is the diffusion coefficient or diffusivity in m^2/s . In porous media, D_{ij} is usually replaced by D_{ij}^{eff} in order to account for the porous media. In the experiment, oxygen is transported across the CL/filter by diffusion from the oxygen channel to the nitrogen channel. Assuming a linear variation in mass fraction, equation (3.28) can be written in discrete form as:

$$\dot{m}_{O_2}^D = D_{N_2,O_2}^{eff} \frac{\rho_t \Delta w_{O_2}}{L} \quad (3.29)$$

where $\dot{m}_{O_2}^D$ is superficial oxygen diffusive mass flux in CL sample ($\text{kg}/\text{m}^2\cdot\text{s}$), D_{N_2,O_2}^{eff} is the effective diffusivity of CL/filter sample (m^2/s), w_{O_2} is oxygen mass fraction, L is the thickness of sample and ρ_t is the interstitial gas mixture density in the sample. The latter is approximated to be $\frac{\rho_{O_2} + \rho_{N_2}}{2}$.

According to the mass conservation, the mass of oxygen that flows into the nitrogen channel through the CL sample is equal to the mass of oxygen that leaves the nitrogen channel. The mass flux of oxygen flowing out of the nitrogen channel is:

$$\dot{M}_{O_2}^{out} = \rho_{O_2} \dot{V}_{O_2} = \dot{V}_t x_{O_2} \rho_{O_2} \approx \dot{V}_{N_2} x_{O_2} \rho_{O_2} \quad (3.30)$$

where $\dot{M}_{O_2}^{out}$ is oxygen mass flow rate out of nitrogen channel (kg/s), x_{O_2} is the oxygen molar fraction in nitrogen channel measured by oxygen sensor, \dot{V}_t is volume flow rate of gas out of channel and \dot{V}_{N_2} is the volume flow rate of N_2 controlled by MFC (LPM). Equation (3.30) is based on the assumption that an equal amount of N_2 diffuses through CL sample into O_2 channel as O_2 diffuses through GDL into N_2 channel, then \dot{V}_{N_2} is approximately the same as the total volume rate in the N_2 channel.

Since oxygen transport through the CL sample is driven only by diffusion because of the very low permeability of CLs, the mass flux of oxygen flowing into nitrogen channel through the CL/filter sample can be simply written as:

$$\dot{M}_{O_2}^{in} = \rho_t D_{N_2,O_2}^{eff} A \frac{\Delta w_{O_2}}{L} \quad (3.31)$$

where $\dot{M}_{O_2}^{in}$ is the oxygen diffusive mass flow rate into the nitrogen channel through the CL/filter sample (kg/s) and A is the cross-sectional area. Assuming w_{O_2} is 0 in the nitrogen channel and 1 in the oxygen channel, equation (3.31) results in:

$$\dot{M}_{O_2}^{in} = D_{N_2,O_2}^{eff} A \frac{\rho_t}{L} \quad (3.32)$$

According to mass conservation, $\dot{M}_{O_2}^{in} = \dot{M}_{O_2}^{out}$, then:

$$D_{N_2, O_2}^{eff} A \frac{\rho_t}{L} = \dot{V}_{N_2} x_{O_2} \rho_{O_2} \quad (3.33)$$

D_{N_2, O_2}^{eff} is finally written as:

$$D_{N_2, O_2}^{eff} = \frac{\dot{V}_{N_2} \rho_{O_2} x_{O_2} L}{A \rho_t} = \frac{2\dot{V}_{N_2} \rho_{O_2} x_{O_2} L}{A (\rho_{O_2} + \rho_{N_2})} \quad (3.34)$$

Equation (3.34) is used to calculate the through-plane effective diffusivity of the CL/filter. Matlab code is available in the appendix. Three filter replicates were measured prior to measuring the CL/filter and the filter diffusivity was obtained. To obtain the CL diffusivity, the diffusion resistance network needs to be analysed first, shown in Figure 3.16.

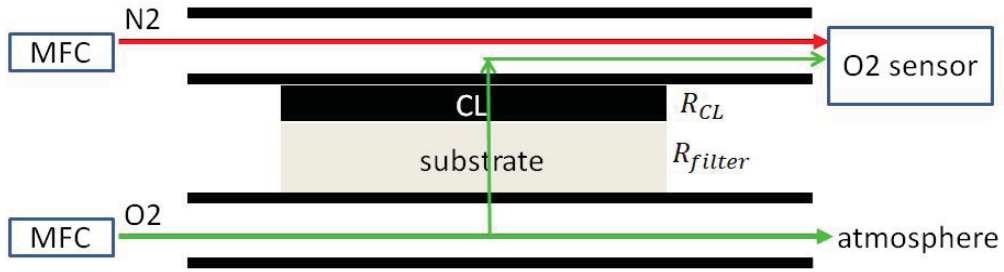


Figure 3.16: Diffusion resistance network of CL/filter sample

Diffusion resistance that arises from the filter can be expressed as:

$$R_{filter} = \frac{L_{filter}}{D_{filter}^{eff} A} \quad (3.35)$$

Similarly, diffusion resistance of the CL is :

$$R_{CL} = \frac{L_{CL}}{D_{CL}^{eff} A} \quad (3.36)$$

Then, total diffusion resistance can be written as:

$$R_{total} = \frac{L_{total}}{D_{total}^{eff} A} = \frac{L_{filter}}{D_{filter}^{eff} A} + \frac{L_{CL}}{D_{CL}^{eff} A} \quad (3.37)$$

Therefore, effective diffusivity of CL is expressed as:

$$D_{CL}^{eff} = \frac{L_{CL}}{\frac{L_{total}}{D_{total}^{eff}} - \frac{L_{filter}}{D_{filter}^{eff}}} \quad (3.38)$$

where A is the cross-sectional area, L_{CL} and L_{filter} are the thickness of CL and filter, respectively.

3.3.2 Data analysis

3.3.2.1 GDL permeability

In order to obtain viscous and inertial permeability in equation (2.7), the inlet channel pressure P_1 , and the molar flux of gas \dot{n} are measured. The molar flux \dot{n} in equation (2.7) is calculated using $\dot{n} = P_{standard} v / RT^\circ$, where $P_{standard}$ is the standard atmospheric pressure, i.e., 101325 Pa and T° is 298K. The inlet gas velocity v is obtained using $v = \frac{\dot{V}}{A}$, where \dot{V} is the volume flow rate at standard conditions controlled by the MFC in SLPM. P_1 is measured directly by the pressure transducer and P_2 is at ambient pressure. The experimental data is used to fit to equation (2.7) using a Python code to extract viscous permeability B_v and inertial permeability B_l . The code is used for the data fitting by employing a least squares regression technique. Simulations at different gas velocity with different permeability values are performed and a residual function is defined as:

$$Res = \sum_{i=10}^n (P_{1,exp} - P_{1,num}(B_v, B_l))^2 \quad (3.39)$$

where $P_{1,exp}$ is the experimental inlet pressure measured by PT, and $P_{1,num}$ is the numerical estimate of the inlet pressure obtained from equation (2.7). The values of B_v and B_l which minimize the residual function represent the permeabilities of GDL.

3.3.2.2 CL permeability

In order to obtain the viscous permeability and Knudsen diffusivity of the CL samples, permeability experiments are performed using both nitrogen and helium respectively. Inlet velocity and pressure drop are measured in the experiment. A volume flow rate of 0-0.1 SLPM, considered to be small enough to make the inertial effect negligible, is controlled with the MFC. The experimental data is used to fit simultaneously d_p^{eff} and B_v in equation (3.12). A loop is run for different values of d_p^{eff} , and each value of d_p^{eff} combines with different

values of B_v to calculate the residual using the combined experimental data of nitrogen and helium. The residual is defined as:

$$Res = \sum_{i=10}^n (P_{1,exp} - P_{1,num}(B_v, d_p^{eff}))^2 \quad (3.40)$$

where $P_{1,exp}$ and $P_{1,num}$ are the experimental inlet gas pressure measured by PT and numerical estimate of inlet gas pressure computed from equation (3.12). The corresponding combination of d_p^{eff} and B_v is taken as final fitting result when the residual is minimized.

3.3.2.3 GDL diffusivity

In order to obtain the effective diffusivity of the GDL sample, the pressure drop is controlled by DPC and the oxygen molar fraction in the nitrogen channel is measured by the oxygen sensor. The total molar flux in the nitrogen channel is then calculated using the channel flow rate and oxygen molar fraction at the outlet in order to obtain the oxygen flux across the sample. The total net molar flux leaving the nitrogen channel consists of four parts: (1) the nitrogen flow into the nitrogen channel from the MFC, (2) the gas flow into the nitrogen channel across the GDL due to convection, (3) the oxygen flow into the nitrogen channel across the GDL by diffusion, and (4) the nitrogen flow out of the channel across the GDL by diffusion. Then, the total net molar flux leaving the nitrogen channel is (1)+(2)+(3)-(4). The molar flux of nitrogen out of the nitrogen channel and the molar flux of oxygen into the nitrogen channel are very small compared to the nitrogen flux from the MFC, i.e., (3) \ll (1) and (4) \ll (1). Also, since the molar flux of the two gases by diffusion are very close, i.e., (3) \approx (4), thus (3)-(4) is negligible compared to (1)+(2). As a result, the total molar flux leaving the nitrogen channel is equal to (1)+(2). The nitrogen molar flux into the channel from MFC is calculated by:

$$\dot{n}_{ch} = \frac{\rho_{N_2} \dot{V}}{M_{N_2} A} \quad (3.41)$$

where \dot{n}_{ch} is nitrogen molar flux from MFC (mol/m² s), ρ_{N_2} is density of nitrogen at system pressure, \dot{V} is the volume flow rate at experimental condition set by MFC (LPM), M_{N_2} is molar mass of nitrogen. The molar flux of gas into the channel through the sample is calculated as:

$$\dot{n}_{sample} = \frac{P_t v}{RT} \quad (3.42)$$

where \dot{n}_{sample} is molar flux of gas through the sample (mol/m² s) by convection, P_t is total pressure controlled by back pressure controller and differential pressure controller, A is the

flow area of the sample, v is the superficial gas velocity in the porous media, calculated as $\frac{B_v \Delta P}{\eta L}$, where $\eta \approx (\eta_{O_2} + \eta_{N_2})/2$ and B_v is calculated in permeability experiment. Then, the total oxygen mass flux in the porous media calculated using experimental data can be estimated as:

$$\dot{m}_{O_2,exp} = x_{O_2}(\dot{n}_{ch} + \dot{n}_{sample})M_{O_2} \quad (3.43)$$

where $\dot{m}_{O_2,exp}$ is experimental oxygen mass flux across the sample (kg/m² s), x_{O_2} is the oxygen volume fraction measured by oxygen sensor.

To estimate \dot{m}_{O_2} , \dot{m}_t , P_t and w_{O_2} , equations (3.18)-(3.21) are solved using the MATLAB bvp4c solver. A loop is run for effective diffusivity D_{N_2,O_2}^{eff} , and the residual is calculated as the square of the difference between the numerical mass flux \dot{m}_{O_2} and experimental mass flux $\dot{m}_{O_2,exp}$ at different pressure drop, as shown in equation (3.44).

$$Res = \sum_{i=1}^5 \left(\dot{m}_{O_2} - \dot{m}_{O_2,exp}(\Delta P_i, D_{N_2,O_2}^{eff}) \right)^2 \quad (3.44)$$

The estimated effective diffusivity, D_{N_2,O_2}^{eff} is the value that minimizes the residual.

3.3.2.4 CL diffusivity

In order to obtain the through-plane effective diffusivity of the CL sample, the volume flow rate of nitrogen and oxygen are controlled by two MFCs (Cole-Parmer, model: RK-32907-69, range: 0 - 5 SLPM) and the oxygen molar fraction in the nitrogen channel is measured by an oxygen sensor (Ocean Optics, Model: FOSPOR-600-32MM, range: 0 - 21% in gas). Assuming that the diffusive flux of oxygen and nitrogen across the CL sample are equal, and both of them are much less than the nitrogen flow from the MFC (details in results section), then the total volume flux in the nitrogen channel is considered to be approximately equal to the value from MFC. The PTFE filter was measured before measuring CL/filter sample, then the through-plane effective diffusivity of CL is obtained using equation (3.34) and (3.38).

3.4 Uncertainty analysis

In this section, the uncertainty analysis of through-plane permeability and diffusivity will be conducted by following the steps for in-plane permeability and diffusivity uncertainty analysis. DPC and BPC will also be discussed as they are used in through-plane diffusivity

experiment of GDL.

3.4.1 Mass flow controller uncertainty

Mass flow controller uncertainties have been presented in previous chapter.

3.4.2 Pressure transducer uncertainty

Pressure transducer uncertainties have been presented in previous chapter.

3.4.3 Differential pressure controller uncertainty

The differential pressure controller is produced and calibrated by Cole-Parmer. The full range is 500 Pa, and the accuracy is 0.25% of full scale=0.25%×500 Pa=1.25 Pa. The precision uncertainty is provided by manufacturer as 0.05%×500 Pa=0.25 Pa. The overall uncertainty of DPC was then calculated as:

$$w_{DPC} = \sqrt{B_{DPC}^2 + P_{DPC}^2} = \sqrt{1.25^2 + 0.25^2} = 1.27 \text{ Pa} \quad (3.45)$$

3.4.4 Back pressure controller uncertainty

The back pressure controller is from Cole-Parmer. The accuracy is 0.25% of full scale=0.25%×100 Psi=0.25 Psi, and the provided precision uncertainty is 0.05%×100 Psi=0.05 Psi. The overall uncertainty was then:

$$w_{BPC} = \sqrt{B_{BPC}^2 + P_{BPC}^2} = \sqrt{0.25^2 + 0.05^2} = 0.255 \text{ Psi} = 1758 \text{ Pa} \quad (3.46)$$

3.4.5 Oxygen sensor uncertainty

The oxygen sensor uncertainty and calibration have been discussed for the case of in-plane diffusivity measurements of GDL. In the case of through-plane diffusivity experiment of GDL and CL, the overall uncertainty of oxygen sensor was taken as 5% of the reading.

3.4.6 Thickness measurement uncertainty

The thickness of sample is measured by a micrometer (Mitutoyo Japan, Series NO.:008395) at a load of 0.5 N. As discussed in chapter 2, the uncertainty of the micrometer has been validated by shims of different thickness and the overall accuracy is provided by manufacturer as 2 μm . As discussed in catalyst layer characterization section, the thickness measured by

the micrometer is in good agreement with SEM imaging thickness and therefore, the CL thickness uncertainty can be calculated using the SEM imaging data shown in Table 3.1.

3.4.7 Permeability uncertainty

Based on the discussion above, the uncertainty in function f is computed using the uncertainties in each variable, shown as equation (2.17). Ignoring the Forcheimer term due to its insignificant effect on permeability, the permeability can be expressed as:

$$B_v = 2RT\eta \left(\frac{\dot{n}L}{P_1^2 - P_2^2} \right) \quad (3.47)$$

Taking R , T , η and P_2 as constants, then the permeability uncertainty is given as:

$$w_{B_v} = 2RT\eta \sqrt{\left(w_{\dot{n}} \frac{L}{P_1^2 - P_2^2} \right)^2 + \left(w_L \frac{\dot{n}}{P_1^2 - P_2^2} \right)^2 + \left(w_{\Delta P_{PT}} \frac{2\dot{n}LP_1}{(P_1^2 - P_2^2)^2} \right)^2} \quad (3.48)$$

as $P_1 = P_2 + \Delta P_{PT}$ and using equation (3.47), then:

$$\frac{w_{B_v}}{B_v} = \sqrt{\left(\frac{w_{\dot{n}}}{\dot{n}} \right)^2 + \left(\frac{w_L}{L} \right)^2 + \left(\frac{2w_{\Delta P_{PT}}}{\Delta P_{PT}} \frac{(P_2 + \Delta P_{PT})}{(2P_2 + \Delta P_{PT})} \right)^2} \quad (3.49)$$

The through-plane permeability uncertainty for GDL and CL are different due to the different experimental conditions. In the experiment, the flow rate varies from 0-1 SLPM for GDL and 0-0.1 SLPM for CL. According to the overall uncertainty provided in Table 2.1 and 2.2, the average overall uncertainty in the flow rate is taken as 4% for GDL and 15% for CL. The pressure drop across sample under experimental condition usually varies from several hundred to several thousand pascals. Therefore, the average overall uncertainty in pressure transducer is taken as 1% for GDL and 0.5% for CL. The uncertainty in thickness is taken as 0.5% for GDL based on micrometer uncertainty and 8% for CL based on SEM imaging data shown in Table 3.1. As ΔP_{PT} is much smaller than air pressure P_2 , $\frac{(P_2 + \Delta P_{PT})}{(2P_2 + \Delta P_{PT})}$ can be approximately taken as 0.5, then

$$\text{For GDL : } \frac{w_{B_v}}{B_v} = \sqrt{(4\%)^2 + (1\%)^2 + (0.5\%)^2} = \pm 4.2\% \quad (3.50)$$

$$\text{For CL : } \frac{w_{B_v}}{B_v} = \sqrt{(15\%)^2 + (0.5\%)^2 + (8\%)^2} = \pm 17\% \quad (3.51)$$

Precision experiments were also conducted following the same step shown in previous chapter

and the deviation fell in the accepted range.

3.4.8 Experimental permeability precision uncertainty

In order to experimentally measure the permeability precision uncertainty of the setup, six experiments are repeated for the same Toray-90 (0%PTFE) sample without opening/closing the diffusion bridge and the results are compared. Results are shown in Table 3.3. The through-plane permeability for Toray-90 (0%PTFE) is $1.05 \pm 0.004 \times 10^{-11} (m^2)$. The standard deviation is calculated using equation (2.18), therefore P_x in equation (2.19) is calculated to be $0.004 \times 10^{-11} (m^2)$. The measurement uncertainty, P_x/B_v is calculated to be 0.38%, thus the setup precision is better than the theoretical precision calculated using equation (3.50).

Table 3.3: Toray-90 (0%PTFE) through-plane permeability

	$B_v(N_2) \times 10^{-11} (m^2)$
Measurement 1	1.06
Measurement 2	1.05
Measurement 3	1.05
Measurement 4	1.05
Measurement 5	1.06
Measurement 6	1.05

3.4.9 Diffusivity uncertainty

GDL diffusivity uncertainty - Recall that the oxygen mass flux in the porous media can be calculated using equation (3.43) from which it is known that the diffusivity uncertainty is decided by two terms and it can be calculated separately. Take M_{O_2} , R , T , η and A as constants, then:

First term:

$$\dot{m}_1 = x_{O_2} \dot{n}_{ch} M_{O_2} \quad (3.52)$$

Second term:

$$\dot{m}_2 = x_{O_2} \dot{n}_{sample} M_{O_2} = x_{O_2} M_{O_2} \frac{P_t \Delta P B_v}{R T \eta L} \quad (3.53)$$

Uncertainty in the first term:

$$w_{\dot{m}_1} = M_{O_2} \sqrt{(w_{x_{O_2}} \dot{n}_{ch})^2 + (w_{\dot{n}_{ch}} x_{O_2})^2} \quad (3.54)$$

$$\frac{w_{\dot{m}_1}}{\dot{m}_1} = \sqrt{\left(\frac{w_{\dot{n}_{ch}}}{\dot{n}_{ch}}\right)^2 + \left(\frac{w_{x_{O_2}}}{x_{O_2}}\right)^2} \quad (3.55)$$

Uncertainty in the second term :

$$w_{\dot{m}_2} = \frac{M_{O_2}}{RT\eta} \left(\left(w_{x_{O_2}} \frac{P_t B_v \Delta P}{L} \right)^2 + \left(w_{P_t} \frac{w_{x_{O_2}} B_v \Delta P}{L} \right)^2 + \left(w_{B_v} \frac{w_{x_{O_2}} P_t \Delta P}{L} \right)^2 + \left(w_{\Delta P} \frac{P_t B_v w_{x_{O_2}}}{L} \right)^2 + \left(w_L \frac{w_{x_{O_2}} P_t B_v \Delta P}{L^2} \right)^2 \right)^{\frac{1}{2}} \quad (3.56)$$

$$\frac{w_{\dot{m}_2}}{\dot{m}_2} = \sqrt{\left(\frac{w_{x_{O_2}}}{x_{O_2}}\right)^2 + \left(\frac{w_{P_t}}{P_t}\right)^2 + \left(\frac{w_{B_v}}{B_v}\right)^2 + \left(\frac{w_{\Delta P}}{\Delta P}\right)^2 + \left(\frac{w_L}{L}\right)^2} \quad (3.57)$$

To measure the GDL diffusivity, pressure difference ΔP is controlled to be 2 to 10 Pa, gas flow rate is set at 1 SLPM, the system pressure is maintained at 10 Psig. Under experimental conditions, the uncertainty in \dot{n}_{ch} is about 1.5% (see table 2.1), x_{O_2} is 5%, P_t is 1.1% (controlled by BPC), B_v is 4.15%, ΔP is 15% and L is 0.5%, then the uncertainty for GDL will approximately be:

$$\frac{w_{\dot{m}_1}}{\dot{m}_1} = \sqrt{1.5\%^2 + 5\%^2} = 5.2\% \quad (3.58)$$

$$\frac{w_{\dot{m}_2}}{\dot{m}_2} = \sqrt{5\%^2 + 1.1\%^2 + 4.15\%^2 + 15\%^2 + 0.5\%^2} = 16.4\% \quad (3.59)$$

In summary, the diffusivity uncertainty is always decided by two terms, so it should be described by a range instead of a single constant. The diffusivity uncertainty varies from 5.2% - 16.4% for GDL and the biggest error source is the differential pressure controller.

CL/filter diffusivity uncertainty - The analysis of diffusivity uncertainty for CL/filter follows the same procedure of in-plane diffusivity of GDL. According to equation (3.34), the overall uncertainty of through-plane diffusivity for CL/filter is calculated as:

$$w_{D_{N_2, O_2}^{eff}} = \frac{2\rho_{O_2}}{\rho_{O_2} + \rho_{N_2}} \sqrt{\left(w_{\dot{V}} \frac{x_{O_2} L}{A} \right)^2 + \left(w_{x_{O_2}} \frac{\dot{V} L}{A} \right)^2 + \left(w_L \frac{x_{O_2} \dot{V}}{A} \right)^2 + \left(w_A \frac{x_{O_2} \dot{V} L}{A^2} \right)^2} \quad (3.60)$$

Dividing both side by D_{N_2, O_2}^{eff} gives:

$$\frac{w_{D_{N_2, O_2}^{eff}}}{D_{N_2, O_2}^{eff}} = \sqrt{\left(\frac{w_{\dot{V}}}{\dot{V}}\right)^2 + \left(\frac{w_{x_{O_2}}}{x_{O_2}}\right)^2 + \left(\frac{w_L}{L}\right)^2 + \left(\frac{w_A}{A}\right)^2} \quad (3.61)$$

Here are four terms of uncertainties: (1) the overall uncertainty in flow rate is 1.5% under experimental condition, (2) the overall uncertainty in oxygen sensor is 5% of reading, (3) The uncertainty in thickness of CL/filter is $2\mu\text{m}/80\mu\text{m}=2.5\%$, and (4) the error in cross-sectional area is less than 4%. Substituting all the values into (3.61) gives the overall uncertainty of through-plane diffusivity of CL/filter:

$$\frac{w_{D_{N_2, O_2}^{eff}}}{D_{N_2, O_2}^{eff}} = \sqrt{(1.5\%)^2 + (5\%)^2 + (2.5\%)^2 + (4\%)^2} = \pm 7\% \quad (3.62)$$

CL diffusivity uncertainty - The CL diffusivity is calculated using equation (3.38) with D_{filter}^{eff} and D_{total}^{eff} obtained from diffusivity experiment. Taking $\frac{L_{total}}{D_{total}^{eff}}$ and $\frac{L_{filter}}{D_{filter}^{eff}}$ as one entity respectively, equation (3.38) is rewritten as:

$$D_{CL}^{eff} = \frac{L_{CL}}{\frac{L_{total}}{D_{total}^{eff}} - \frac{L_{filter}}{D_{filter}^{eff}}} = \frac{L_{CL}}{a - b} \quad (3.63)$$

here, a is equal to $\frac{L_{total}}{D_{total}^{eff}}$ and b is equal to $\frac{L_{filter}}{D_{filter}^{eff}}$. For simplicity, D_{filter}^{eff} and D_{total}^{eff} are written as D_f and D_t , and L_{total} and L_{filter} are written as L_t and L_f in this subsection. The uncertainty in a and b are calculated respectively.

For a which is $\frac{L_{total}}{D_{total}^{eff}}$:

$$a = \frac{L_{total}}{D_{total}} = \frac{\rho_t A}{\rho_{O_2} \dot{V}_{N_2} x_{O_2}} \quad (3.64)$$

the uncertainty in a is expressed as:

$$\frac{w_a}{a} = \sqrt{\left(\frac{w_{\dot{V}}}{\dot{V}}\right)^2 + \left(\frac{w_{x_{O_2}}}{x_{O_2}}\right)^2 + \left(\frac{w_A}{A}\right)^2} \quad (3.65)$$

the uncertainty in each parameter has been discussed before and the uncertainty in a is calculated as:

$$\frac{w_a}{a} = \sqrt{(1.5\%)^2 + (5\%)^2 + (4\%)^2} = \pm 6.5\% \quad (3.66)$$

and the uncertainty in b is calculated to be the same:

$$\frac{w_b}{b} = \sqrt{(1.5\%)^2 + (5\%)^2 + (4\%)^2} = \pm 6.5\% \quad (3.67)$$

To calculate the uncertainty in D_{CL}^{eff} , the partial derivative with respect to each parameter

is expressed as:

$$\frac{\partial D_{CL}^{eff}}{\partial L_{CL}} = \frac{1}{a-b} \quad (3.68)$$

$$\frac{\partial D_{CL}^{eff}}{\partial a} = \frac{-L_{CL}}{(a-b)^2} \quad (3.69)$$

$$\frac{\partial D_{CL}^{eff}}{\partial b} = \frac{L_{CL}}{(a-b)^2} \quad (3.70)$$

Then, the overall uncertainty in D_{CL}^{eff} is expressed as:

$$w_{D_{CL}^{eff}} = \sqrt{\left(w_{L_{CL}} \frac{\partial D_{CL}^{eff}}{\partial L_{CL}}\right)^2 + \left(w_a \frac{\partial D_{CL}^{eff}}{\partial a}\right)^2 + \left(w_b \frac{\partial D_{CL}^{eff}}{\partial b}\right)^2} \quad (3.71)$$

The equation (3.71) is further written as:

$$\frac{w_{D_{CL}^{eff}}}{D_{CL}^{eff}} = \sqrt{\left(\frac{w_{L_{CL}}}{L_{CL}}\right)^2 + \left(\frac{w_a}{a-b}\right)^2 + \left(\frac{w_b}{a-b}\right)^2} \quad (3.72)$$

The uncertainty in a and b has been calculated to be 6.5%, so w_a and w_b are equal to $0.065a$ and $0.065b$ respectively. The uncertainty in L_{CL} is measured to be 8% by SEM imaging, therefore:

$$\frac{w_{D_{CL}^{eff}}}{D_{CL}^{eff}} = \sqrt{(8\%)^2 + \left(\frac{0.065}{1-\frac{b}{a}}\right)^2 + \left(\frac{0.065}{1-\frac{a}{b}}\right)^2} \quad (3.73)$$

It can be seen that the overall uncertainty is dependent on the ratio of $\frac{a}{b}$, i.e., $\frac{L_t D_f}{L_f D_t}$. The CL thickness is between 4 and 6 μm and the filter thickness is around 80 μm so $\frac{L_f}{L_t}$ is taken as 0.94. The filter diffusivity is approximately 20% higher than CL/filter entity based on experimental raw data which will be shown in the results and discussion section, then the value of $\frac{D_f}{D_t}$ is taken as 1.2. The uncertainty in D_{CL}^{eff} is finally calculated as:

$$\frac{w_{D_{CL}^{eff}}}{D_{CL}^{eff}} = \sqrt{(8\%)^2 + \left(\frac{0.065}{1-0.78}\right)^2 + \left(\frac{0.065}{1.3-1}\right)^2} = \sqrt{(8\%)^2 + (22.3\%)^2 + (30.5\%)^2} = 38\% \quad (3.74)$$

Based on the uncertainty analysis in this section, the uncertainty in CL diffusivity is higher than CL/filter diffusivity because $\frac{L_f}{L_t}$ and $\frac{D_f}{D_t}$ affect the CL diffusivity. According to equation (3.73), the uncertainty might be reduced to some degree by printing more number of layers of CL sample in order to decrease $\frac{L_f}{L_t}$ and increase $\frac{D_f}{D_t}$, however, increasing number of printed layers reduces the CL porosity and transport properties so 15 layers are printed in this study.

The high uncertainty means that our filter might not be the best material for this study, and the uncertainty could be reduced by selecting another filter with bigger pore diameter, so that the value of $\frac{D_f}{D_t}$ will increase and the uncertainty can be reduced to some degree. However, the filter pore diameter can not be too big otherwise more inks will penetrate into the filter pores and affect the results. The appropriate filter pore diameter should be around 200 nm because it gives higher filter diffusivity and prevents inks penetrating into the filter.

3.4.10 Experimental diffusivity precision uncertainty

In order to experimentally measure the diffusivity precision uncertainty of the setup, six experiments are repeated for the same material without opening/closing the diffusion bridge and the results were compared. A Toray-90 (0%PTFE) sample was measured and the experimental results are shown in Table 3.4. The through-plane diffusibility for the Toray-90 (0%PTFE) is 0.247 ± 0.006 . The standard deviation is calculated using equation (2.18), therefore P_x in equation (2.19) is calculated to be 0.006. The measurement uncertainty, P_x/B_v is calculated to be 2.42%, thus the setup accuracy is better than the theoretical accuracy calculated using equation (2.33).

Table 3.4: Toray-90 (0%PTFE) through-plane diffusibility

Diffusibility	
Measurement 1	0.255
Measurement 2	0.243
Measurement 3	0.243
Measurement 4	0.243
Measurement 5	0.255
Measurement 6	0.243

3.5 Results and discussion

3.5.1 Experimental results for Toray-90 samples and comparison with literature

This chapter mainly focuses on the measurements permeability and diffusivity for CL. However, before discussing the experimental results of CL, it is necessary to compare our GDL permeability and diffusivity results with literature in order to validate the reliability of the measurements. We move to discuss CL results later after making sure the setup is working properly.

3.5.1.1 Toray-90 GDL through-plane permeability and comparison to literature

To validate the reliability of the permeability measurement, the through-plane permeability of Toray-90 (0%PTFE) and Toray-90 (20%PTFE) is measured and results are compared to literature. Three replicates are measured for each type of sample and the pressure drop and gas flow rate vs. time are recorded during the experiment. The fluctuation of measured pressure is very small (shown in Figure 3.17). Figure 3.18 shows that the pressure drop across the GDL increases with higher gas velocity. It was also found that at the same gas velocity, the Toray-90 (20%PTFE) sample shows higher pressure drop than Toray-90 (0%PTFE). The through-plane permeability was found to decrease with increasing PTFE loading in GDL, which is consistent with literature results [27]. Permeability estimates are shown in Table 3.5 as well as literature data. Good agreement was found.

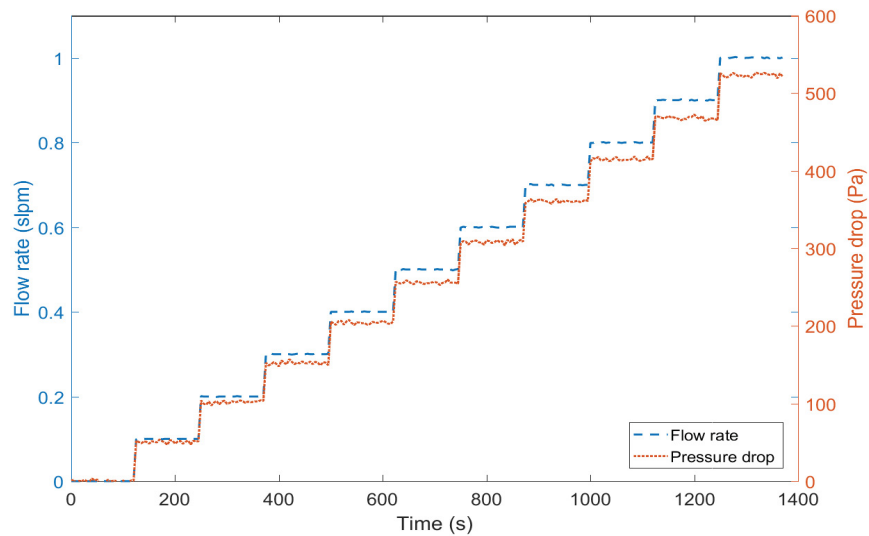


Figure 3.17: Inlet pressure vs time for Toray-90 with 0%PTFE

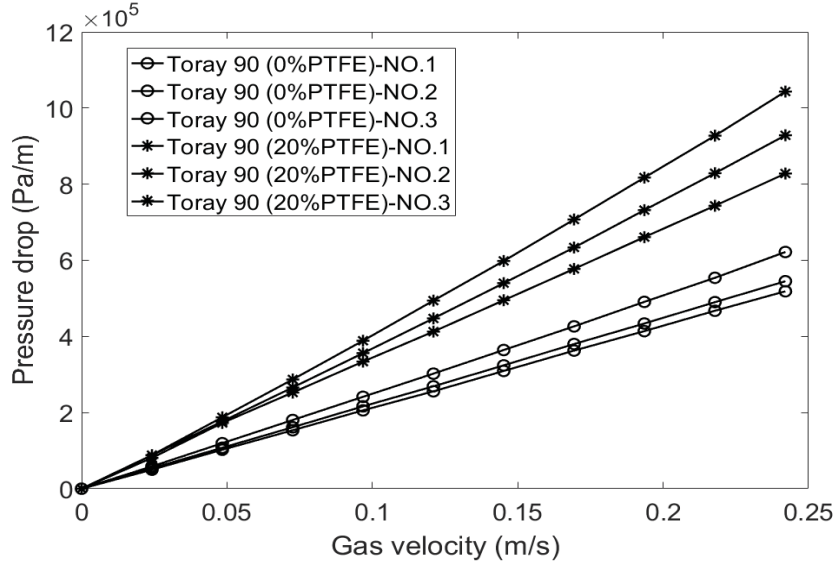


Figure 3.18: Pressure drop vs velocity for Toray-90 with 0%PTFE and 20%PTFE

Table 3.5: Toray-90 through-plane permeability

Sample	B_v ($10^{-11}m^2$)	Literature B_v ($10^{-11}m^2$)
Toray-90 (0% PTFE)	0.92 ± 0.07	1.1 [25], 0.9 [19], 0.8 [29]
Toray-90 (20% PTFE)	0.66 ± 0.08	0.73 [25], 0.66 [29]

3.5.1.2 Toray-90 GDL through-plane diffusivity and comparison with literature

To validate the reliability of the diffusivity measurement, the through-plane diffusivity of Toray-90 (0%PTFE) and Toray-90 (20%PTFE) are measured. Three replicates are measured for each type of sample and oxygen concentration vs pressure difference are shown in Figure 3.20. It can be seen that increasing the pressure difference can increase the oxygen transport through the sample. It was also found that 90 (0%PTFE) shows higher oxygen concentration than Toray-90 (20%PTFE). The through-plane diffusibility was found to decrease with increasing PTFE loading in GDL, which is consistent with the conclusion in the literature. The results are shown in Table 3.6 and compared with literature, and they found to be in good agreement.

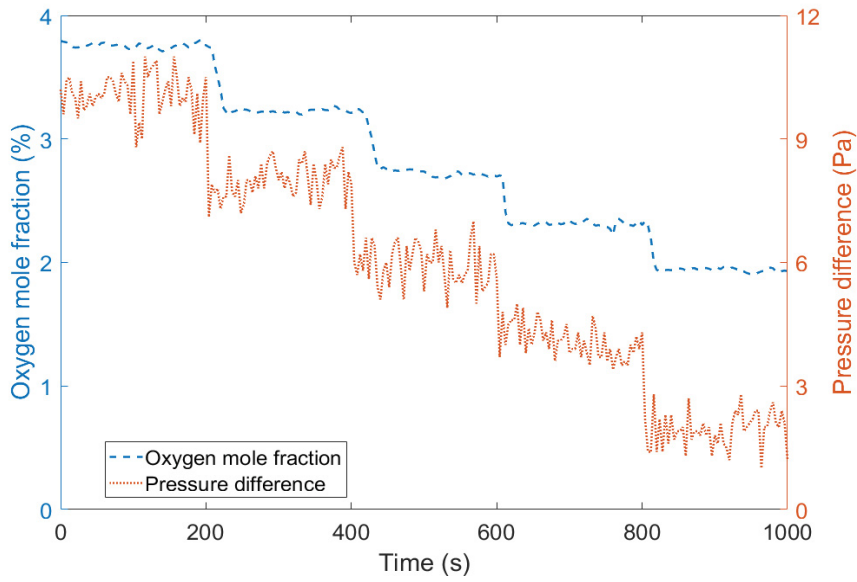


Figure 3.19: Differential pressure and oxygen concentration vs time for Toray-90 with 0%PTFE

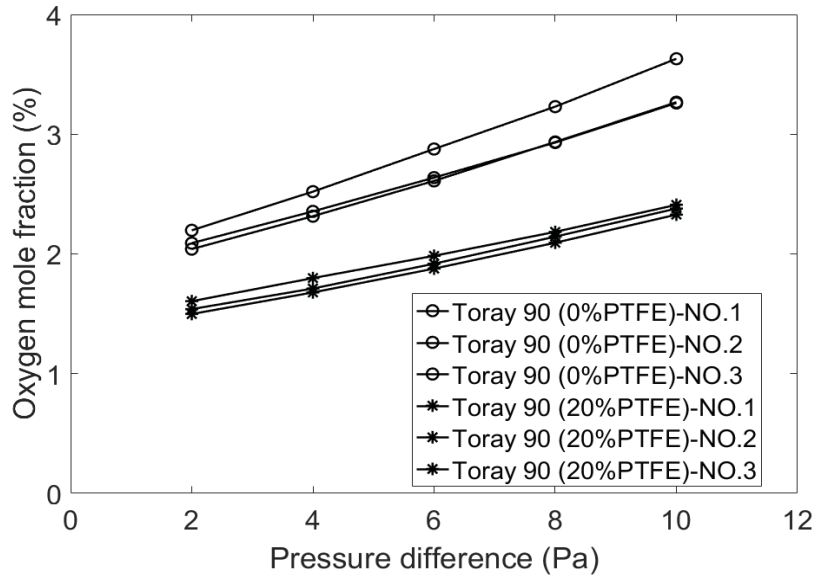


Figure 3.20: Oxygen concentration vs pressure drop for Toray-90 with 0%PTFE and 20%PTFE

Table 3.6: Toray-90 through-plane diffusibility

Sample	Diffusibility	Literature
Toray-90 (0%PTFE)	0.283 ± 0.014	0.24-0.34 [8], 0.25-0.33 [43], 0.27-0.42 [77], 0.237 ± 0.07 [29]
Toray-90 (20%PTFE)	0.204 ± 0.003	0.14-0.19 [8], 0.23-0.25 [43], 0.19-0.3 [77], 0.153 ± 0.03 [29]

The discussion above proves that the experimental setup was working properly and able to reproduce the results in the literature.

3.5.2 CL through-plane permeability

3.5.2.1 Measurements of pressure drop across the PTFE filter

As discussed before, to obtain the pressure drop across the CL, the PTFE filter needs to be measured prior to CL measurements. To get the pressure drop across PTFE filter, different gases with varying mean free path are used. Three replicates are tested and ΔP_{filter} vs. gas velocity were recorded and shown in Figure 3.21. The results showed good repeatability. The average pressure drop across the filter is used to estimate the pressure drop across the CL alone and calculate permeability. The pressure drop across the CL is calculated as:

$$\Delta P_{CL} = \Delta P_{total} - \Delta P_{filter} \quad (3.75)$$

where ΔP_{total} is the total pressure drop across the CL/filter sample and ΔP_{filter} is pressure drop across the filter.

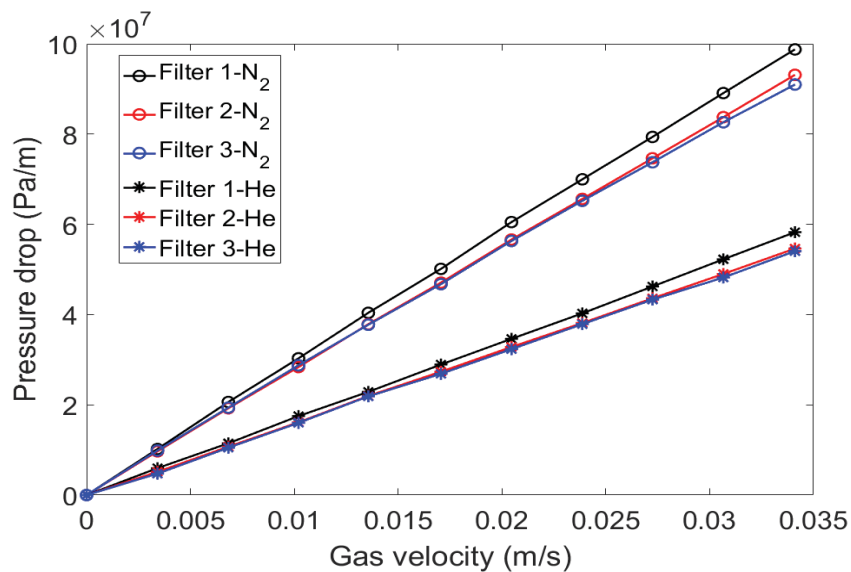


Figure 3.21: Filter pressure drop vs. gas velocity using nitrogen and helium

The permeability and effective pore diameter of the filter are also obtained using equation (3.12). Fitting results are shown in Figure 3.22. The effective pore diameter of the filter, d_p^{eff} is calculated as 122 ± 4 nm, which is in close agreement with the pore diameter reported by the filter supplier, i.e., 100 nm.

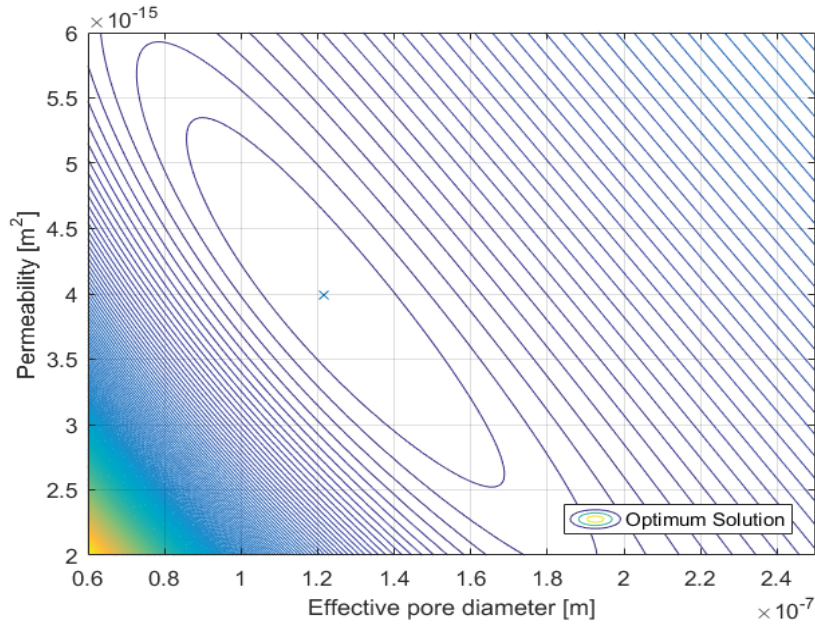


Figure 3.22: Fitting results for PTFE filter

3.5.2.2 CL permeability and effective pore diameter

As discussed before, Knudsen effects can be significant for PTFE filter and CLs because the pore sizes are very small and the gas flow is in the transition region. As a result, Darcy's law can not predict permeability of the PTFE filter and CL accurately. If no Knudsen slip occurs, the pressure loss across the sample would be independent on the gas type and as a result, the ratio of B_{v,N_2} to $B_{v,He}$ should be close or equal to 1. Table 3.7 shows the permeability of all CLs under study using nitrogen and helium as working gases. Pressure drop across the CL vs. gas velocity from the nitrogen and helium tests was calculated using equation (3.75) and shown in Figure 3.23 and 3.24. 20%Pt/C (40% Nafion) shows the highest pressure drop per meter. In contrast, 20%Pt/C (20% Nafion) and 46.7%Pt/C (30% Nafion) show the lowest pressure drop per meter. $B_{v,He}$ is 40% to 80% higher than B_{v,N_2} , indicating that Darcy's law can not be applied to CL and Knudsen slip should be taken into account. Equation (3.12) is therefore used to extract gas-independent viscous permeability and effective pore diameter.

Table 3.7: CL permeability using Darcy's law with nitrogen and helium

CL components	$B_{v,N_2} (10^{-16} \text{ m}^2)$	$B_{v,He} (10^{-16} \text{ m}^2)$	$B_{v,He}/B_{v,N_2}$
Vulcan 20%Pt/C, 20%Naf	8.6 ± 1.0	15.1 ± 2.0	1.76
Vulcan 20%Pt/C, 30%Naf	5.7 ± 0.5	8.6 ± 0.9	1.52
Vulcan 20%Pt/C, 40%Naf	2.1 ± 1.0	3.3 ± 1.4	1.62
Vulcan 40%Pt/C, 30%Naf	2.7 ± 0.16	3.9 ± 0.4	1.46
Ketjen 46.7%Pt/C, 30%Naf	15.0 ± 7.0	24.2 ± 11.9	1.61

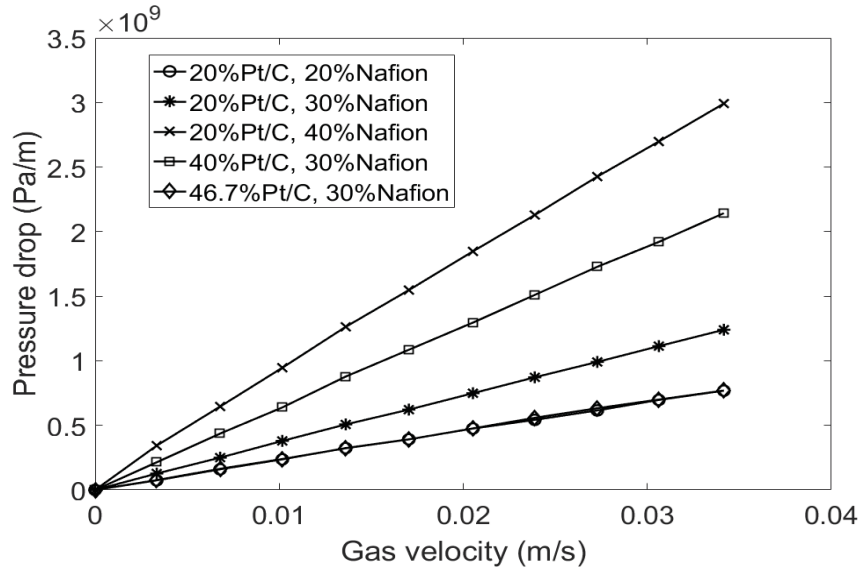


Figure 3.23: CL pressure drop vs. gas velocity using nitrogen

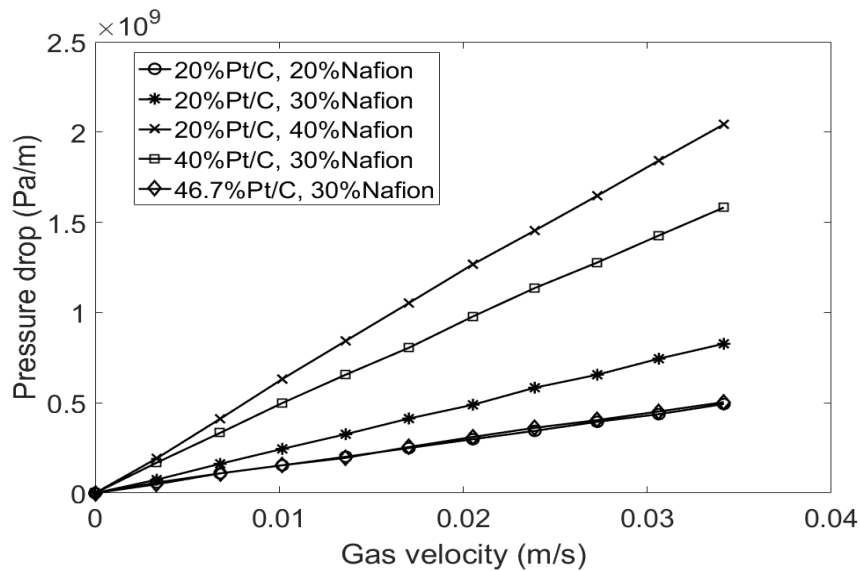


Figure 3.24: CL pressure drop vs. gas velocity using helium

As shown in Table 3.8, permeability and effective pore diameter decrease with increasing I/C ratio and Pt/C ratio. In addition, catalysts supported on Vulcan XC carbon black show lower permeability and smaller effective pore diameter than Ketjen carbon black at same I/C ratio. The effective pore diameter vs. porosity for CLs is plotted in Figure 3.25 and it can be seen that the effective pore diameter increases with increasing porosity because ionomer fills up or blocks some pores.

Table 3.8: Measured CL permeability and effective pore diameter

CL components	$B_v \times 10^{-16}$ (m ²)	d_p^{eff} (nm)
Vulcan 20%Pt/C, 20%Naf	5.6 ± 0.6	16.0 ± 4.0
Vulcan 20%Pt/C, 30%Naf	4.1 ± 0.5	7.0 ± 1.0
Vulcan 20%Pt/C, 40%Naf	2.6 ± 1.6	3.3 ± 0.6
Vulcan 40%Pt/C, 30%Naf	2.4 ± 0.3	3.5 ± 0.1
Ketjen 46.7%Pt/C, 30%Naf	7.7 ± 2.4	12.8 ± 1.2

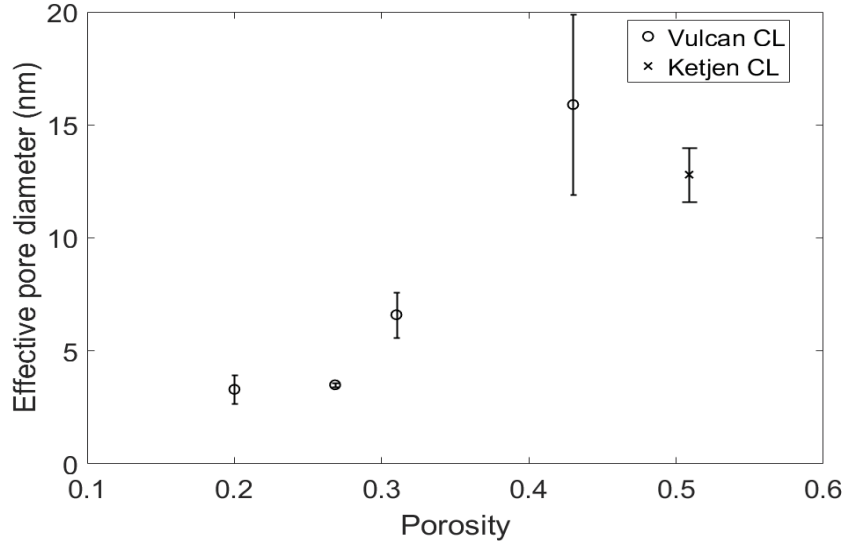


Figure 3.25: Effective pore diameter vs. CL porosity

3.5.2.3 Validation of Knudsen's expression using krypton and carbon dioxide

To validate the experimental results, the pressure drop vs. gas velocity is predicted for other gases using the effective pore diameter and gas-independent permeability shown in Table 3.8. Krypton and CO₂ are used for validation because they have different mean free path and viscosity than nitrogen and helium. The dynamic viscosity of krypton and CO₂ are taken as 2.5×10^{-5} Pa·s and 1.5×10^{-5} Pa·s at 25 °C [78].

Figure 3.26 compares pressure drop vs. gas velocity obtained experimentally and predicted using equations (2.3) with B_v obtained for He tests and (3.12) using data from Table 3.8. Equation (3.12) predictions for pressure drop vs. gas velocity are in good agreement with experimental data. In contrast, the compressible form of Darcy's law, equation (2.3), underestimates the pressure drop because Knudsen effect is ignored. Knudsen's expression is therefore able to provide a gas-independent and accurate prediction of gas transport in CLs.

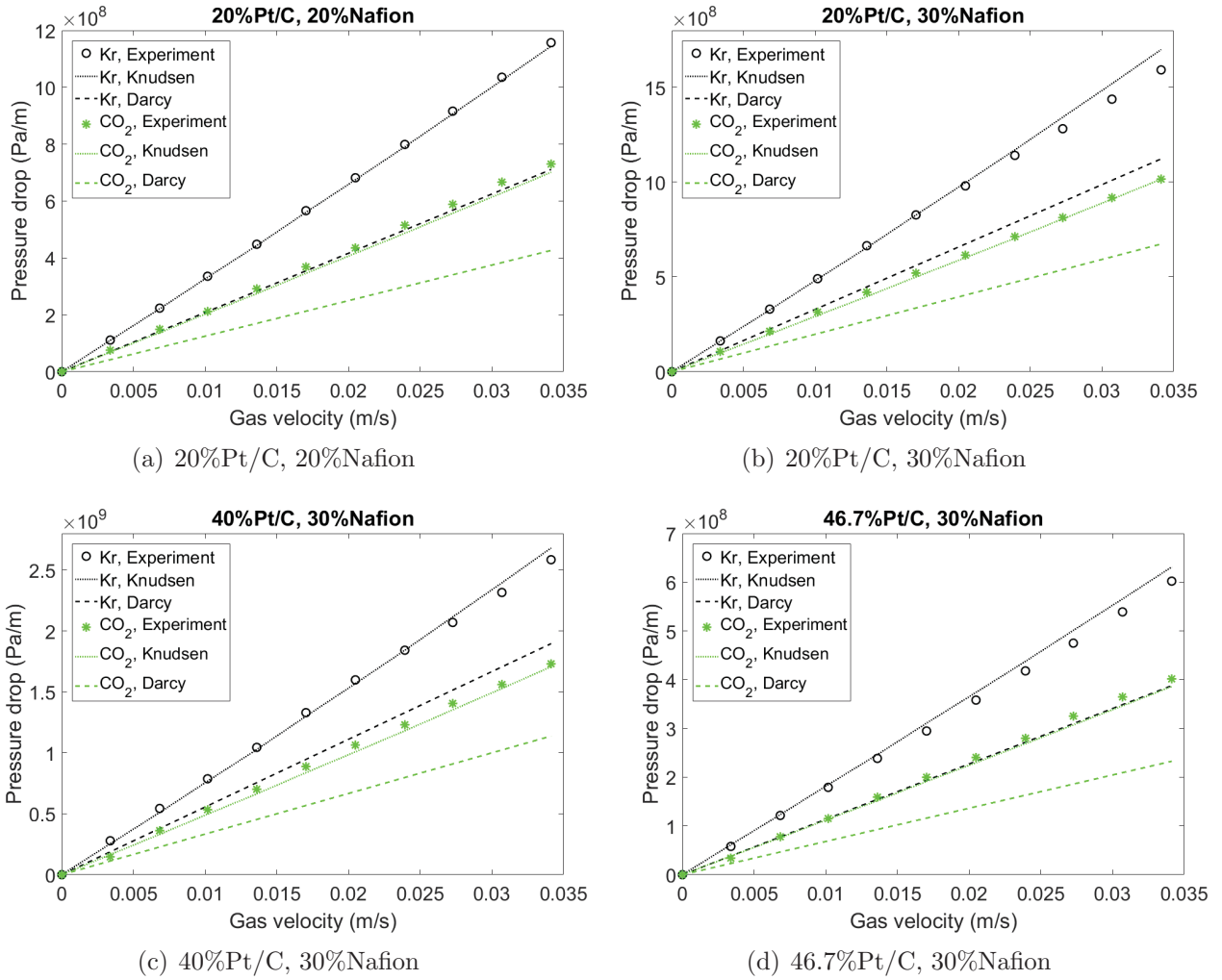


Figure 3.26: Comparison of experimental pressure drop vs. gas velocity using Krypton and CO₂ to estimated profiles using Knudsen's expression and Darcy's law for different catalyst: (a) 20%Pt/C, 20%Nafion (b) 20%Pt/C, 30%Nafion (c) 40%Pt/C, 30%Nafion (d) 46.7%Pt/C, 30%Nafion

3.5.3 CL through-plane diffusivity

3.5.3.1 Measurements of PTFE filter diffusivity

In order to obtain the through-plane diffusivity of the CL, the PTFE filter diffusivity is measured prior to CL measurements. To estimate PTFE filter effective diffusivity, oxygen and nitrogen are introduced into each flow channel of the diffusion bridge. The gas flow rates are kept at 1 SLPM to minimize the diffusive layer effect and maintain a measurable oxygen concentration in the nitrogen channel, i.e., a value between 1% and 5%. Three filter replicates are tested and diffusivity is estimated using equation (3.34). Table 3.9 shows the estimated effective diffusivity and diffusibility for 3 different filters. The P_x is $2.2 \times 10^{-8} \text{ m}^2/\text{s}$ and ratio of P_x/D_{filter}^{eff} is 1.9% so the results are highly repeatable. Here, Knudsen diffusivity is not separated from bulk diffusivity and \widehat{D}_{filter} is still calculated as D^{eff}/D_M .

Table 3.9: PTFE filter through-plane diffusibility

Sample	D_{filter}^{eff} (m^2/s)	\widehat{D}_{filter}
Filter 1	1.23×10^{-6}	0.0522
Filter 2	1.24×10^{-6}	0.0526
Filter 3	1.16×10^{-6}	0.0492

3.5.3.2 Measurements of PTFE filter diffusivity at different pressure

To verify the setup measurements, the filter is measured at different gauge pressure of 5, 10 and 15 psi. The molecular diffusivity at atmospheric pressure for $N_2 - O_2$ is taken as $2.2 \times 10^{-5} \text{ m}^2/\text{s}$ [65]. Results in Table 3.10 show the effective diffusivity and diffusibility for the filter at various absolute pressure. The deviation of results is very small, i.e., less than 2%. \widehat{D}_{filter} , defined as D_{filter}^{eff}/D_M , is found to increase with pressure from 0.0526 to 0.0560 by 7.0%. The increase is likely due to Knudsen effects. The effective molecular diffusivity, D_M^{eff} is extracted from equation (3.27) and D_M^{eff}/D_M is calculated and shown in Table 3.10. Compared to D_{filter}^{eff}/D_M which increases by 7%, D_M^{eff}/D_M increases by only 3.6%, which means Bosanquet equation can provide more accurate estimation for gas transport in CLs.

Table 3.10: PTFE filter through-plane diffusibility and effective diffusivity for different pressure

Pressure (psig)	D_{filter}^{eff} (m^2/s)	\widehat{D}_{filter} (D_{filter}^{eff}/D_M)	D_M^{eff}/D_M
5	0.846×10^{-6}	0.0526 ± 0.001	0.0560 ± 0.001
10	0.688×10^{-6}	0.0542 ± 0.002	0.0568 ± 0.001
15	0.590×10^{-6}	0.0560 ± 0.002	0.0580 ± 0.001

3.5.3.3 CL diffusivity measurements

To calculate CL diffusivity, nitrogen and oxygen are introduced into the bridge at 1 SLPM and oxygen concentration is measured. The effective diffusivity of CL/filter assembly is calculated and then CL effective diffusivity is calculated using equation (3.38). The oxygen concentrations in the nitrogen channel for different CL/filter assemblies are measured and shown in Figure 3.27. The X-axis represents porosity of the CL that is calculated in the previous section. Three replicates are measured for each type of CL/filter assembly and experimental raw data shows good repeatability.

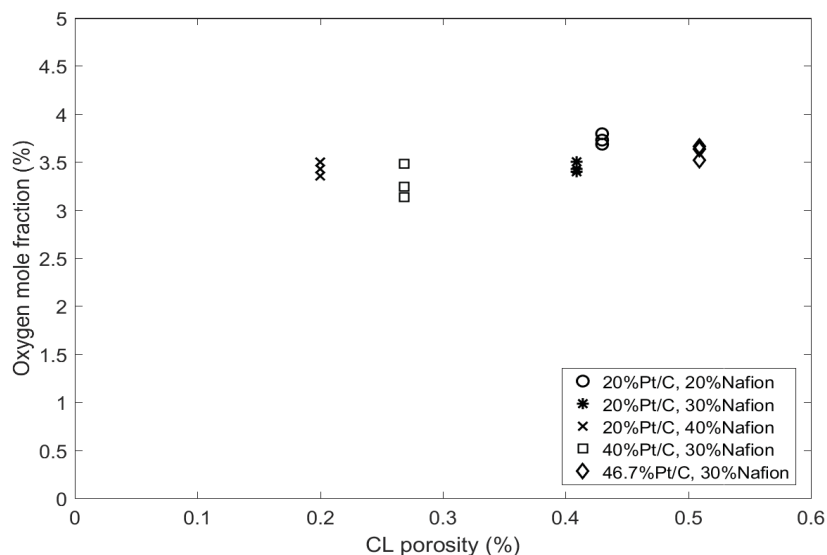


Figure 3.27: The oxygen concentrations in nitrogen channel for different CL/filter assembly

Table 3.11 shows the D_{CL}^{eff} and \widehat{D}_{CL} of the measured CL samples, where \widehat{D}_{CL} is calculated as the ratio of effective diffusivity to the molecular diffusivity. It is easy to see that the D_{CL}^{eff} and \widehat{D}_{CL} decrease with increasing I/C ratio. Meanwhile, Ketjen CL exhibits higher diffusion coefficient than Vulcan CL at same I/C ratio, which is attributed to its high porosity. This trend is in line with other literature [36, 46].

Table 3.11: CL diffusivity and diffusibility (Working gas: Nitrogen and Oxygen)

CL type	I/C ratio	D_{CL}^{eff} ($10^{-6}\text{m}^2/\text{s}$)	\widehat{D}_{CL}
Vulcan 20%Pt/C, 20%Naf	0.31	2.07 ± 0.54	0.090 ± 0.024
Vulcan 20%Pt/C, 30%Naf	0.54	0.65 ± 0.07	0.028 ± 0.003
Vulcan 20%Pt/C, 40%Naf	0.83	0.48 ± 0.09	0.021 ± 0.003
Vulcan 40%Pt/C, 30%Naf	0.71	0.36 ± 0.14	0.016 ± 0.006
Ketjen 46.7%Pt/C, 30%Naf	0.80	1.47 ± 0.11	0.063 ± 0.005

The CL effective diffusivity has been studied by some researchers [11, 36, 46]. Shen et al. [11] tested a CL made with 46.7%Pt/C (graphitized Ketjen) with 30% Nafion loading and calculated the effective diffusivity using Fick's second law at experimental condition 25°C and 1 atm. Inoue et al. [46] tested 50%Pt/C (Ketjen) with different I/C ratio ranging from 0.4 - 1.4 at 22°C and 2 atm using a setup with two flow channels. Yu et al. [36] measured CL of 50%Pt/C (Vulcan) with I/C ratio 0.5 to 1.5 using a PEM fuel cell platform. \widehat{D}_{CL} from literature is calculated based on their experimental raw data and shown in Table 3.13, Figure 3.28 and Figure 3.29. Compare the diffusivity results in terms of porosity (Figure 3.28), the experimental data are in line with literature data. The CL diffusivity shows an increasing trend with porosity. The CL diffusivity vs. porosity from experiment is similar with literature results regardless of the carbon support type. Comparing the results in terms of I/C ratio, however, the results do not agree. This is likely due to the different carbon support and different CL fabrication method. The CLs fabricated using inkjet printing have lower porosity than other fabrication methods. Also, the CLs supported on Ketjen black show higher diffusibility than the CLs supported on Vulcan black at same I/C ratio since Ketjen black CLs have higher porosity.

Table 3.13: CL diffusivity and diffusibility and comparison to literature results

	I/C	Porosity	\widehat{D}_{CL}
Inoue et al. [46], Ketjen	0.4	75%	0.320
Inoue et al. [46], Ketjen	0.7	71%	0.403
Inoue et al. [46], Ketjen	1	58%	0.119
Inoue et al. [46], Ketjen	1.3	41%	0.018
Yu et al. [36], Vulcan	0.5	50%	0.087
Yu et al. [36], Vulcan	1	41%	0.026
Yu et al. [36], Vulcan	1.5	18%	0.004
Vulcan 20%Pt/C, 20%Naf	0.31	43%	0.090
Vulcan 20%Pt/C, 30%Naf	0.54	31%	0.028
Vulcan 20%Pt/C, 40%Naf	0.83	20%	0.021
Vulcan 40%Pt/C, 30%Naf	0.71	27%	0.016
Ketjen 46.7%Pt/C, 30%Naf	0.8	51%	0.063

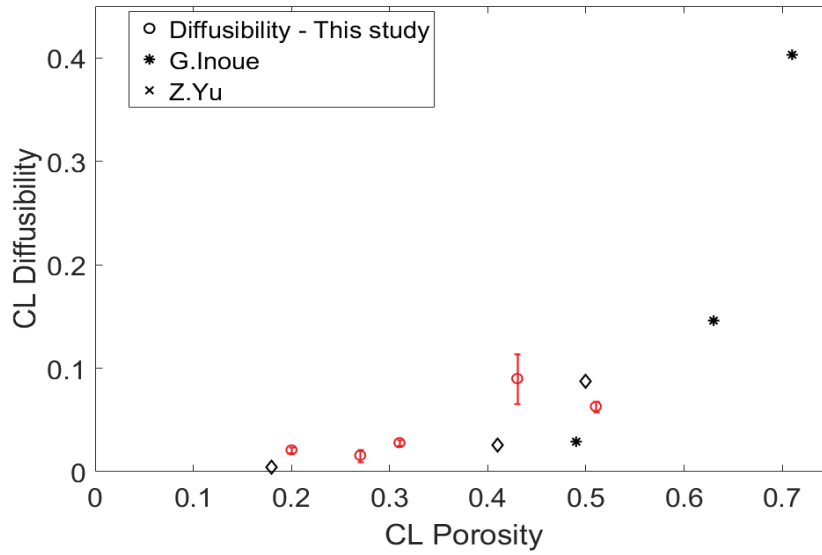


Figure 3.28: CL diffusibility vs porosity and comparison to literature results reported by Z. Yu [36] and G. Inoue [46]

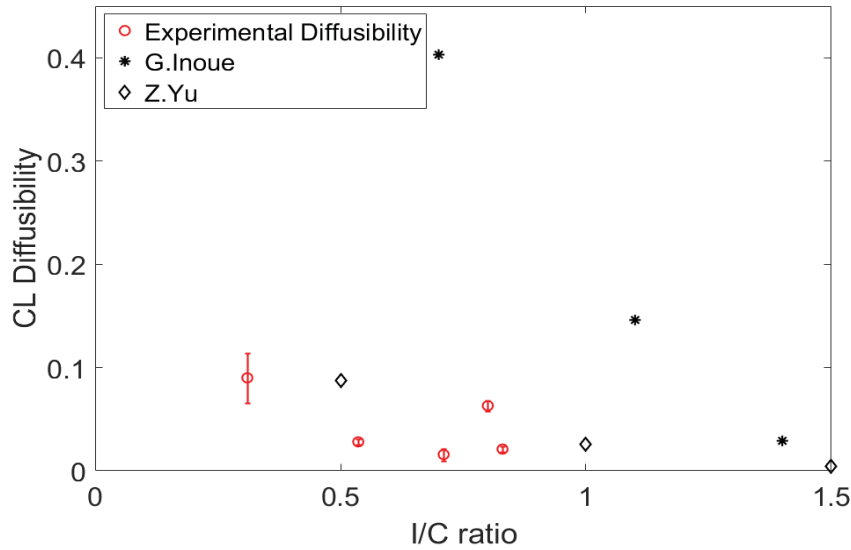


Figure 3.29: CL diffusibility vs I/C ratio and comparison to literature results reported by Z. Yu [36] and G. Inoue [46]

The equation (3.27) can be used to examine the contributions to gas transport resistance. The gas diffusion resistance come from molecular and Knudsen transport resistance and can be expressed as:

$$R_{gas} = R_M + R_K = \frac{L}{D_M^{eff}} + \frac{L}{D_K^{eff}} \quad (3.76)$$

where R_{gas} is the overall gas transport resistance, R_M and R_K are molecular and Knudsen transport resistance, respectively. The ratio of R_K to R_M is computed and shown in Table 3.13. The Knudsen transport resistance is 1 to 20 times higher than molecular transport resistance in the CLs, which indicates Knudsen transport resistance dominates the overall gas transport resistance in CLs.

Table 3.13: Knudsen transport resistance vs. molecular transport resistance

CL type	I/C ratio	R_K/R_M
Vulcan 20%Pt/C, 20%Naf	0.31	5.1 ± 1.0
Vulcan 20%Pt/C, 30%Naf	0.54	2.0 ± 0.2
Vulcan 20%Pt/C, 40%Naf	0.83	19.7 ± 1.7
Vulcan 40%Pt/C, 30%Naf	0.71	1 ± 0.2
Ketjen 46.7%Pt/C, 30%Naf	0.8	3.5 ± 1.81

3.6 Conclusions

A through-plane diffusion bridge is proposed to measure the transport properties of CLs, i.e., through-plane permeability, Knudsen diffusivity, effective pore diameter, and molecular diffusivity. To validate the setup accuracy, Toray-90 (0%PTFE) and Toray-90 (20%PTFE) are tested and experimental results are compared to literature. The CL samples, fabricated using inkjet printing, are printed on a PTFE filter. The effect of Nafion loading and I/C ratio on permeability and diffusivity are studied.

The gas-independent permeability and effective pore diameter are obtained by measuring the pressure drop across the CL sample. It was found that high Nafion loading or I/C ratio has a negative effect on permeability and effective pore diameter. Meanwhile, Ketjen carbon support has better transport properties than Vulcan carbon support. The experimental results are validated using Krypton and CO₂ and the Knudsen's expression can accurately predict the pressure drop using experimental permeability and effective pore diameter.

The CL diffusivity measurement uncertainty is analysed and it is found that choosing a better filter with appropriate pore diameter can reduce the uncertainty. The effective diffusivity of the CL is obtained by measuring oxygen mole fraction in nitrogen channel. Increasing Nafion loading or I/C ratio has a negative influence on CL diffusivity. Also, Ketjen carbon support shows higher diffusivity than Vulcan carbon support and this trend can also be found in the case of permeability. Experimental diffusivity is compared to literature data

and good agreement is found. The molecular transport resistance is compared to Knudsen transport resistance and it is found the majority of contribution to gas transport resistance is caused by Knudsen transport.

Chapter 4

Conclusion and future work

4.1 Conclusion

In the first chapter, a detailed literature review on transport properties of PEM fuel cell porous media identified two research gaps:

- even though many GDLs contain a large amount of carbon matrix material, few studies have analyzed the effect of gas diffusion layer carbon matrix on its transport properties, such as permeability and diffusivity
- CL transport properties, especially permeability and Knudsen diffusivity, have not been well studied.

The second chapter addresses the first literature gap by measuring the in-plane transport properties of GDLs with different amount of carbon matrix. The experimental setup developed by Mangal [28] was enhanced to accurately measure in-plane permeability and diffusivity of GDLs. Improvements in the setup included: (1) removing BPC and DPC, and (2) using more number of layers to get better oxygen signal. MIP technique is employed to obtain the PSD and carbon matrix of GDLs. SEM imaging is also used for better observing the GDL pore structure. It was found that expression used to estimate permeability for fibrous media are not appropriate for materials with large amount of carbon matrix. The Knudsen slip effect is also more significant in GDLs with large amount of carbon matrix, such as 24 BA and 28 BA. The samples with largest pore diameter and low amount of carbon matrix, i.e., 29 BA, had higher diffusibility at same porosity/compression level than other samples. Freudenberg also showed very high diffusibility, which may be attributed to its unique pore structure and zero carbon matrix.

Chapter 3 studies through plane mass transport in CLs. In order to study the effect of CL structure on transport properties, CL with different porosity, i.e., I/C ratio, and type of carbon support were fabricated and studied. The through-plane diffusion bridge developed by Mangal [27] is modified to measure the transport properties of CLs by: (1) removing BPC and DPC, (2) replacing the lamination sheet with transparent tapes to avoid compressing CLs. Knudsen's expression is used to calculate permeability and effective pore diameter of the CL. The model is validated by measuring pressure drop vs gas velocity for different gases. The effective diffusivity is calculated using Fick's law. It was found that increasing I/C ratio had a negative effect on CL transport properties. In addition, Ketjen carbon support shows better transport properties than Vulcan carbon support due to the higher porosity of the former.

4.2 Future work

In this study, the GDLs were measured in the in-plane direction at compression level 0% to 50% and Knudsen effects are found in 24 BA and 28 BA. However, this work can be further extended by increasing the compression level to 70% to 80% to obtain more data in the region where Knudsen effects are more dominant. A better relation between diffusibility and porosity would also be obtained as GDL transport properties would be measured over a wider range of porosities.

The CL diffusivity measurement uncertainty is higher than expected due to the filter selection, so the accuracy can be improved by looking for a better filter with appropriate pre diameter. Even though Vulcan type CL with different Nafion loading is measured in this study, Ketjen CL is measured with only one Nafion loading. As Ketjen shows better transport properties than Vulcan, it would be beneficial to study Ketjen CL with different Nafion loading to confirm our conclusion that the use of Ketjen carbon black leads to layers with better porosity and morphology.

CL transport properties have been measured in the through-plane direction because of its thin thickness. Hence, the current setup can be modified to measure CL in the in-plane direction. This could be achieved by printing CL on an impermeable material and placing the sample into the in-plane diffusion bridge. A new in-plane diffusion bridge needs to be made with very high precision.

All the measurement in this study are done in dry condition, however, the PEM fuel cell

media always works in humid conditions. The setup can be modified to saturate the gases using a water bath to measure transport properties at different humidities.

Bibliography

- [1] World energy outlook 2017. <https://www.iea.org/weo2017/#section-1-1>. Accessed: 2018-06-20.
- [2] The hidden costs of fossil fuels. <https://www.ucsusa.org/clean-energy/coal-and-other-fossil-fuels/hidden-cost-of-fossils>, note = Accessed: 2018-06-20,.
- [3] H.Tawfik, Y.Hung, and D.Mahajan. Metal bipolar plates for pem fuel cell-a review. *Journal of Power Sources*, 163(2):755–767, 2007.
- [4] J.P. Feser, A.K. Prasad, and S.G. Advani. Experimental characterization of in-plane permeability of gas diffusion layers. *Journal of Power Sources*, 162(2):1226–1231, 2006.
- [5] Sigracet fuel cell components. <https://www.sglcarbon.com/en/markets-solutions/material/sigracet-fuel-cell-components/>. Accessed: 2019-03-8.
- [6] Sehkyu Park, Jong-Won Lee, and Branko N. Popov. A review of gas diffusion layer in pem fuel cells: Materials and designs. *International Journal of Hydrogen Energy*, 7(1):5850–5865, 2012.
- [7] Sumit Kundu, Kunal Karan, Michael Fowler, Leonardo C. Simon, Brant Peppley, and Ela Halliop. Influence of micro-porous layer and operating conditions on the fluoride release rate and degradation of pemfc membrane electrode assemblies. *Journal of Power Sources*, 179(2):693–699, 2008.
- [8] Carl Chan, Nada Zamel, Xianguo Li, and Jun Shen. Experimental measurement of effective diffusion coefficient of gas diffusion layer/microporous layer in pem fuel cells. *Electrochimica Acta*, 65:13–21, 2012.
- [9] Jin Hyun Nam, Kyu-Jin Lee, Gi-Suk Hwang, Charn-Jung Kim, and Massoud Kaviany. Microporous layer for water morphology control in pemfc. *International Journal of Heat and Mass Transfer*, 52(11-12):2779–2791, 2009.
- [10] James Larminie and Andrew Dicks. *Fuel Cell Systems Explained*. John Wiley & Sons, 2nd edition, 2003.
- [11] Jun Shen, Jianqin Zhou, Nelson G.C. Astrath, Titichai Navessin, Zhong-Sheng (Simon) Liu, Chao Li, Jurandir H. Rohling, Dmitri Bessarabov, Shanna Knights, and Siyu Ye.

- Measurement of effective gas diffusion coefficients of catalyst layers of pem fuel cells with a loschmidt diffusion cell. *Journal of Power Sources*, 196(2):674–678, 2011.
- [12] Li Chen, Gang Wu, Edward F Holby, Piotr Zelenay, Wen-Quan Tao, and Qinjun Kang. Lattice boltzmann pore-scale investigation of coupled physical-electrochemical processes in c/pt and non-precious metal cathode catalyst layers in proton exchange membrane fuel cells. *Electrochimica Acta*, 158:175–186, 2015.
- [13] H.A. Gasteiger, J.E. Panels, and S.G. Yan. Dependence of pem fuel cell performance on catalyst loading. *Journal of Power Sources*, 127(1-2):162–171, 2004.
- [14] F. Jaouen, E. Proietti, M. Lefevre, R. Chenitz, J.-P. Dodelet, G. Wu, H.T. Chung, C. M. Johnston, and P. Zelenay. Recent advances in non-precious metal catalysis for oxygen-reduction reaction in polymer electrolyte fuel cells. *Energy Environ. Sci*, 4(4):114–130, 2011.
- [15] D.C.Higgins and Z.Chen. Recent progress in non-precious metal catalysts for pem fuel cell applications. *The Canadian Journal of Chemical Engineering*, 91(12):1881–1895, 2013.
- [16] Je Seung Lee, Nguyen Dinh Quan, Jung Min Hwang, Sang Deuk Lee, Honggon Kim, Hyunjoo Lee, and Hoon Sik Kim. Polymer electrolyte membranes for fuel cells. *J. Ind. Eng. Chem*, 12(2):175–183, 2006.
- [17] Nafion hp membrane properties. <http://www.fuelcellstore.com/spec-sheets/nafion-hp-membrane-spec-sheet.pdf>, note = Accessed: 2018-06-20,.
- [18] Nafion 115, 117, and 1110 membrane properties sheet. <http://www.fuelcellstore.com/spec-sheets/chemours-nafion-115-117-1110-spec-sheet.pdf>, note = Accessed: 2018-06-20,.
- [19] Jeff T.Gostick, Michael W.Fowler, Mark D.Pritzker, Marios A.Ioannidis, and Leya M.Behra. In-plane and through-plane gas permeability of carbon fibre electrode backing layers. *Journal of Power Sources*, 162(1):228–238, 2006.
- [20] M.S.Ismail, T.Damjanovic, D.B.Ingham, L.Ma, and M.Pourkashanian. Effect of polytetrafluoroethylene-treatment and microporous layer-coating on the in-plane permeability of gas diffusion layers used in proton exchange membrane fuel cells. *Journal of Power Sources*, 195(19):6619–6628, 2010.
- [21] Mohammed Ismail, Kevin Hughes, Derek Ingham, Lin Ma, Mohamed Pourkashanian, and Masli Rosli. Through-plane permeability for untreated and ptfe-treated gas diffusion layers in proton exchange membrane fuel cells. In *Seventh International Fuel Cell Science, Engineering and Technology Conference*, Newport Beach, California, 2009.
- [22] O.M. Orogbemi, D.B. Ingham, M.S. Ismail, K.J Hughes, and M.Pourkashanian L.Ma. Through-plane gas permeability of gas diffusion layers and microporous layer: Effects of carbon loading and sintering. *Journal of the Energy Institute*, 91(2):270–278, 2018.

- [23] Vladimir Gurau, Michael J. Bluemle, Emory S. De Castro, Yu-Min Tsou, Thomas A. Zawodzinski Jr, and J. Adin Mann Jr. Characterization of transport properties in gas diffusion layers for proton exchange membrane fuel cells: 2. absolute permeability. *Journal of Power Sources*, 165(2):793–802, 2007.
- [24] A. Tamayol, F. McGregor, and M. Bahrami. Single phase through-plane permeability of carbon paper gas diffusion layers. *Journal of Power Sources*, 204:94–99, 2012.
- [25] Nicholas B. Carrigy, Lalit M. Pant, Sushanta Mitra, and Marc Secanell. Knudsen diffusivity and permeability of pemfc microporous coated gas diffusion layers for different polytetrafluoroethylene loadings. *Journal of The Electrochemical Society*, 160(2):F81–F89, 2013.
- [26] Lalit M. Pant, Sushanta K. Mitra, and Marc Secanell. Absolute permeability and knudsen diffusivity measurements in pemfc gas diffusion layers and micro porous layers. *Journal of Power Sources*, 206:153–160, 2012.
- [27] Prafful Mangal, Lalit M. Pant, Nicholas Carrigy, Mark Dumontier, Valentin Zingan, Sushanta Mitra, and Marc Secanell. Experimental study of mass transport in pemfcs: Through plane permeability and molecular diffusivity in gdl. *Electrochimica Acta*, 167:160–171, 2015.
- [28] P. Mangal, M. Dumontier, N. Carrigy, and M. Secanell. Measurements of permeability and effective in-plane gas diffusivity of gas diffusion media under compression. *ECS Transactions*, 64(3):487–499, 2014.
- [29] Prafful Mangal. Experimental study of mass transport parameters of pemfc porous media, 2014.
- [30] M. Kaviany. *Principles of heat transfer in porous media*. Springer, 1st edition, 1991.
- [31] M.M. Tomadakis and T.J. Robertson. Viscous permeability of random fiber structures: Comparison of electrical and diffusional estimates with experimental and analytical results. *Journal of Composite Materials*, 39(2):163–188, 2005.
- [32] L. Hao and P. Cheng. Lattice boltzmann simulations of anisotropic permeabilities in carbon paper gas diffusion layers. *Journal of Power Sources*, 186(1):104–114, 2009.
- [33] B. Yu and J. Li. Some fractal characters of porous media. *Fractals*, 9(3):365–372, 2001.
- [34] Guangli He, Zongchang Zhao, Pingwen Ming, Abudula Abuliti, and Caoyong Yin. A fractal model for predicting permeability and liquid water relative permeability in the gas diffusion layer (gdl) of pemfcs. *Journal of Power Sources*, 163(2):846–852, 2007.
- [35] Dahua Shou, Youhong Tang, Lin Ye, Jintu Fan, and Feng Ding. Effective permeability of gas diffusion layer in proton exchange membrane fuel cells. *International Journal of Hydrogen Energy*, 38(25):10519–10526, 2013.

- [36] Z.Yu, R.N.Carter, and J.Zhang. Measurements of pore size distribution, porosity, effective oxygen diffusivity, and tortuosity of pem fuel cell electrodes. *Fuel Cells*, 12(4):557–565, 2012.
- [37] T. R. Marrero and E. A. Mason. Gaseous diffusion coefficients. *Journal of Physical and Chemical Reference Data*, 1(1):3–118, 1972.
- [38] Parker C. Reist. Steady-state measurement of krypton-85-air diffusion coefficients in porous media. *Environmental Science and Technology*, 1(7):566–569, 1967.
- [39] Bendt P. J. “Measurements of He³-He⁴ and H₂-D₂ Gas Diffusion Coefficients”. *Physical Review*, 110(1):85–89, 1958.
- [40] Michael J. Martinez, Sirivatch Shimpalee, and J. W. Van Zee. Measurement of macmullin numbers for pemfc gas-diffusion media. *Journal of The Electrochemical Society*, 156(1):B80–B85, 2009.
- [41] Denis Kramer, Stefan A.Freunberger, Reto Fluckiger, Ingo A.Schneider, Alexander Wokaun, Felix N.Buchi, and Gunther G.Scherer. Electrochemical diffusimetry of fuel cell gas diffusion layers. *Journal of Electroanalytical Chemistry*, 612(1):63–77, 2008.
- [42] Reto Fluckiger, Stefan A.Freunberger, Denis Kramer, Alexander Wokaun, Gunther G.Scherer, and Felix N.Buchi. Anisotropic, effective diffusivity of porous gas diffusion layer materials for pefc. *Electrochimica Acta*, 54(2):551–559, 2008.
- [43] Nada Zamel, Nelson G.C. Astrath, Xianguo Li, Jun Shen, Jianqin Zhou, Francine B.G. Astrath, Haijiang Wang, and Zhong-Sheng Liu. Experimental measurements of effective diffusion coefficient of oxygen-nitrogen mixture in pem fuel cell diffusion media. *Chemical Engineering Science*, 65(2):931–937, 2010.
- [44] Grant Unsworth, Lu Dong, , and Xianguo Li. Improved experimental method for measuring gas diffusivity through thin porous media. *AIChE J*, 59(4):1409–1419, 2013.
- [45] Rinat R. Rashapov and Jeff T. Gostick. In-plane effective diffusivity in pemfc gas diffusion layers. *Transport in Porous Media*, 115(3):228–238, 2016.
- [46] Gen Inoue, Kouji Yokoyama, Junpei Ooyama, Takeshi Terao, Tomomi Tokunaga, Norio Kubo, and Motoaki Kawase. Theoretical examination of effective oxygen diffusion coefficient and electrical conductivity of polymer electrolyte fuel cell porous components. *Journal of Power Sources*, 327:610–621, 2016.
- [47] Zhiqiang Yu and Robert N. Carter. Measurements of effective oxygen diffusivity in electrodes for proton exchange membrane fuel cells. *Journal of Power Sources*, 195(4):1079–1084, 2010.
- [48] Jian Zhao, Samaneh Shahgaldi, Lbrahim Alaefour, Qian Xu, and Xianguo Li. Gas permeability of catalyzed electrodes in polymer electrolyte membrane fuel cells. *Applied Energy*, 209:203–210, 2018.

- [49] Bruggeman D. Calculation of various physics constants in heterogenous substances I dielectricity constants and conductivity of mixed bodies from isotropic substances. *Annalen der Physik*, 24(7):636–664, 1935.
- [50] Tomadakis M. M and Sotirchos S. V. Ordinary and transition regime diffusion in random fibre structures. *AIChE Journal*, 39(3):397–412, 1993.
- [51] Prodip K. Das, Xianguo Li, and Zhong-Sheng Liu. Effective transport coefficients in pem fuel cell catalyst and gas diffusion layers: Beyond bruggeman approximation. *Applied Energy*, 87(9):2785–2796, 2010.
- [52] Jin Hyun Nam and Massoud Kaviany. Effective diffusivity and water-saturation distribution in single- and two-layer pemfc diffusion medium. *International Journal of Heat and Mass Transfer*, 46(24):4595–4611, 2003.
- [53] Zhang XM and Zhang XX. Impact of compression on effective thermal conductivity and diffusion coefficient of woven gas diffusion layers in polymer electrolyte fuel cells. *Fuel Cells*, 14(2):303–311, 2014.
- [54] Nada Zamel, Xianguo Li, Jurgen Becker, and Andreas Wiegmann. Effect of liquid water on transport properties of the gas diffusion layer of polymer electrolyte membrane fuel cells. *International journal of hydrogen energy*, 36(9):5466–5478, 2011.
- [55] T.G.Tranter, P. Stogornyuk, J.T. Gostick, A.D. Burns, and W.F.Gale. A method for measuring relative in-plane diffusivity of thin and partially saturated porous media: An application to fuel cell gas diffusion layers. *International Journal of Heat and Mass Transfer*, 110:132–141, 2017.
- [56] Tero Hottinen, Olli Himanen, Suvi Karvonen, and Iwao Nitta. Inhomogeneous compression of pemfc gas diffusion layer part ii. modeling the effect. *Journal of Power Sources*, 171(1):113–121, 2007.
- [57] I. Nitta, S. Karvonen, O. Himanen, and M. Mikkola. Modelling the effect of inhomogeneous compression of gdl on local transport phenomena in a pem fuel cell. *Fuel Cells*, 8(6):410–421, 2008.
- [58] John R. Fanchi. *Shared Earth Modeling: Methodologies for Integrated Reservoir Simulations*. Gulf Professional Publishing, 1st edition, 2002.
- [59] R. Byron Bird, Warren E. Stewart, and Edwin N. Lightfoot. *Transport phenomena*. John Wiley & Sons, 2nd edition, 2002.
- [60] John R. Taylor. *An Introduction to Error Analysis: The Study of Uncertainties in Physical Measurements*. University Science Books, 2nd edition, 1997.
- [61] James Richard Kracher. Experimental analysis of transient water fluxes in pem fuel cells, 2018.

- [62] Anthony J. Wheeler and Ahmad R. Ganji. *Introduction to Engineering Experimentation*. Prentice Hall, 3rd edition, 2009.
- [63] Anthony D. Santamaria, Prodip K. Das, James C. MacDonald, , and Adam Z. Weber. Liquid-water interactions with gas-diffusion-layer surfaces. *Journal of The Electrochemical Society*, 161(12):F1184–F1193, 2014.
- [64] Joseph D. Fairweather, Perry Cheung, and Daniel T. Schwartz. The effects of wet-proofing on the capillary properties of proton exchange membrane fuel cell gas diffusion layers. *Journal of Power Sources*, 195(3):787–793, 2010.
- [65] Calculating the oxygen diffusion coefficient in air. <http://compost.css.cornell.edu/oxygen/oxygen.diff.air.html>. Accessed: 2019-03-05.
- [66] S. P. Wasik and K. E. McCulloh. Measurements of gaseous diffusion coefficients by a gas chromatographic technique. *JOURNAL OF RESEARCH of the National Bureau of Standards-A. Physics and Chemistry*, 73A(2):207–211, 1969.
- [67] S. Whitaker. *Transport in Porous Media 1(1) 3-25*. 1986.
- [68] M. Mandal, A. Valls, N. Gangnus, and M. Secanell. Analysis of inkjet printed polymer electrolyte electrolyzer electrodes. *ECS Transactions*, 80(8):1085–1095, 2017.
- [69] S. Shukla, D. Stanier, M. S. Saha, J. Stumper, and M. Secanell. Analysis of inkjet printed pefc electrodes with varying platinum loading. *Journal of The Electrochemical Society*, 163(7):F677–F687, 2016.
- [70] S. Shukla, K. Domican, K. Karan, S. Bhattacharjee, and M. Secanell. Analysis of low platinum loading thin polymer electrolyte fuel cell electrodes prepared by inkjet printing. *Electrochimica Acta*, 156:289–300, 2015.
- [71] P.J. Ferreira, G.J.O La, Y. Shao-Horn, D. Morgan, R. Makharia, S. Kocha, and H. A. Gasteiger. Instability of pt/c electrocatalysts in proton exchange membrane fuel cells a mechanistic investigation. *Journal of The Electrochemical Society*, 152(11):A2256–A2271, 2005.
- [72] S. Shukla, D. Stanier, MS. Saha, B. Zahiri, M. Tam, J. Stumper, and M. Secanell. Characterization of inkjet printed electrodes with improved porosity. *ECS Transactions*, 77(11):1453–1463, 2017.
- [73] R. E. Cunningham and R. J. J. Williams. *Diffusion in Gases and Porous Media*. Plenum Press, 1980.
- [74] H Adzumi. Studies on the flow of gaseous mixtures through capillaries. iii. the flow of gaseous mixtures at medium pressures. *Bulletin of the Chemical Society of Japan*, 12(6):292–303, 1937.
- [75] H Adzumi. The flow of gases through metallic capillaries at low pressures. *Bulletin of the Chemical Society of Japan*, 14(9):343–347, 1939.

- [76] Piet J.A.M. Kerkhof. A modified maxwell-stefan model for transport through inert membranes: the binary friction model. *The Chemical Engineering Journal*, 64(3):319–343, 1996.
- [77] Jacob M.LaManna and Satish G.Kandlikar. Determination of effective water vapor diffusion coefficient in pemfc gas diffusion layers. *INTERNATIONAL JOURNAL OF HYDROGEN ENERGY*, 36(8):5021–5029, 2011.
- [78] Tables of physical and chemical constants. http://www.kayelaby.npl.co.uk/general_physics/2_2/2_2_3.html. Accessed: 2019-02-11.

Appendix A

GDL through-plane diffusivity analysis software

```
1 % This is the main.m file used to estimate D_eff
2 %
3 % This file reads experimental data for differential pressure (from DPC)
4 % and mole fraction (from Neofex sensor), reads the equations (from
5 % MODEL.ODEfun.m), boundary conditions (from MODEL.bcfun.m), and estimate
6 % the D_eff for a pair of gases
7 %
8 % Input parameters: Differential pressure , oxygen mole fraction
9 % -
10 %
11 % Please update the differential pressure and oxygen mole fraction data
12 % from experiments in the matrices 'delta_p' and 'x_O2', respectively.
13 %
14 % Please make sure to update the parameters in the file 'load_constants '
15 %
16 % Parameters that generally need update are viscous permeability , thickness
17 % of the sample. Other parameters might be changed like flow rate , D_bulk
18 % etc , depending on the experiments
19 %%%%%%%%%%%%%%%%%%%%%%%%%%%%%%%%%%%%%%%%%%%%%%%%%%%%%%%%%%%%%%%%%%%%%%%%%%
20
21 function main
22
23 clear
24 close all
25
26 [D_bulk , dia , t , w , L , R , T , M_O2 , M_N2 , eta_O2 , eta_N2 , B_v , zeta_O2N2 ,
27 zeta_N2O2 , zeta_O2O2 , zeta_N2N2 , p_N2_r , rho_o , vv , rho_O2]=load_constants ();
28 eta_mix = eta_O2*0.8 + eta_N2*0.2;
29 %eta_mix = eta_O2*0.5 + eta_N2*0.5;
30 GDL.L=L;
31
32
33 %%%%%%%%%%%%%%%%%%%%%%%%%%%%%%%%%%%%%%%%%%%%%%%%%%%%%%%%%%%%%%%%%%%%%%%%%%
34 %%%%%%%%%%% experimental data %%%%%%%%%%%
35 %%%%%%%%%%%%%%%%%%%%%%%%%%%%%%%%%%%%%%%%%%%%%%%%%%%%%%%%%%%%%%%%%%%%%%%%%%
36 %%%%%%%%%%%%%%%%%%%%%%%%%%%%%%%%%%%%%%%%%%%%%%%%%%%%%%%%%%%%%%%%%%%%%%%%%%
```

```

37 delta_p=[          % Differential pressure Pa(measured from DPC)
38 10
39 8
40 6
41 4
42 2
43 ];
44
45
46 x_O2=0.01*[          % Oxygen mole fraction (measured from Neofox sensor)
47 3.31426596
48 2.88893959
49 2.48698791
50 2.13536631
51 1.78179271
52
53 ];
54
55
56 p_O2_l = p_N2_r + delta_p;          % Oxygen's absolute pressure Pa
57
58 % CHANGE area formula
59 A=3.14*dia^2/4;% Area of the porous media(Only for T-plane exps)m2
60 %A=t*w;% Area of the porous media (Only for In-plane)
61
62 rho_N2=rho_o*(p_N2_r(1,1)/101000); %N2 density at back pressure p_N2_r(1,1)
63 rho_OO=1.429*(p_N2_r(1,1)/101000);%O2 density at back pressure p_N2_r(1,1)
64 m=rho_N2*vv*1e-3/60;%Mass flow rate in nitrogen channel estimated (in kg/s)
65          % vv is Flow rate of gases in LPM
66
67 tx_n=size(x_O2); %tx_n=5
68 n=max(tx_n); % n=5
69 n_O2_exp=zeros(n,1); %n=5
70 mol_extra=zeros(n,1);%n=5
71 v=zeros(n,1);%n=5
72
73 %%%%%%%%%%%%%%%%%%%%%%%%%%%%%%%%%%%%%%%%%%%%%%%%%%%%%%%%%%%%%%%%%%%%%%%%%
74 %%%%%%%%%%%%%%%%%%%%%%%%%%%%%%%%%%%%%%%%%%%%%%%%%%%%%%%%%%%%%%%%%%%%%%%%%
75 %%% Estimating experimental oxygen mass flux %%%%%%%%%%%%%%%%%%%%%%%%%%%%%%%%%%%%%%%%%%%%%%%%%%%%%%%%%%%%%%%%%%%%%%%%%
76 %%%%%%%%%%%%%%%%%%%%%%%%%%%%%%%%%%%%%%%%%%%%%%%%%%%%%%%%%%%%%%%%%%%%%%%%%
77 %%%%%%%%%%%%%%%%%%%%%%%%%%%%%%%%%%%%%%%%%%%%%%%%%%%%%%%%%%%%%%%%%%%%%%%%%
78
79 D_ij_vec = 1.3e-7:1.5e-7:1.2e-5;
80 % Modify the range of D_eff here, close to the expected values
81
82     tmp1=size(p_O2_l); %tmp1=5
83     tmp2=size(D_ij_vec);
84     N_1=max(tmp1);%N_1=5
85     N_2 = max(tmp2);
86     n_O2 = zeros(N_1,N_2);
87     res=zeros(N_1,N_2);
88     Res = zeros(N_2,1);
89
90

```

```

91 for i = 1:length(D_ij_vec)
92
93     D_ij = D_ij_vec(i);
94
95     for j=1:N_1
96         p_O2_l_array=p_O2_l(j,1);
97         x_O2_array=x_O2(j,1);
98         v(j,1)=B_v/eta_mix*(delta_p(j,1)/GDL.L);
99         %gas velocity across media, obtained by B_v experiment
100     mol_extra(j,1) = p_O2_l(j,1)/(R*T)*A*v(j,1); %molar flux across media
101     mol = m/M_N2; %molar flux in nitrogen channel
102     n_O2_exp(j,1)=(x_O2(j,1)*(mol+mol_extra(j,1))/A)*M_O2;
103     %oxygen mass flux across media
104
105     % Initial mesh -
106     L1 = 0;
107     L2 = GDL.L; % sample thickness
108     n_GDL = 1e3; %number of points in the initial mesh,
109
110     xinit = L1:(L2-L1)/n_GDL:L2;
111
112     % Call routine to compute initial guess
113     ini_sol = compute_initial_solution(xinit);
114
115     %--- Solve problem
116     % Use default integration properties.
117     options = bvpset('RelTol', 1e-5, 'NMax', 10000, 'Stats', 'on');
118
119     sol = bvp4c(@MODEL_ODEfun, @MODEL_bcfun, ini_sol, options, D_ij,
120     p_O2_l_array);
121
122     x_dir = linspace(L1,L2,1e3); % generates a row vector of 50 linearly
123         equally
124     % spaced points between 0 and L.
125     Solution.mesh=x_dir;
126     y = deval(sol,x_dir); % evaluates the solution of the problem
127     % at all the entries of the vector x.
128
129     %Create the Solution object. Note that the Solution
130     object is obtained by interpolating the solution from
131     bvp4c to a finer mesh
132     n_O2(j,i)=y(1,1); %n_O2 is constant through GDL
133     %rho_O2(j,i)=y(3,999);
134     res(j,i) = (n_O2(j,i) - n_O2_exp(j)).^2;
135
136     end
137     %Res(i,1) =sum(res(j,i),j);
138     Res(i,1) =sum(res(:,i));
139
140 end
141 [Res_min, I]=min(Res);
142 min_residual = Res(I)
143 D_eff = D_ij_vec(I);
144 Diffusibility = D_eff/D_bulk

```

```

144 figure(1);
145 plot(D_ij_vec , Res, 'ko-', 'Markersize',15, 'Linewidth',2);
146 hold on
147 xlabel('Effective Diffusivity Guess', 'FontSize',20);
148 ylabel('Residual', 'FontSize',20);
149 figure(2);
150 h1=plot(delta_p , n_O2_exp , 'kv', 'Markersize',6);
151 hold on
152 h2=plot(delta_p , n_O2(:,I) , '-k', 'Linewidth',2);
153 legend([h1 h2], 'Experimental data', 'Fit')
154 xlabel('\nabla P', 'FontSize',20);
155 ylabel('Oxygen Mass Flux', 'FontSize',20);
156 D_ij = D_ij_vec(I);
157 for j=1:N_1
158     p_O2_l_array=p_O2_l(j,1);
159     x_O2_array=x_O2(j,1);
160
161     % Initial mesh -
162     L1 = 0;
163     L2 = GDL.L;
164     n_GDL = 1e3; %number of points in the initial mesh, try
165     to keep more than 1e5 to avoid singular Jacobian matrix
166     xinit = L1:(L2-L1)/n_GDL:L2;
167
168     % Call routine to compute initial guess
169     ini_sol = compute_initial_solution(xinit);
170
171     %--- Solve problem
172     % Use default integration properties.
173     options = bvpset('RelTol', 1e-5, 'NMax', 10000, 'Stats', 'on');
174
175     sol = bvp4c(@MODEL_ODEfun, @MODEL_bcfun, ini_sol, options, D_ij,
176               p_O2_l_array);
177
178     x_dir = linspace(L1,L2,1e3); %generates a row vector of 50 linearly
179     equally spaced points between 0 and L.
180     Solution.mesh=x_dir;
181     y = deval(sol,x_dir); % evaluates the solution of the problem
182     % at all the entries of the vector x.
183
184     %Create the Solution object. Note that the Solution object is
185     %obtained by interpolating the solution from bvp4c to a finer mesh
186     w_O2(j,:) = y(3,:); %n_O2 is constant through GDL
187     p_t(j,:) = y(4,:);
188
189     end
190
191 figure(3);
192 [n_param n_points] = size(w_O2);
193 for jj =1:(n_param-1)
194     plot(Solution.mesh, w_O2(jj,:), '-')
195     hold on
196 end

```

```

197 plot(Solution.mesh,w_O2(n_param,:),'-')
198 legend('w_O2(x)')
199 title('Fraction of O2')
200 xlabel('x'), ylabel('n_O2(x)')
201 figure(4);
202 [n_param n_points] = size(w_O2);
203 for jj =1:(n_param-1)
204     plot(Solution.mesh,p_t(jj,:),'-')
205     hold on
206 end
207 plot(Solution.mesh,p_t(n_param,:),'-')
208 legend('p_t(x)')
209 title('Total pressure')
210 xlabel('x'), ylabel('p_t(x)')
211 end
212
213 function ini_sol = compute_initial_solution(xinit)
214
215 % Constant initial guess of the solution for [y1(x);y2(x); ... ,y15(x)]
216 yinit =[0.0001
217         0.0001
218         0.25
219         (13.7+10)*6900+5
220         ];
221
222 % Interpolate the solution to each point in the grid
223 ini_sol = bvpinit(xinit,yinit);
224
225 end
226 %Function compute_initial_solution
227
228 %-----
229 %
230 % Various Constants used in main.m
231 % These constants are required to solve for D_eff in the diffusion exps
232 % Created by: Prafful Mangal
233 % NOTE 1:On this page, you need to change sample thickness (L), permeability
234 % of sample (B_v), flow rate of nitrogen gas (vv).
235 % NOTE 2:Depending on the experiment condition, you may also need to change
236 % the pressure of nitrogen (p_N2_r), bulk diffusivity (D_bulk)
237 %-----
238 function [D_bulk,dia,t,w,L, R, T, M_O2, M_N2, eta_O2,
239 eta_N2, B_v,zeta_O2N2,zeta_N2O2,zeta_O2O2,zeta_N2N2,
240 p_N2_r, rho_o,vv,rho_O2] = load_constants()
241
242 p_N2_r = (13.7+10)*6900*ones(5,1);
243 % Pressure of nitrogen set using BPC (usually 10 psig)
244 %p_N2_r2= (14.64+15)*6900*ones(6,1);
245
246 %%%%%%%%%%%%%%%%%%%%%%%%%%%%%%%%%%%%%%%%%%%%%%%%%%%%%%%%%%%%%%%%%%%%%%%%%%
247 L = 870e-6; %Thickness of the GDL (in m)
248 B_v = 1.05E-11;
249 % Viscous permeability obtained from separate permeability experiment

```

```

250 %%%%%%%%%%%%%%%%%%%%%%%%%%%%%%%%%%%%%%%%%%%%%%%%%%%%%%%%%%%%%%%%%%%%%%%%%
251 %%%%%%%%%%%%%%%%%%%%%%%%%%%%%%%%%%%%%%%%%%%%%%%%%%%%%%%%%%%%%%%%%%%%%%%%%
252 %Select proper D_bulk for selected pair of gas and
253 absolute pressure (usually N2_O2 at 10psig)
254 % The values are taken from literature %%%%%%%%%%%%%%%%%%%%%%%%%%%%%%%%%%%%%%%%%%%%%%%%%%%%%%%%%%%%%%%%%%%%%%%%%
255 %%%%%%%%%%%%%%%%%%%%%%%%%%%%%%%%%%%%%%%%%%%%%%%%%%%%%%%%%%%%%%%%%%%%%%%%%
256 %%%%%%%%%%%%%%%%%%%%%%%%%%%%%%%%%%%%%%%%%%%%%%%%%%%%%%%%%%%%%%%%%%%%%%%%%
257 %D_bulk= 2.19e-5; %at 1atm(m2/s)
258 %D_bulk= 1.5352697563e-5; %at 5psig N2_O2(m2/s)
259 D_bulk= 1.22697563e-5; %at 10psig N2_O2(m2/s)
260 %D_bulk = 1.019955e-5; %at 15psig N2_O2
261 %D_bulk = 0.872737e-5; %at 20psig N2_O2
262 %D_bulk = 7.33155e-5; %at 1atm He_O2
263 %D_bulk = 5.42e-5; %at 5 psig He_O2
264 %D_bulk = 4.33155e-5; %at 10 psig He_O2
265 %D_bulk = 3.53e-5; %at 15 psig He_O2
266 %D_bulk = 3.080993e-5; %at 20 psig He_O2
267 %D_bulk = 1.158645e-5; % at 10 psig Ar_O2
268
269 %%%%%%%%%%%%%%%%%%%%%%%%%%%%%%%%%%%%%%%%%%%%%%%%%%%%%%%%%%%%%%%%%%%%%%%%%
270 %%%%%%%%%%Select density of gas used apart from Oxygen (usually Nitrogen)%%
271 %%%%%%%%%%%%%%%%%%%%%%%%%%%%%%%%%%%%%%%%%%%%%%%%%%%%%%%%%%%%%%%%%%%%%%%%%
272
273 rho_o = 1.251; %Nitrogen (kg/m3)
274 rho_O2 = 1.429; %Oxygen
275 %rho_o = 1.783; %Argon
276 %rho_o = 0.179; %Helium
277
278 %%%%%%%%%%%%%%%%%%%%%%%%%%%%%%%%%%%%%%%%%%%%%%%%%%%%%%%%%%%%%%%%%%%%%%%%%
279 %%%%%%%%%%%%%%%%%%%%%%%%%%%%%%%%%%%%%%%%%%%%%%%%%%%%%%%%%%%%%%%%%%%%%%%%%
280 %%%%%%%%%% Select the proper geometry of porous media %%%%%%%%%%
281 %%%%%%%%%%%%%%%%%%%%%%%%%%%%%%%%%%%%%%%%%%%%%%%%%%%%%%%%%%%%%%%%%%%%%%%%%
282
283 dia=8e-3; % Diameter of porous media (For Through-plane exps),m
284 t=920e-6; % Shim Thickness of porous media (For In-Plane exps),m
285 w=0.05; % Width of porous media(m) (For In-Plane exps, fixed as 50mm),m
286 %%%%%%%%%%%%%%%%%%%%%%%%%%%%%%%%%%%%%%%%%%%%%%%%%%%%%%%%%%%%%%%%%%%%%%%%%
287 %%%%%%%%%%%%%%%%%%%%%%%%%%%%%%%%%%%%%%%%%%%%%%%%%%%%%%%%%%%%%%%%%%%%%%%%%
288
289 vv=0.635; %%%% Flow rate of nitrogen gases in LPM
290
291 R=8.3144622;% J/(mol*K)
292 T=298.15; %K
293 %%%%%%%%%%%%%%%%%%%%%%%%%%%%%%%%%%%%%%%%%%%%%%%%%%%%%%%%%%%%%%%%%%%%%%%%%
294 %%%%%%%%%% Select the correct molecular mass and viscosity for the gases used %
295 %%%%%%%%%%%%%%%%%%%%%%%%%%%%%%%%%%%%%%%%%%%%%%%%%%%%%%%%%%%%%%%%%%%%%%%%%
296
297 M_O2 = 32e-3; %kg/mol
298 M_N2 = 28e-3; %kg/mol
299 %M_N2 = 4e-3; %kg/mol
300 eta_O2 = 2.06e-5; % O2, Pa.s
301 eta_N2=1.80e-5;%Nitrogen Pa.s
302 %eta_N2=2.23e-5; %Argon
303 %eta_N2=2.02e-5; %Helium

```

```

304
305 %%%%%%%%%%%%%%%%%%%%%%%%%%%%%%%%%%%%%%%%%%%%%%%%%%%%%%%%%%%%%%%%%%%%%%%%%
306 %%%%%%%%%%%%%%%%%%%%%%%%%%%%%%%%%%%%%%%%%%%%%%%%%%%%%%%%%%%%%%%%%%%%%%%%%
307 %% Below are the equations to find Lennard Jones parameter that can be used to
      find eta-mix%%
308
309 zeta_O2N2=(1+(eta_O2/eta_N2)^0.5*(MN2/MO2)^0.25)^2/(8*(1+MO2/MN2))^0.5;
      % Lennard Jones parameters calculated using equations from Reid et al.
310 zeta_N2O2=eta_N2*M_O2*zeta_O2N2/(eta_O2*MN2);
311 zeta_O2O2=1;
312 zeta_N2N2=1;
313 %%%%%%%%%%%%%%%%%%%%%%%%%%%%%%%%%%%%%%%%%%%%%%%%%%%%%%%%%%%%%%%%%%%%%%%%%
314 end
315
316 %%%%%%%%%%%%%%%%%%%%%%%%%%%%%%%%%%%%%%%%%%%%%%%%%%%%%%%%%%%%%%%%%%%%%%%%%
317 %%%%%%%%%%%%%%%%%%%%%%%%%%%%%%%%%%%%%%%%%%%%%%%%%%%%%%%%%%%%%%%%%%%%%%%%%
318 %%%%%%%%%%%%%%% Apply the boundary conditions here %%%%%%%%%%%%%%%
319 %%%%%%%%%%%%%%%%%%%%%%%%%%%%%%%%%%%%%%%%%%%%%%%%%%%%%%%%%%%%%%%%%%%%%%%%%
320 %%%%%%%%%%%%%%%%%%%%%%%%%%%%%%%%%%%%%%%%%%%%%%%%%%%%%%%%%%%%%%%%%%%%%%%%%
321
322 function res = MODEL_bcfun(YL,YR, x_O2_array , p_O2_l_array )
323 M_O2 = 32e-3;
324 M_N2 = 28e-3;
325 R=8.3144622;
326 T=298.15;
327
328 %v=B_v/eta_mix*(delta_p/GDL.L);
329 % mol_extra = p_O2_l/(R*T)*A*v;
330 res = [
331     YR(3)-0    % Mass fraction of oxygen at 10 psig at x=L, N2 channel
332     YL(3)-1    % Mass fraction of oxygen at 10 psig at x=0,O2 channel
333     YL(4)-p_O2_l_array    % Mixture pressure at x=0,O2 channel
334     YR(4)-(13.7+10)*6900    % Mixture pressure at x=L,N2 channel
335     ];
336 end
337
338
339 %%%%%%%%%%%%%%%%%%%%%%%%%%%%%%%%%%%%%%%%%%%%%%%%%%%%%%%%%%%%%%%%%%%%%%%%%
340 %%%%%%%%%%%%%%%%%%%%%%%%%%%%%%%%%%%%%%%%%%%%%%%%%%%%%%%%%%%%%%%%%%%%%%%%%
341 %%% This file shows system of equations used to estimate D_eff%%
342 %%%%%%%%%%%%%%% Created by: Prafful Mangal %%%%%%%%%%%%%%%
343 %%%%%%%%%%%%%%%%%%%%%%%%%%%%%%%%%%%%%%%%%%%%%%%%%%%%%%%%%%%%%%%%%%%%%%%%%
344 %%%%%%%%%%%%%%%%%%%%%%%%%%%%%%%%%%%%%%%%%%%%%%%%%%%%%%%%%%%%%%%%%%%%%%%%%
345
346 function dydx = MODEL_ODEfun(x, y, D-ij , p_O2_l_array )
347
348 %--- Initialize gradient vector:
349 dydx = zeros(4,1);
350
351 %--- Read the solution:
352 n_O2 = y(1); % Oxygen mass flux
353 n_t = y(2); % Total mass flux
354 w_O2 = y(3); % Oxygen mass fraction
355 p-t = y(4); % Total pressure

```



```

356
357
358 %Some constants are assigned values here
359 [D_bulk, dia, t, w, L, R, T, M_O2, M_N2, eta_O2, eta_N2, B_v, zeta_O2N2,
360 zeta_N2O2, zeta_O2O2, zeta_N2N2, p_N2_r, rho_o, v] = load_constants();
361
362
363 %rho_t = p_t*M_N2/(R*T)/(1-((M_O2 - M_N2)/M_O2)*w_O2); % Mixture density
364 rho_t = 1.429*((p_N2_r(1,1)+50)/101000)*0.5+rho_o*(p_N2_r(1,1)/101000)*0.5;
365 %rho_O2 = w_O2*rho_t; % Mass fraction of oxygen
366 w_N2 = 1-w_O2; % Mass fraction of nitrogen
367 M = 1/(w_O2/M_O2 + w_N2/M_N2); % Molecular weight of the mixture
368
369 % x_O2 = w_O2*M/M_O2; % Mole fraction of oxygen
370 % x_N2 = (1-w_O2)*M/M_N2; % Mole fraction of nitrogen
371
372 %eta_mix = (x_O2*eta_O2)/(x_O2*zeta_O2O2 + x_N2*zeta_O2N2) +
373 (x_N2*eta_N2)/(x_N2*zeta_N2O2 + x_N2*zeta_N2N2); %Chapman-Enskog equation
374
375 eta_mix = eta_O2*0.5 + eta_N2*0.5; % Pa.s
376
377
378 % Build system of equations:
379 dydx(1) = 0;
380 dydx(2) = 0;
381 dydx(3) = (1/D_ij)*(w_O2*(n_t/rho_t) - n_O2/rho_t);
382 %dydx(4) = (1/D_ij)*(rho_N2*n_t/rho_t - (n_t - n_O2));
383 dydx(4) = - (eta_mix/B_v)*(1/rho_t)*n_t;
384 end

```

Appendix B

CL/filter through-plane diffusivity analysis software

```
1 clear
2 clc
3 %%%Experimental data%%%
4 %change the value according to experimental condition%
5 L=80E-6;%thickness in m
6 P=13.7;%experimental pressure , psi
7 V_MFC=1.1;%volume flow rate from MFC in LPM, experimental condition
8 V=1.1*0.001/60;%volume flow rate, m3/s, experimental condition
9 d=0.008;%diameter in m
10 A=3.14/4*d^2;%cross-sectional area
11 x=0.0373;%oxygen mole fraction measured by sensor (0.05 means 5%)
12
13 %%%Constant%%%
14 rho_N2_STP=1.25;%N2 density, kg/m3, STP
15 rho_He_STP=0.179;%He density, kg/m3, STP
16 rho_O2_STP=1.43;%O2 density, kg/m3, STP
17 P_STP=14.7;%standard pressure 101325/6900=14.7 psi
18 rho_N2=rho_N2_STP*P/P_STP;%N2 density, kg/m3, experimental condition
19 rho_He=rho_He_STP*P/P_STP;%He density, kg/m3, experimental condition
20 rho_O2=rho_O2_STP*P/P_STP;%O2 density, kg/m3, experimental condition
21
22 %%%choose gases%%%
23 rho_t=(rho_N2+rho_O2)/2;%mixture density for N2-O2, use N2-O2 or He-O2
24 %rho_t=(rho_He+rho_O2)/2;%mixture density for He-O2, use N2-O2 or He-O2
25 D_bulk_STP=2.2E-5;%bulk diffusivity of N2-O2(m2/s) STP, use N2-O2 or He-O2
26 %D_bulk_STP=7.4E-5;%bulk diffusivity of He-O2(m2/s) STP, use N2-O2 or He-O2
27 D_bulk=D_bulk_STP*P_STP/P; %bulk diffusivity at experimental condition
28 D_eff=V*rho_O2*x*L/A/rho_t;%effective diffusivity
29 Diff=D_eff/D_bulk;
```

Appendix C

CL through-plane permeability and effective pore diameter

```
1 clear
2 clc
3 L=80E-6; %in m, sample thickness
4 eta_N2=1.82E-5; % N2, in Pa.s
5 eta_He=2.02E-5; %He, in Pa.s
6 M_N2=28E-3; %N2, in kg/mol
7 M_He=4E-3; %He, in kg/mol
8 T=300; % gas temperature
9 p2=94500; %outlet pressure
10
11 p1_N2=94500+[
12 790
13 1550
14 2300
15 3020
16 3740
17 4505
18 5217
19 5900
20 6610
21 7278
22
23
24 ];%%matrix for p1, velocity
25
26 p1_He=94500+[
27 380
28 840
29 1280
30 1750
31 2150
32 2587
33 3031
34 3465
35 3857
36 4324
```

```

37
38 ];%%matrix for p1, velocity
39
40 y_N2=1.07*[
41
42 0.00342932
43 0.0068074
44 0.0102196
45 0.01352944
46 0.01706106
47 0.020473265
48 0.02390262
49 0.027246565
50 0.0306076
51 0.03407098
52
53
54 ]; %%matrix for v1, velocity
55
56 y_He=1.07*[
57 0.0034805
58 0.00682446
59 0.0101343
60 0.01361474
61 0.01706106
62 0.020456205
63 0.02388556
64 0.02729775
65 0.03062466
66 0.03412216
67
68
69 ]; %%matrix for v1, velocity
70 point=size(p1_N2); %number of datapoint
71 datapoint=max(point); %number of datapoint
72
73 x1_N2=zeros(datapoint,1);
74 x2_N2=zeros(datapoint,1);
75 x1_He=zeros(datapoint,1);
76 x2_He=zeros(datapoint,1);
77
78
79 dpeff_guess = linspace(1E-9, 3E-7, 600); %0.5e-8:0.5e-8:0.2e-5;
80 Bv_guess= linspace (1E-16, 3E-14, 1100); %4e-13:1e-15:4.5e-12;
81 tmp1=size(dpeff_guess);
82 N_1=max(tmp1);
83 tmp2=size(Bv_guess);
84 N_2=max(tmp2);
85 tmp3=size(x1_N2);
86 N_3=max(tmp3);
87 p_moedl_N2=zeros(N_3,1);
88 p_moedl_He=zeros(N_3,1);
89 res=zeros(N_2,1);
90 Res_Bv=zeros(N_1,N_2);

```

```

91
92
93 for i = 1:N_1
94     dpeff=dpeff_guess(i);
95     for j=1:N_2
96         Bv=Bv_guess(j);
97         for k=1:N_3
98             A1=Bv/2/eta_N2/L; %solving A*p^2+B*p+C=0 to get inlet p1, N2
99             B1=0.89*dpeff*sqrt(8*8.314*300/3.14/M_N2)/3/L-y_N2(k);
100            C1=-Bv*p2^2/2/eta_N2/L-0.89*dpeff*sqrt(8*8.314*300/3.14/M_N2)/3/L*p2;
101
102            A2=Bv/2/eta_He/L; %solving A*p^2+B*p+C=0 to get inlet p1, He
103            B2=0.89*dpeff*sqrt(8*8.314*300/3.14/M_He)/3/L-y_He(k);
104            C2=-Bv*p2^2/2/eta_He/L-0.89*dpeff*sqrt(8*8.314*300/3.14/M_He)/3/L*p2;
105            p_moedl_N2(k)=((-B1)+sqrt(B1^2-4*A1*C1))/(2*A1); %solving quadratic
            equation
106            p_moedl_He(k)=((-B2)+sqrt(B2^2-4*A2*C2))/(2*A2); %solving quadratic
            equation
107            res(k)=(p_moedl_N2(k)-p1_N2(k))^2+(p_moedl_He(k)-p1_He(k))^2;
108        end
109        Res_Bv(i,j)=sum(res);
110    end
111 end
112 min(min(Res_Bv))
113 [Number_dpeff, Number_Bv]=find(Res_Bv==min(min(Res_Bv)));
114 dpeff_final=dpeff_guess(Number_dpeff);
115 Bv_final=Bv_guess(Number_Bv);
116
117 [X,Y] = meshgrid(dpeff_guess, Bv_guess);
118 figure(1)
119 contour(X,Y,Res_Bv',1000)%,'ShowText','on')
120 grid on
121 xlabel('Effective pore diameter [m]')
122 ylabel('Permeability [m^2]')
123 hold on
124 plot(dpeff_guess(Number_dpeff),Bv_guess(Number_Bv),'x')
125 legend('Optimum Solution','Location','SouthEast')
126 figure(2)
127 mesh(X,Y,Res_Bv')

```

Appendix D

Factory certificates

OMEGADYNE INC.
An Affiliate of Omega Engineering, Inc.
CERTIFICATE OF CALIBRATION

Model Number: MMDDB050BIV10B2C0T3A6

Serial Number: 418617 **Capacity:** 3.50 BAR
Date: 11/13/2012 **Excitation:** 24.00 Vdc
Job: R5704 **Technician:** GRS

Pressure Connection: 1/4-18 NPT Male

Electrical Connection: **WIRING CODE**
BLACK = - EXCITATION
WHITE = + OUTPUT
GREEN = N/C
RED = + EXCITATION

CALIBRATION WORKSHEET		NOTES
Pressure BAR	OUTPUT Vdc	
0.00	0.009	
1.75	5.010	
3.50	10.007	
1.75	5.010	
0.00	0.009	

NIST Traceable Number(s): C-1956, C-1317

Omegadyne Inc., certifies that the above instrumentation has been calibrated and tested to meet or to exceed the published specifications. This calibration was performed using instrumentation and standards that are traceable to the National Institute of Standards and Technology. This document also ensures that all testing performed complies with MIL-STD 45662-A, ISO 10012-1, and ANSI/NCSL Z540-1-1994 requirements. After Final Calibration our products are stored in an environmentally controlled stock room and are considered in bonded storage. Depending on environmental conditions and severity of use, factory calibration is recommended every one to three years after the initial service installation date.

Bruce Lott
Accepted and Certified By

11/13/2012
Date

Omegadyne Inc., 149 Stelzer Court, Sunbury, OH 43074 (740) 965-9340
http://www.omegadyne.com email: info@omegadyne.com (800) USA-DYNE

Figure D.1: Factory certificate of pressure transducer

Cole Parmer Instrument Co.
Calibration Data Sheet
 Certification Number: 58253

Sales Order Number: S006250
Serial Number: 62704
Part Number: 32407-69
Software Version: QP07R08
PID/I Values: 100 / 5000 / 0
Process Gas: Selectable
Calibration Gas: Air
Range: 5 SLPM
Gas Temperature: 25.6 °C
Ambient Humidity: 30%
Calibration Procedure/Rev. #: DOC-AUTOCAL-GASFLOW/Rev. 65
Calibrated By: James Tolentino
Calibration Date: 05/18/2011
Full Scale Pressure: 160 PSIA
Full Scale Pressure Accuracy: +/- 0.5% of Full Scale
Temperature Accuracy: +/- 1.5 °C
Standard Temp. & Pressure: 25°C, 14.6959 PSIA
Calibration due 1 yr. after receipt:

Equipment Used

Voltage: TOOL-CMTR11	Temperature: TOOL-TEMP6
Tool Due Date: 07/08/2011	Tool Due Date: 07/08/2011
Manufacturer/Model: Fluke 85	Manufacturer/Model: ERTCO
Device Uncertainty: +/- (0.1% + 1 digit)	Device Uncertainty: +/- 0.2 deg C

Flow: TOOL-FLOW12	Pressure: TOOL-PRESSURE8
Tool Due Date: 03/23/2012	Tool Due Date: 04/14/2012
Manufacturer/Model: Alicat / MCAL-SE0L	Manufacturer/Model: Alicat / P-100PSIG-D
Device Uncertainty: +/- (0.3% Reading + 0.2% F.S.)	Device Uncertainty: +/- 0.2% of full scale

All test equipment used for calibration is NIST traceable.

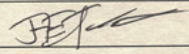
Calibration

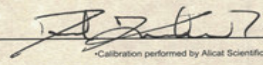
Uncertainty: +/- (0.8% of Reading + 0.2% of Full Scale) **Calibration Pressure:** Inlet: 10 PSIG
Units of measure: SLPM Outlet: 0 PSIG

Output 1 Configuration	Output 2 Configuration
mini-DIN pin #6	mini-DIN pin #2

D.U.T.	Actual	In Tolerance	Output 1	Output 2
0.000	0.000	Yes	0.000 Vdc	5.12 Vdc
1.246	1.248	Yes	1.248 Vdc	5.12 Vdc
2.499	2.510	Yes	2.499 Vdc	5.12 Vdc
3.742	3.765	Yes	3.742 Vdc	5.12 Vdc
4.991	4.995	Yes	4.99 Vdc	5.12 Vdc

Notes: 0-5V set-point.

Tech Signature: 

QC Signature: 

Calibration performed by Alicat Scientific, Inc.

C51 Rev 15 Last Modified 04/12/2011

Figure D.2: Factory certificate of mass flow controller 1

Cole Parmer Instrument Co.
Calibration Data Sheet
Certification Number: 58207

Sales Order Number: SO306244
Serial Number: 82661
Part Number: 32907-69
Software Version: G907R08
PID/I Values: 100 / 12000 / 0
Process Gas: Selectable
Calibration Gas: Air
Range: 5 SLPM
Gas Temperature: 25.5 °C
Ambient Humidity: 24%
Calibration Procedure/Rev. #: DOC-AUTOCAL-GASFLOW/Rev. 65
Calibrated By: Thomas Hermes
Calibration Date: 05/17/2011
Full Scale Pressure: 160 PSIA
Full Scale Pressure Accuracy: +/-0.5% of Full Scale
Temperature Accuracy: +/-1.5 °C
Standard Temp. & Pressure: 25°C, 14.6959 PSIA
Calibration due 1 yr. after receipt:

Equipment Used

Temperature: TOOL-TEMP6	Voltage: TOOL-CMTR13
Tool Due Date: 07/08/2011	Tool Due Date: 12/09/2011
Manufacturer/Model: ERTCO	Manufacturer/Model: Fluke / 87
Device Uncertainty: +/- 0.2 deg.C	Device Uncertainty: +/- (0.1% + 1 digit)

Flow: TOOL-FLOW12	Pressure: TOOL-PRESSURE8
Tool Due Date: 03/23/2012	Tool Due Date: 04/14/2012
Manufacturer/Model: Alicat / MCAL-5E0L	Manufacturer/Model: Alicat / P-100PSIG-D
Device Uncertainty: +/- (0.3% Reading + 0.2% F.S.)	Device Uncertainty: +/- 0.2% of full scale

All test equipment used for calibration is NIST traceable.

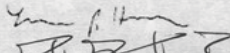
Calibration

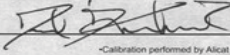
Uncertainty: +/- (0.8% of Reading + 0.2% of Full Scale) Calibration Pressure: Inlet: 10 PSIG
Units of measure: SLPM Outlet: 0 PSIG

Output 1 Configuration	Output 2 Configuration
mini-DIN pin #6	mini-DIN pin #2

D.U.T.	Actual	In Tolerance	Output 1	Output 2
0.000	0.000	Yes	0.000 Vdc	5.12 Vdc
1.248	1.249	Yes	1.248 Vdc	5.12 Vdc
2.495	2.508	Yes	2.495 Vdc	5.12 Vdc
3.752	3.765	Yes	3.750 Vdc	5.12 Vdc
4.992	4.992	Yes	4.99 Vdc	5.12 Vdc

Notes: 0-5V set-point.

Tech Signature: 

QC Signature: 

Calibration performed by Alicat Scientific, Inc. CS1 Rev 15 Last Modified 04/12/2011

Figure D.3: Factory certificate of mass flow controller 2